Multi-stage Cu Mineralization of the Mowana Copper Deposit, Matsitama Schist Belt, NE Botswana

ボツワナ北東部、Matsitama 片岩帯、Mowana 銅鉱床の多段階 Cu 鉱化作用

Amogelang Kooganne

ID No: 6518102

Department of Geosciences, Geotechnology and Materials Engineering for Resources

Graduate School of International Resource Sciences

Akita University, Japan

2021

ABSTRACT

The Mowana hydrothermal Cu deposit is located within the Matsitama-Motloutse Complex in the southwestern part of the Zimbabwe Craton in the northeastern part of Botswana. The deposit is in the northern-most flank of the Matsitama Schist Belt, which makes one of the four granite-greenstone belts of north-eastern Botswana. It is poorly understood and has received less documentation since its discovery, by comparison to other ore deposits in the same area. Mowana deposit is unique from other Archean greenstone belt vein deposits in the sense that instead of Au mineralization it is rather dominated by Cu mineralization. There is a large, inferred time gap between rock formation and mineralization. The deposit is hosted by the NNE-striking and nearly vertically dipping (70-80°) Bushman Lineament (shear zone) within the graphitic schist lenses in the carbonaceous and argillaceous metasedimentary rocks of the Neoarchean to Paleoproterozoic Matsitama Sedimentary Group. Within the Matsitama Sedimentary Group, the Mowana deposit is hosted by rocks belonging to the Bushman Mine group, a sedimentary fining upward sequence. The Matsitama Sedimentary Group is enclosed within the foliated granitoids of the Matsitama-Motloutse Complex. The ca. 0.2 Ga Phanerozoic Karoo Supergroup overlies these units.

The host metasedimentary rocks: limestone, argillite and graphitic schist, as well as the surrounding granites, suffered from hydrothermal alteration. The hydrothermal alteration is characterized by silicification, chloritization, epidotization, sericitization, hematite, and carbonate alterations. Based on the alteration mineral assemblage, the main mineralization stage is attributed to near-neutral pH fluids at temperatures between ~200 °C and ~>340 °C. The temperatures obtained from the chlorite

geothermometry of the Type 1 veins coincides with the above temperature in the range 340-400 °C and a modal temperature of 370-380 °C.

The base metal mineralization of the Mowana deposit evolved in at least two hydrothermal vein types. The first mineralization type, represented by the quartz+calcite±K-feldspar veins and breccias, is characterized by the precipitation of principal chalcopyrite with pyrite, minor bornite and trace amounts of galena. The Type 2, represented by quartz+calcite±fluorite veins, hosts appreciable amounts of galena. The supergene mineralization is widely distributed in the shallow levels (up to 70 m below the surface) of the deposit. Supergene enrichment is manifested by the significant presence of chalcocite, bornite, covellite and anglesite. Oxidation is characterized by Fe-oxides and Cu carbonates: malachite, goethite, and hematite. The ore mineral assemblage of pyrite+chalcopyrite+bornite paired with the temperature obtained from the chlorite geothermometry from the Type 1 veins was used to determine the sulfidation state of the Mowana deposit. The ore mineral assemblage of the Type 1 veins lies on the pyrite+chalcopyrite+bornite buffer line at a temperature of 340 to 400 °C indicating that the Type 1 veins evolved under a transition between intermediate and high sulfidation state.

Chalcopyrite is the principal Cu-bearing mineral, which also contains an average 67.4 ppm of Ag which may be due to incorporation of Ag in the Cu site. Galena from the Type 2 veins has high contents of Se with an average of 1231 ppm, possibly incorporated as PbSe. The average Ag content in galena from the Type 2 veins is 58.9 ppm. The average Co, Ni, and As contents in pyrite are 143 ppm, 33.6 ppm, and 107 ppm, respectively.

Fluid Inclusion analysis was also conducted. Two-phase (liquid and gas) fluid inclusions were observed in the mineralized quartz veins. However, the fluid inclusions were too small to perform microthermometry.

The carbon isotopic composition of graphite from graphitic schist are from -21.0 to -29.8 ‰ (average 26 ‰) indicating a biogenic origin, possibly from cyanobacteria living in shallow water. The $\delta^{13}C$ values of the metacarbonates range from 6.05 to 6.89 ‰ which is higher than the global trend at the time of deposition and rarely observed in Archean carbonates. These heavier values may be explained by diagenetic carbonate precipitation during which dissolved inorganic C is enriched in ^{13}C by methanogenic processes, or alternatively by burial of reduced carbon in an isolated basin at that time, with the residual dissolved carbon being enriched in ^{13}C. The carbon isotopic compositions of the calcite of Type 1 veins ranging from 0.46 to 0.53 ‰ could indicate derivation from a mixed source including C from both host rock types. The $\delta^{18}O$ of the quartz is in the range 9.25 to 10.30 ‰ relative to Standard Mean Water Ocean Water (SMOW). The $\delta^{18}O$ values of calcite range from -12.42 to -22.34 ‰ with respect to Vienna Pee Dee Belemnite (VPDB). The calculated temperature from the co-existing mineral pairs of quartz and calcite in equilibrium range between 250 to 360 °C.

Sulfur isotopic ratios determined on the sulfides from Type 1, Type 2 and diagenetic pyrite help to understand the evolution of the hydrothermal system. The sulfides, chalcopyrite, chalcocite and galena from Type 1 and Type 2 veins, recorded isotopic compositions $\delta^{34}S$ in the range -5 ‰ to +4 ‰. These values may indicate a magmatic sulfur source of S and/or leaching of the host metasedimentary rocks. However, $\delta^{34}S$ of diagenetic pyrite disseminated in silicified limestone and pyrite from

a quartz+calcite±K-feldspar vein recorded sulfur isotopic values of +15.4 ‰ and +18.0 ‰. The values can be explained by closed system reduction of seawater sulfate, followed by remobilization of the $\delta^{34}S$ rich diagenetic pyrite during brecciation as the possible sources of S.

TABLE OF CONTENTS

LIST OF FIGURES

LIST OF TABLES

CHAPTER 1: INTRODUCTION

1.1 Vein type deposits

Vein type deposits are described as zones of mineralization in an inclined and discordant structures such as faults, fissure opening and/or shear zones within the host rocks (Berger, 1982; Haynes, 1993). The ore minerals in the veins are often deposited along with quartz and calcite as gangue minerals (Berger, 1982). The deposit is often formed because of hot hydrothermal fluids ascending to the surface through either fractures, brecciated rocks or faults react with the surrounding country rocks (Berger, 1982). The precipitation and deposition of the ore minerals which are carried as ionic complexes occur once the physiochemical such as temperature, pressure and/ or oxido-reduction conditions are favourable or change as the fluids percolate through the structures (e.g. Reed and Palandri, 2006). The interaction of the hydrothermal fluids with the surrounding country rocks results in the alteration zones with distinctive new minerals which reflect the geochemical composition of the ore forming fluids (Zhu and Tan, 2011). The presence of the igneous rocks and the typical alteration act as a tool for further exploration of the deposits (Zhu and Tan, 2011). Vein deposits include Au, Ag and few Cu-Pb-Zn deposits (Zhu and Tan, 2011). The vein deposits are characterized by mainly quartz, and other gangue minerals such as calcite and minor amounts of sulfides (Zhu and Tan, 2011). The deposits are usually small, and the mineralization occurs in shoots within the vein structures (Berger, 1982). Hydrothermal deposits have been grouped into three types based on their conditions of origin (Waldemar, 1928). These include epithermal, mesothermal and hypothermal deposits (Waldemar, 1928). The epithermal deposits are characterized by formation at shallow depths (<1500 m) at relatively low temperatures (Waldemar, 1928,

Simmons et al., 2005). The mesothermal ore deposits are formed at intermediate depths (1500 m to 4500 m), and pressure at temperatures in the range 200°C to 400°C (Waldemar, 1928). Hypothermal ore deposits are characterized by forming at greater depths below 4500 m and at relatively higher temperatures (400-600°C) (Waldemar 1928).

1.2 Location of the study area, and accessibility

Previously known as the Dukwi project, the Mowana deposit which translates to baobab in English was re-named in 2007 after the giant baobab tree in Setswana language that stands tall by the entrance to the mine lease area (African Copper, 2005). It is located approximately 120 km northwest of Francistown in the North east district. It is contained within the geographical coordinates 20˚31'38" S and 26˚35'46" E (Figure 1; Newall et al., 2018). The deposit is accessible through the A1 highway tarmac road that runs through the country from the Capital city Gaborone (south) to Francistown (North). From Francistown the A1 highway connects to the A3 highway which runs until Maun. The drive time is approximately 1 ½ hours from Francistown. An approximately 10 km due north gravel road at Dukwi village along the A3 highway leads to the Mowana mine.

The deposit lies in the flat, semi-desert scrub-bush vegetation with a gentle slope from east to west with drainage into the makgadikgadi basin (Newall et al., 2018). The topography around the deposit is generally flat with little or no relief as shown in Figure. 2. The climate is hot, semi-arid (steppe) and dry with temperatures ranging from about 7°C in winter and peaking up to 40°C in summer (Newall et al., 2018). The annual rainfall is less than 250 mm (Newall et al., 2018)

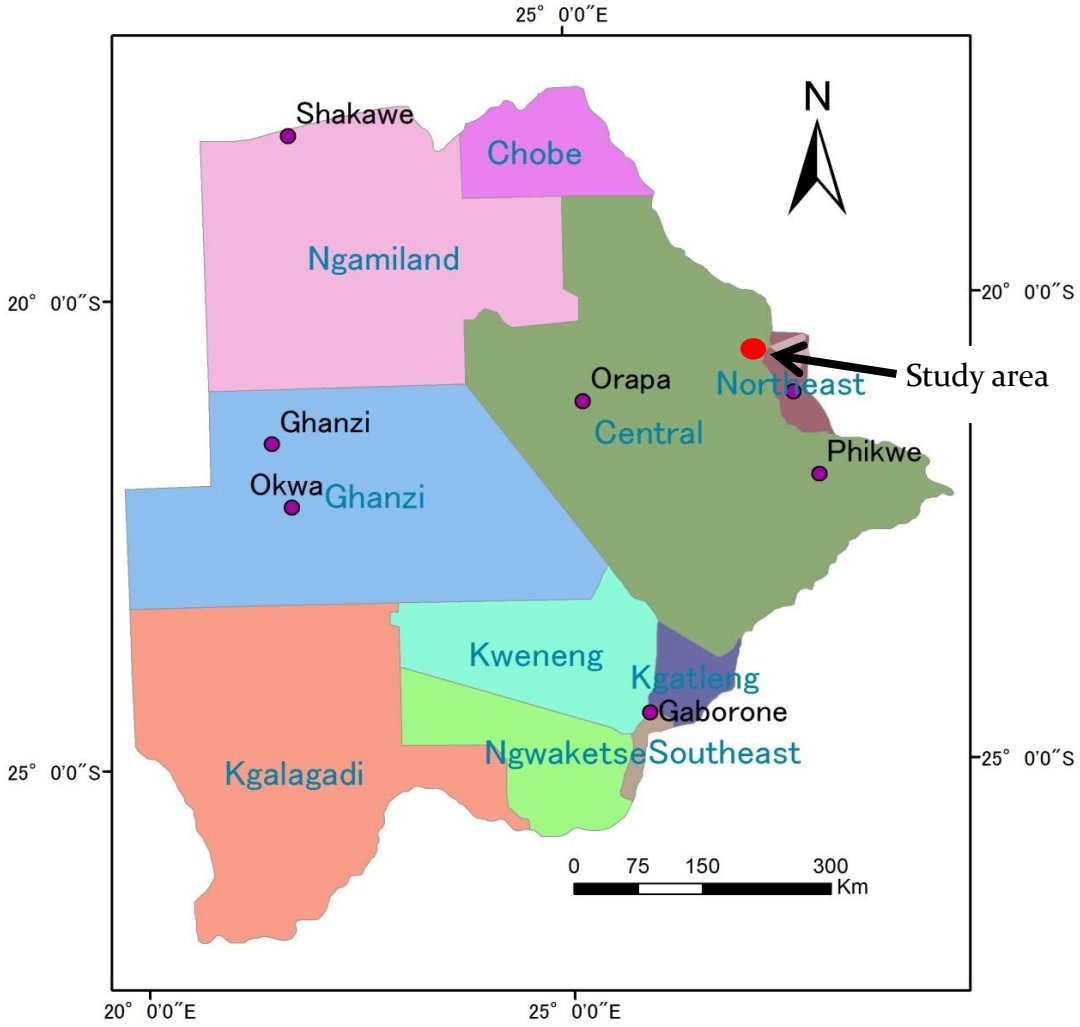

Figure 1: Map of Botswana showing the location of the study area (modified after Carney et al., 1994).

Figure 2: Topography around the Mowana deposit mining pit.

1.3 Exploration history and previous works

The exploration history of Mowana is summarized from the African copper 2005 company report. Exploration history for the Mowana ore deposits dates back to 1960's in an area covering approximately 319 square kilometers (African Copper, 2005). Initially in 1953 the then Bechuanaland Geological survey conducted geological mapping, geophysical surveying and several drill holes which lead to the discovery of the Dukwi oxide resource (African Copper, 2005). Thereafter the major exploration period commenced in 1959 through 1974 with the then Bamangwato concessions limited (BCL) which was a subsidiary of the Rhodesian Selection Trust (African Copper, 2005). The BCL conducted geological mapping, trenching and limited diamond drilling of 6 holes (1,462 m) between the years of 1962 and 1963. Further exploration continued from 1972 to 1974 with extensive drilling using several methods which include diamond drilling of 5 holes (717.5 m), halco drilling of 61 holes (4,250 m) and

wagon drilling of 404 holes of unknown meterage (8,725 samples) (African Copper, 2005).

Post expiration of the BCL license Falconbridge Explorations (Botswana) Limited took over with a major exploration program in the years 1977 to 1982. They extensively worked on collation of previous data, additional geological mapping, chip sampling of ancient small-scale underground workings dating as far back as 1910 to 1915, geochemistry and geophysical surveys (African Copper, 2005). These works were done to assess the deeper parts of the mineralization to check the possibility of an underground mine (African Copper, 2005). Diamond drilling was conducted on 78 drill holes (19,894 m) upon which a feasibility study on the deposit was produced in 1990 reporting 13Mt at a grade of 3.85% Cu (African Copper, 2005). However, the results proved futile for the mining infrastructure cost which led to the company letting their license lapse in 1993 (African Copper, 2005).

1992 saw the Messina Investments Limited (Minvest) acquiring the exploration rights to the Dukwi deposit through their subsidiary Messina Copper Botswana. They conducted and completed metallurgical sampling (African Copper, 2005). Further drilling which total 6800m of both diamond and reverse circulation was done to confirm an idea that the chalcopyrite mineralization was capped by an oxide blanket (African Copper, 2005). These resulted in confirmation of a deep seated hypogene chalcopyrite zone overlain by the supergene chalcocite at intermediate depths which is in turn covered by an extensive mixed copper oxide-copper carbonate cap at shallower depths (African Copper, 2005).

In 1996 Mortbury after purchasing Minvest acquired the rights. They drilled 26 holes (4,441m) using reverse circulation (RC) and percussion drilling as well as

rehabilitation of Bushman shaft for access to -60 m and -30m (African Copper, 2005). The main objectives of the drilling were to infill the previous drilling pattern and to better examine the mineralization at shallower levels to boost the confidence of the open pit option (African copper, 2005). In 2002 Mortbury produced a feasibility study for the near surface portion (oxide and supergene) of the Dukwi deposit (African Copper, 2005). The report focused on the technical and economic viability of an open pit heap-leach solvent extraction-electrowinning (SX/EW) option (African Copper, 2005). Further updates from the technical study by the MDM Ferroman (pty) Ltd of South Africa with influence from the hike of commodity prices deemed the project economically viable in 2004 (African Copper, 2005). The open pit option was postponed due to several factors including the high strip ratio in the open pit and high mining costs among others (African Copper, 2005). Therefore, they focused on underground mining and construction of a flotation concentrator (African copper, 2005).

African Copper PLC took over the project in 2004 and conducted additional drilling and metallurgical tests upon which a feasibility study was produced with reference to several consultancy companies (African Copper, 2005). The project was commissioned in 2008 and had a production rate of 100, 000 t/ month from the open pit and 1.2 Mtpa processing plant (Newall et al. 2018). The total copper resources stood at more than 100Mt at an average grade of 0.94% (Newall et al., 2018). Unfortunately, in 2015 African Copper had to close due to several reasons including high working capital, high debts and falling copper prices hence put under liquidation by year end (Newall et al., 2018).

Since mid-March 2017, Cradle Arc Investments through Leboam Holdings (Pty) Ltd operated the mine (Newall et al., 2018). The company had a daily production of low-grade copper concentrate estimated at 100t per day (Newall et al., 2018).

1.4 Thesis statement and objectives

Although there has been some mapping, drilling and even mining conducted in the deposit area, the Mowana deposit has since received very little documentation. The formation of the deposit and characteristics is still unclear. Moreover, the Mowana deposit is a unique kind of deposits since the main mineralization is copper associated with a shear zone and hosted within a greenstone belt. More often the Archean greenstone belts host Au mineralization as opposed to Cu. This thesis focuses to document the characteristics of the Mowana deposit. This entails but not limited to, the geology, the mineralogical characteristics, and the source of the ore forming fluids of the deposit. The following objectives will be addressed in this study;

(a) To document the host rock lithologies and their textural features.
(b) To document the types, and characteristics of the mineralization and to develop a paragenetic sequence of the different mineralization stages
(c) To understand the mineral chemistry of the different ore minerals in order understand the characteristics of the hydrothermal fluids
(d) To determine the source of ore forming fluids and mineralization formation temperature for the deposit

1.5 Thesis organization

This thesis has been divided in to 8 chapters. The early chapters provide summary of the available literature on the geological framework, metallogeny and geochronology of the north east complexes in Botswana. Chapters 3 to 7 are the main parts of this thesis. Chapters 4 to 7 contain the introduction, methodology, results,

discussion and conclusions subsections. Chapter 8 presents the summary of the main findings established in this thesis. Most of the findings in chapter 3 to 7 have been collated into a paper entitled “Geology, mineralogy, and sulfur isotopes of the Mowana copper deposit, Matsitama Schist Belt, NE Botswana”. This paper has been submitted to Resource Geology and was accepted for publication in February 2021. The paper is authored by Amogelang Kooganne with Dr. Andrea Agangi, and Dr. Ryohei Takahashi of Akita University as co-authors.

CHAPTER 2: REGIONAL GEOLOGY AND TECTONIC SETTING

2.1 Introduction

This chapter provides a review on the geological framework of Botswana, the metallogeny of the north eastern complexes including the Matsitama Schist Belt, and the geochronological correlation these complexes in Botswana. The subsections summarize the findings of several researchers including tectonic studies, regional geologic mapping, mineral resource exploration within the Limpopo Mobile Belt and Zimbabwe Craton in Botswana**.**

The geology of Botswana is quite diverse and complex. Its geological record ranges from Archean to Phanerozoic (Carney et al., 1994). Brief description of each Eonothem Eon is given below with reference to Figure 3.

The oldest rock units in Botswana are composed of the Archean basement sequences which are outcropped only in the east of the country (Carney et al., 1994). These basement terranes are divided into the Kaapvaal Craton, Zimbabwe Craton, and Limpopo Mobile Belt collectively referred to as the Kalahari Craton (Carney et al., 1994). The Kaapvaal craton occurs to the south of the Limpopo belt. Granitoids and gneisses, as well as the greenstone belts of the Kraaipan Group of about 3.0 Ga, form the basement units in the south and southeastern part of Botswana (Wormald and Downey, 1999). The basement was intruded by Gaborone Igneous Complex which was emplaced at 2.8 Ga (Wormald and Downey, 1999). The Gaborone igneous complex composes of the two groups, the Gaborone granite and the Lobatse Group (Wormald and Downey, 1999). According to Wormald and Downey, 1999, the

Gaborone granite consists of porphyritic rapakivi Thamaga granite which graded into equigranular inner marginal phase called the Kgale granite and the outer marginal

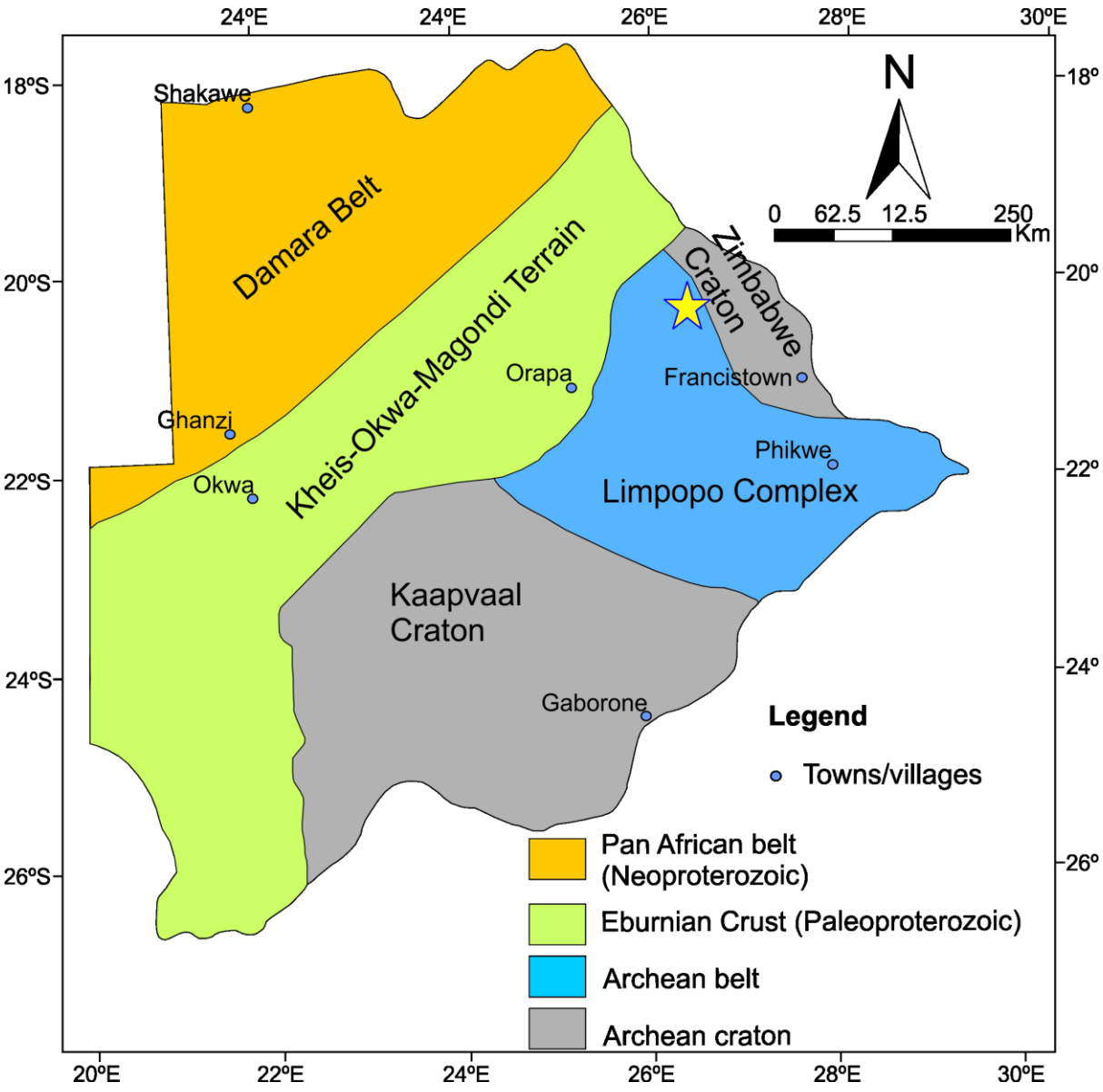

Figure 3: The geological map of Botswana. The location of the study area is represented by the yellow star (modified after *McCourt* et al*., 2004; Chisenga et al. 2020*).

phase called the Ntlhantlhe microgranite. The Lobatse Group is made of the Kanye Volcanic Formation, the Nnywane and Mogobane Formations, which consist of massive rhyolites, volcanoclastics rhyolite and argillaceous sediments, respectively (Wormald and Downey, 1999).

A large proportion of the geological framework of the northeastern Botswana comprises the Zimbabwe Craton and the Limpopo Belt. From here on the discussion will focus on these 2 terranes.

The 800 km long and about 500 km wide, NE trending, oval shaped Archean Zimbabwe Craton has been described as a composite granite-greenstone terrane (Prendergast, 2004). The Zimbabwe Craton is mainly confined to Zimbabwe, with an extension into NE Botswana, where it occupies an area of about 60,000 km^2 equating to about 15 % of the entire country (Carney et al., 1994). However, since the westernmost boundary of the craton is concealed beneath the Phanerozoic cover rocks and the southern boundary is not defined, the full extent of the craton is unspecified (McCourt et al., 2004). It includes numerous remnants of supracrustal successions and tonalite-trondhjemite-granodiorite (TTG) intrusions spanning in age from the Paleoarchean to the Neoarchean (Fig. 4; Blenkinsop et al. 1997; Jelsma and Dirks, 2000; Hofmann and Chagondah, 2019). The oldest preserved rocks of the Zimbabwe Craton are represented by TTG gneiss of the Tokwe Terrane (3.6 – 3.5 Ga) (Fig. 4; Kusky, 1998). However, detrital zircon grains preserved in the quartzites from the greenstone belts in Zimbabwe have yielded ages up to ca. 3.8 Ga (Dodson et al., 1988; Bolhar et al., 2017).

The collision of the Zimbabwe Craton and the Kaapvaal carton in the south resulted in the formation of the generally E-W trending Neoarchean mobile belt which has been interpreted as the suture zone between these Cratons (Carney et al., 1994, McCourt et al., 2004). The lithological units of the Limpopo Mobile Belt have been complexly deformed and metamorphosed at amphibolite to granulite facies (Carney et al., 1994, Barton et al., 1994, Maier et al., 2008; Van Reenen et al., 2019). The Limpopo Mobile Belt is divided into three distinct zones based on photogeological

techniques as well as compositional and structural differences; these are the Southern Marginal Zone, Central Zone, and Northern Marginal Zone (Carney et al., 1994, Khoza et al., 2013; Van Reenen et al., 2019; Fig. 2). The NMZ lies mainly in Zimbabwe and comprises the granite-greenstone material, is separated from the Zimbabwe Craton by the southward-dipping North Limpopo Thrust Zone (NLTZ). The southern limit of the NMZ (northern limit of the CZ) is marked by the south-dipping Triangle Shear Zone (TSZ). The Northern Marginal Zone is contiguous with the Matsitama-Motloutse Complex to the west in Botswana (McCourt et al., 2004).

The Central Zone, which occupies the largest area of the three zones, contains various Archean supracrustal rocks commonly intruded by a variety of orthogneisses and anorthositic gabbroic rocks. (Fripp et al., 1979; Watkeys et al., 1983, Van Reenen et al., 2019). The Central zone has experienced two sets of metamorphisms between 2.7-2.6 Ga (Smith et al., 2011), hence complex fold pattern. U-Pb zircon ages of gneiss granitoids from the Central Zone are mainly in the range 2734±4 and 2637±3 Ma (Kampunzu et al., 2003). The ENE to NE trending shear zone referred to as the Palala-Tshipise shear zone separates the CZ from the SMZ in NE South Africa.

The Southern Marginal Zone consists chiefly of enderbitic and charnokitic gneisses and has experienced only a single metamorphic event at 2.72-2.65 Ga (Smit et al., 2011). SMZ is disjointed from the Kaapvaal craton to the south by a north-dipping Hout-River Shear Zone (HRSZ). Thus, Zimbabwe Craton is juxtaposed to the Limpopo mobile belt to the south and truncates into the Proterozoic Magondi belt along the western margin.

In northeast Botswana, the geology includes the transition between the Zimbabwe Craton and Limpopo Mobile Belt to the south (McCourt et al., 2004). The geology in

this area has been divided into distinct tectonostratigraphic complexes (McCourt et al., 2004). The complexes include the Francistown Granite-Greenstone Complex, the Matsitama-Motloutse Complex, and the Phikwe Complex (McCourt et al., 2004). These distinct Archaean crustal complexes are attributed to the accretionary processes that resulted in their amalgamation during the Neoarchean (McCourt et al., 2004).

Francistown Arc complex

The Francistown Granite-Greenstone Complex is regarded as a continental-margin (volcanic arc) that developed between 2.75 and 2.60 Ga (Bagai et al., 2002, McCourt et al., 2004). This complex constitutes the southwestern margin of the Zimbabwe craton in Botswana (Carney et al., 1994). The Francistown Complex is a composite granitoid-greenstone terrane comprising three individual greenstone belts associated with voluminous granitoid suites, minor mafic intrusions and wide distribution of gneisses (Carney et al., 1994; Bagai, 2002; Kampunzu et al., 2003). The complex consists of the typical Tati, Vumba and Maitengwe greenstone belts which essentially consist of volcanic rocks (Carney et al, 1994; McCourt et al., 2004). The basement rocks of the Tati and Vumba granite-greenstone belts comprise essentially of basic metavolcanics rocks with a substantial amount of ultramafic components (Carney et al, 1994; McCourt et al., 2004). The upper part of the sequence is composed of intermediate and acid volcanic members (Litherland, 1975; Majaule et al., 1997). The granitoids enclose all these belts lithologies (Carney et al., 1994; Majaule et al., 1997) The belts are deficient of sedimentary components (Litherland, 1975; Majaule et al., 1997). The Maitengwe granite-greenstone belt consist of compositionally the same

lithologies (Aldiss, 1991). The basement rocks consist of Banded Iron Formation (BIF) overlain by an ultramafic formation comprising serpentinites, meta-peridotites, and amphibolite (Aldiss, 1991). The rocks in these belts have been associated with the Upper Greenstone Belts of Zimbabwe based on geochronology (Aldiss, 1991) as it will be shown in the next subsection. The rocks have been metamorphosed in the greenschist up to lower amphibolite facies although granulite facies rocks have been reported particularly in the Vumba belt (Carney et al., 1994; McCourt et al., 2004). The greenstone belts were subsequently intruded by several episodes of granitoids including tonalities, granodiorites, monzonites, and post tectonic granites (Carney et al., 1994; McCourt et al., 2004). A ductile shear zone separates the Francistown Arc Complex to the South (McCourt et al., 2004 and references therein).

Phikwe Complex

The Phikwe Complex is included within the generally E-W trending Neoarchean high-grade metamorphic Limpopo Mobile Belt, specifically in the Central Zone (Carney et al., 1994; McCourt et al., 2004; Van Reenen et al., 2019). Deformed and metamorphosed amphibolites, various granitoid gneisses intruding the supracrustal rocks with minor ultramafic rocks and younger granites characterize the geology of the Phikwe Complex (McCourt et al., 2004; Van Reenen et al., 2019).

Matsitama-Motloutse Complex

The Matsitama-Motloutse, Phikwe and Mahalapye Complexes are included within the high-grade metamorphic Limpopo Mobile Belt, specifically in the Central Zone (Carney et al., 1994; Smit et al., 2011; McCourt et al., 2004). The Matsitama-

Motloutse Complex is an accretionary assemblage which was accreted on to the Francistown Arc Complex as a result of northward subduction along the Shashe Shear Zone (Carney et al., 1994; Majaule et al., 1997). Previously Matsitama-Motloutse Complex was considered as part of the Zimbabwe Craton, however, Ranganai et al. (2002) and McCourt et al. (2004) concluded that the Matsitama-Motloutse Complex is the extension of the Limpopo Mobile Belt.

The Matsitama-Motloutse Complex is mainly composed of continental margin-type supracrustal rocks (Majaule et al., 1997). The rocks have been tightly intruded by the granitoids (Carney et al., 1994). The complex is dominated by sedimentary sequences which also have been deformed and metamorphosed in the greenschist to lower amphibolite facies (Carney et al., 1994; McCourt et al., 2004). The composition of the intruding granitoids is heterogeneous and seems syntectonic (Aldiss, 1991; Carney et al., 1994; McCourt et al., 2004).

The late Archean in age Matsitama Schist Belt within the Matsitama-Motloutse Complex, is one of the greenstone belts of North eastern Botswana (Hall and Hughes, 1997). Previously the belt has been considered to be part of the Zimbabwe Craton. However, since the copper mineralization dating age of ~2.0 Ga has been obtained from the Bushman shear zone the belt has been linked to the Magondi orogenesis which is post-Archean hence attributing some of the deformation in the Matsitama area to the formation of the Magondi belt (Majaule et al., 1997). The belt has been metamorphosed to greenschist facies to amphibolite facies (McCourt et al., 2014). Lithologically the main constituents of the belt are metasediments including carbonates, pelites, conglomerates and minor ultramafic metavolcanics towards the base of the stratigraphy. According to Hall and Hughes 1977; Coomer et al., 1977; Majaule et al., 1997, the Matsitama greenstone belt exhibit distinct features from other

greenstone belts in north east Botswana. These include the high dominance of metasedimentary rocks in the stratigraphic sequence whereas the mafic and ultramafic rocks are infrequent (Majaule et al., 1997). Intermediate volcanic rocks are rare and show slight lithological and chemical variations, whereas the acidic volcanic rocks are virtually absent in the belt (Majaule et al., 1997; McCourt et al., 2004). Botrill (1998) indicated that the absence an acidic volcanic component signifies a different depositional setting for the Matsitama Schist Belt compared to other greenstone belts of the Zimbabwe Craton. The Cu-Ag mineralization in the Matsitama Schist Belt is distinctively hosted by the calcareous metasedimentary rocks and graphitic schists with little or no gold mineralization, in contrast to the aforementioned granite greenstone belts (Majaule et al., 1997).

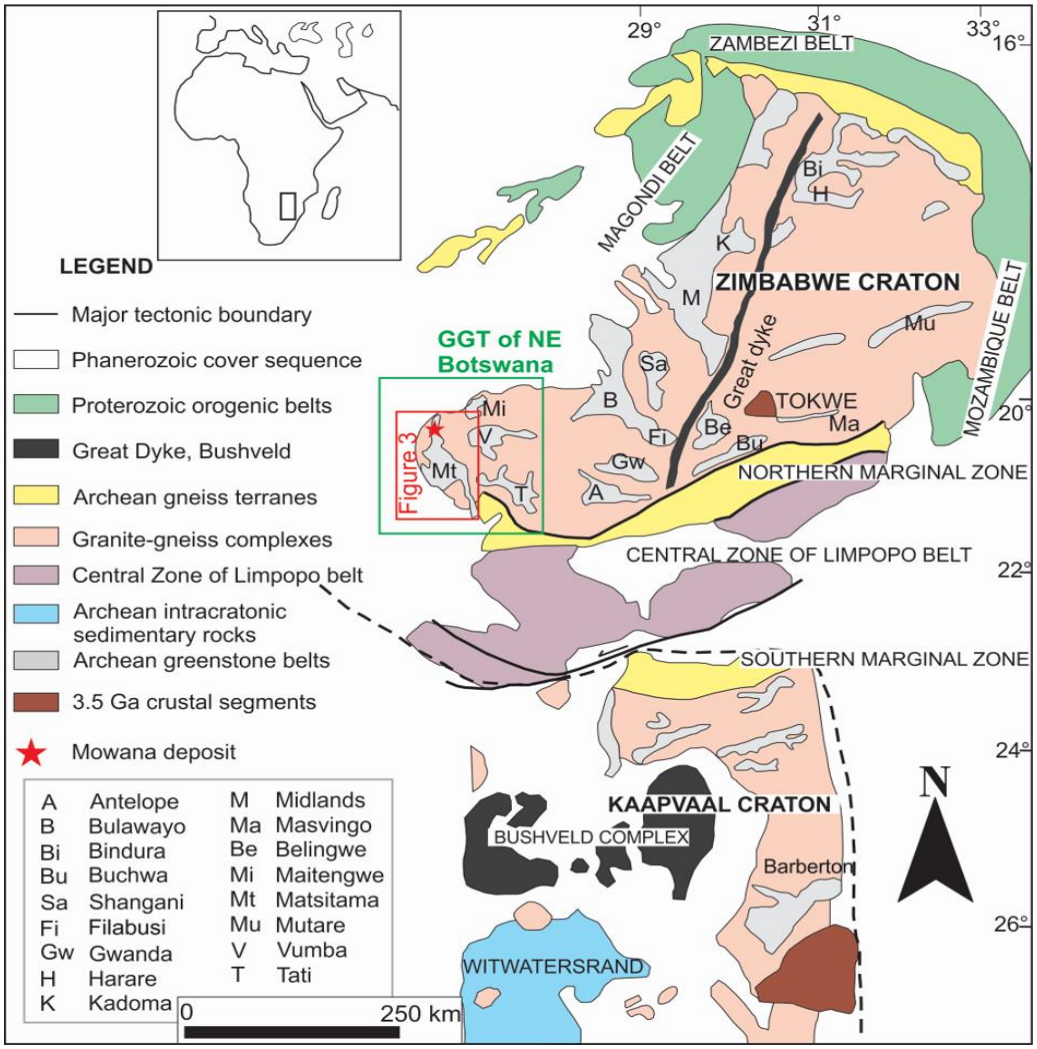

Figure 4: Main geological units of southern African cratons and adjacent Proterozoic belts. The inset shows location of the Kalahari Craton (Zimbabwe and Kaapvaal Cratons) in Africa. The green rectangle labelled GGT represent the distribution of four main granite-greenstone terranes (GGT) of the Zimbabwe Craton in NE Botswana. The red rectangle indicates the position of figure 3 (*modified after Bagai et al., 2002 and references therein*).

Proterozoic belt terranes occur along the western margins of the Kaapvaal-Zimbabwe Cratons as shown in Figure 3. The oldest Proterozoic rocks were formed during the Paleoproterozoic Eburnian tectonothermal event and constitute the Kheis-Okwa-Magondi Belt (Carney et al., 1994). The main lithologic units comprising the Kheis-Magondi Belt include granitoids and metamorphic assemblages (Carney et al., 1994). Farther to the northwest, lies a complex of Neoproterozoic terrane made up of the Ghanzi-Chobe Belt and Okavango-Shakawe Zone (Carney et al., 1994). These terranes consist of basement rocks deformed during the Kibaran and again during the Pan-African tectonothermal events (Carney et al., 1994).

Phanerozoic successions which are mainly characterized by the Karoo Supergroup and the Kalahari red beds overlie the basement rocks and cover a large area of about 75 % of the Botswana's surface area (Carney et al., 1994). The Karoo Supergroup largely composed of sedimentary and volcanic rocks unconformably overlie the Archean and Proterozoic rocks (Carney et al., 1994). The north-easterly trending faults and northwest trending faults control the distribution of the Karoo Supergroup (Barton et al., 1994). The Karoo Supergroup are subsequently overlain unconformably by the Kalahari beds (Carney et al., 1994). The Kalahari beds are mainly characterized by aeolian sands (Carney et al., 1994).

2.2 Mineralization in the northeastern part of Botswana

The northeastern part of Botswana is endowed with several mineralization in different styles (Fig. 5). The Francistown complex is enriched in Gold mineralization hosted in NW trending zones, particularly in the sheared zones (Aldiss, 1991, Carney et al., 1994). Minor enrichments in copper, lead and zinc are notable in this area (Aldiss, 1991). Antimony-arsenic, bismuth and tungsten veins occur sparingly (Aldiss, 1991).

Nickel-copper mineralization is intimately associated with the basic intrusive rocks of the Tati group (Aldiss, 1991). Based on high copper-nickel ratio, the deposits are categorized as Archean mafic intrusive as opposed to the Komatiite hosted Archean nickel deposits (Aldiss, 1991). Relatively high contents of Co, Pd and Rh have been reported (Aldiss, 1991).

Matsitama-Motloutse complex is sparingly mineralized with similar Cu associations (Carney et al., 1994). Volcano sedimentary successions of this mainly host copper as the main base metal (Aldiss, 1991; Carney et al., 1994). The mineralization is hosted in the north trending mylonitized and quartz enriched rocks including carbonate and biotite-schist (Aldiss, 1991).

The Matsitama Schist Belt hosts numerous individual occurrences of either Cu, Pb-Zn, Ag, and Ni mineralization within four main areas which include: Mowana, Lepashe Copper Snake, and a line of deposits and prospects extending from Mutsuku to Nakalakwana Corridor (African Copper, 2008; Fig. 6). The Mowana Cu deposit is hosted by the Bushman Lineament and consists of epigenetic, structurally controlled Cu-Pb-Zn±Ag sulfide mineralization (African Copper, 2008). The Thakadu, Makala, Mutsuku, and Nakalakwana, forming a linear pattern, share many similarities with the Mowana Cu deposit in terms of the nature of deposition and relative timing of

mineralization (Davis, 2009). The structural context and mineralization of the Thakadu Cu deposit are better understood owing to the extensive mapping in the surrounding region carried out by Davis (2009). It is hosted by a series of high-strain zones and folded beds, which give it in some parts a curvilinear shape (Newall et al., 2018). Based on a resource estimation by Newall et al. (2018), the Thakadu deposit contained 963.9 Mt of mineral resource at 1.32 wt% Cu grade and 0.25 % Cu cut-off grade, and 1.77 Mt at 12.03 g/t Ag. The Cu mineralization (chalcopyrite) overprinted quartz-carbonate alteration (Davis, 2009; African Copper PLC, 2008). Based on Pb isotopes, Coomer et al. (1977) concluded that the mineralization at Thakadu, in the Matsitama Schist Belt occurred at approximately 2.2 Ga. The Makala Cu-Pb-Zn-Ag deposit, situated between Thakadu and Mutsuku deposits, contains a resource of 10.27 Mt at 1.18 wt% Cu (Newall et., 2018). The Nakalakwana corridor is a Cu-Au-Ag prospect that contains 9.9 Mt of protore at 0.46 wt% Cu (Newall et al., 2018). The Lepashe Copper Snake is composed of four prospect areas which generally contain Cu-Ni-Cr-V mineralization (African Copper PLC, 2008). However, some prospects may contain anomalous concentrations of Au often detected from soil anomalies (African Copper PLC, 2008).

2.3 Geochronology and correlation of the northeast complexes

Several geochronological data have been obtained using various dating methods, in a quest to assign absolute ages to the different lithologies in the area. Absolute dating underpins the exploration of particularly magmatic-hydrothermal deposits, since the time-dependent fertility of magmas is paramount (Selly et al., 2018).

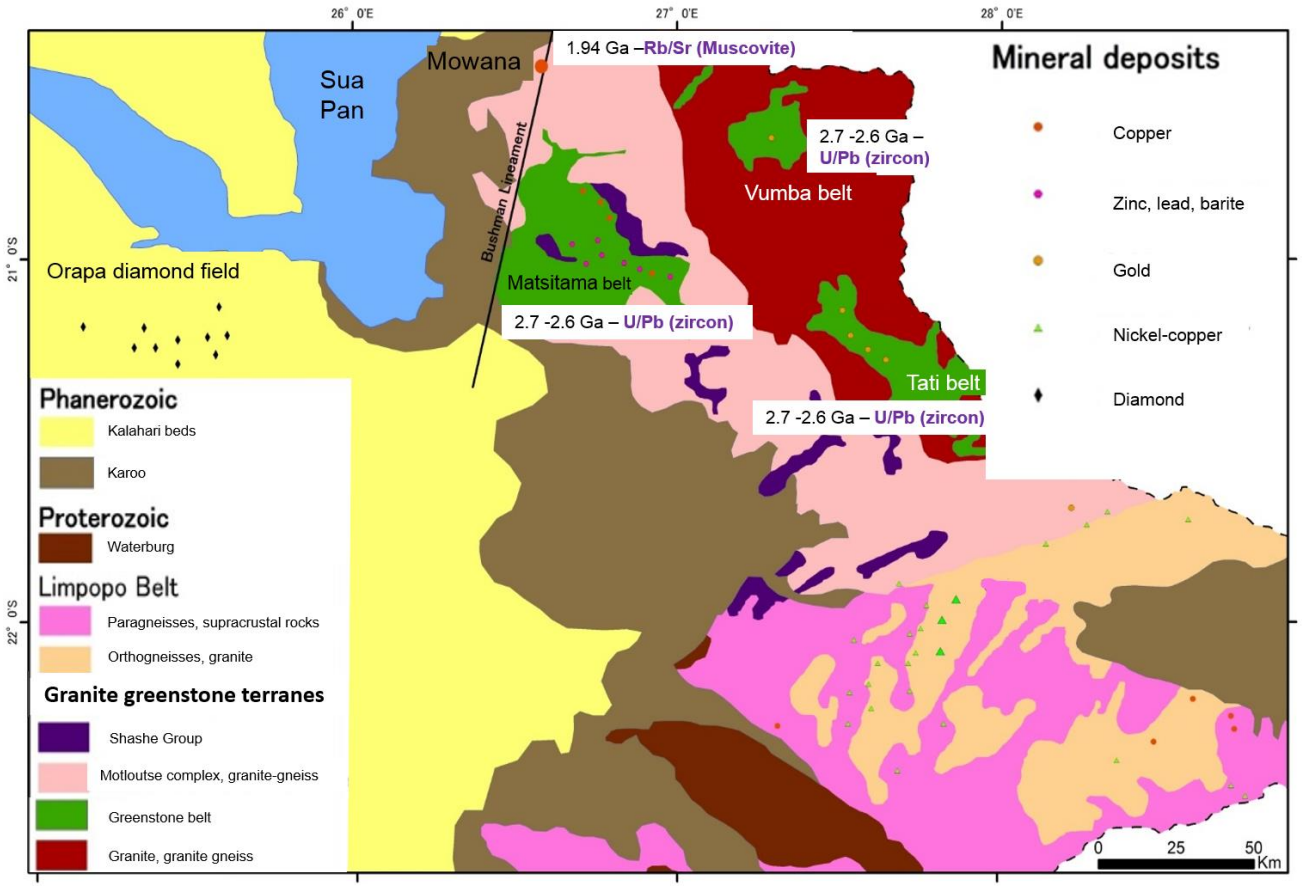

Figure 5: Regional geology and mineral deposits of North-east Botswana (modified after Newall et al., 2018).

The ages summarized here were obtained through the modern high precision U-Pb dating method. The 3.6 - 3.5 Ga Tokwe Terrane, which hosts greenstone enclaves of the Sebakwean Group, represents the oldest section of the granitoid crust in the Zimbabwe Craton (Figure 2; Wilson et al. 1995, Hoffman et al., 2003). The Paleoarchean magmatism ceased at approximately 3.4 Ga with the intrusion of the Mushandike and Mont d'Or Granitoids (Hoffman and Chagondah, 2019). The Upper greenstones of the Zimbabwe Craton have an emplacement age of approximately 2.7 Ga, concomitant with the tectonic and magmatic events (Aldiss 1991; Hofmann et al.,

2003; Hofmann and Chagondah, 2019). The 2.6 Ga regional metamorphism led to the emplacement of voluminous Chilimandzi Granites, which initiated the stabilization of the craton (Wilson et al. 1995; Hoffman and Chagondah, 2019 and references therein) with the subsequent intrusion of the 2.57 Ga layered igneous complex of the Great Dyke (Oberthür et al., 2002).

Bagai et al. (2002) reported the age of the TTGs around the Vumba Greenstone Belt as 2.69 to 2.64 Ga, which was contemporaneous with the age of the volcanic rocks in the Vumba Greenstone Belt. The Matsitama Granitoids are time-correlative to the Vumba Granitoids, since similar U-Pb ages were documented for the tonalitic gneisses of the Mosetse Complex (2.71 to 2.64 Ga; Majaule and Davis, 1998). U-Pb zircon geochronological data placed the Tati Granitoids within the same emplacement age bracket of ~2.73 to 2.65 Ga (Bagai et al., 2002). All these somewhat younger and similar ages support that the greenstone belts in the Francistown complex in Botswana are correlative to the Upper Greenstone Belts in Zimbabwe (Carney et al., 1994).

Based on Pb isotopes, Coomer et al. (1977) concluded that the mineralization at Dihudi and Thakadu leads, in the Matsitama Schist Belt occurred at approximately 2.2 Ga.

Magmatism in the Motloutse Complex indicated an Archean emplacement age of ~2.7 Ga to 2.6 Ga (Holzer et al., 1999). McCourt et al. (2004), dated the detrital zircons obtained from the quartzites of the Motloutse Complex which indicate a provenance from rocks with the age range between 2.74 and 2.68 Ga and a maximum deposition age of ~2.66 Ga. A lateral temporal correlation has been inferred between the Motloutse and the Matsitama Schist Belt, following the record of similar detrital zircon ages from the Matsitama Schist Belt (in the range from 2.69 to 2.63 Ga; McCourt

et al., 2004). The upper intercept ages provided by the zircons from the granitoids of Phikwe Complex are 2.61 Ga and 2.65 Ga, and a concordant age of 2.66 Ga (McCourt et al., 2004) Younger granites within the Phikwe Complex indicated ages of 2.65 Ga and 2.60 Ga (McCourt and Armstrong, 1998).

CHAPTER 3: DEPOSIT GEOLOGY

3.1 Lithologic units

The Matsitama Schist Belt consists of four lithological assemblages (Fig. 3). The basal Sebotha-Mosupe Formation consists of ultramafic and mafic units with minor limestone and quartzite (Botrill, 1998). These are overlain by a fining upward sedimentary sequence which is informally referred to as the Bushman Mine “Group” (Davis, 2009). The Bushman Mine “Group” is subdivided into a formation, and facies, namely the Palamela Formation, and Lepashe River -Nakalakwana, and Mmalogong Facies (Carney et al., 1994; Davis, 2009). In other literature (e.g., Majaule 1997) these divisions are referred to as associations. The Palamela Formation consists of metasedimentary rocks; mica-schists, and carbonates interbedded mafic volcaniclastic rocks and coarser clastic sedimentary rocks (Carney et al., 1994; Majaule et al., 1997). Metasedimentary rocks, metavolcanics and ferruginous quartzites which are overlain by the Lepashe River conglomerate constitute the Lepashe River – Nakalakwana Facies (Carney et al., 1994; Majaule et al., 1997). The Mmalogong Facies is constituted by ferruginous quartzo-feldspathic sandstones and red beds (Botrill, 1998; Davis, 2009). The Matsitama Schist belt has been deformed and metamorphosed during an orogenic even whereby the sedimentary rocks of the Bushman Mine group were thrust over the older granite-gneiss terrane along with a series of thrust and nappe structures (Majaule et al., 1997, Davis 2009).

The Mowana Cu deposit is located in the northern part of the Matsitama Schist Belt (Fig. 3) in a narrow strip of dominantly folded metasedimentary rocks which

probably belong to the Lepashe River Facies of the Bushman Mine “Group” (Botrill, 1998). The deposit is hosted by the N-NE striking and nearly vertical dipping sliver known as the Bushman Lineament, which overprinted the carbonaceous, argillaceous metasediments and graphitic schists that host the Cu-bearing quartz-carbonate breccias (Barton et al., 1994). These units are enclosed by granitic gneisses of the Neoarchean to Paleoproterozoic (2.57-2.3 Ga; Barton et al., 1994) Matsitama-Motloutse Complex forming a large sedimentary basin on the Zimbabwe Craton (Majaule et al., 1997; Barton et al., 1994; Fig. 6). The Bushman lineament, located to the northern margin of the Matsitama Schist Belt, is one of the prominent and extensive structures which were produced contemporaneous with the regional deformation (<2.0 Ga; Kamber et al., 1993, Barton et al. 1994). The lineament, which is dominated by brittle deformation, is a major shear zone extending for more than 6.5 km northwards and up to 300 m wide (Barton et al., 1994).

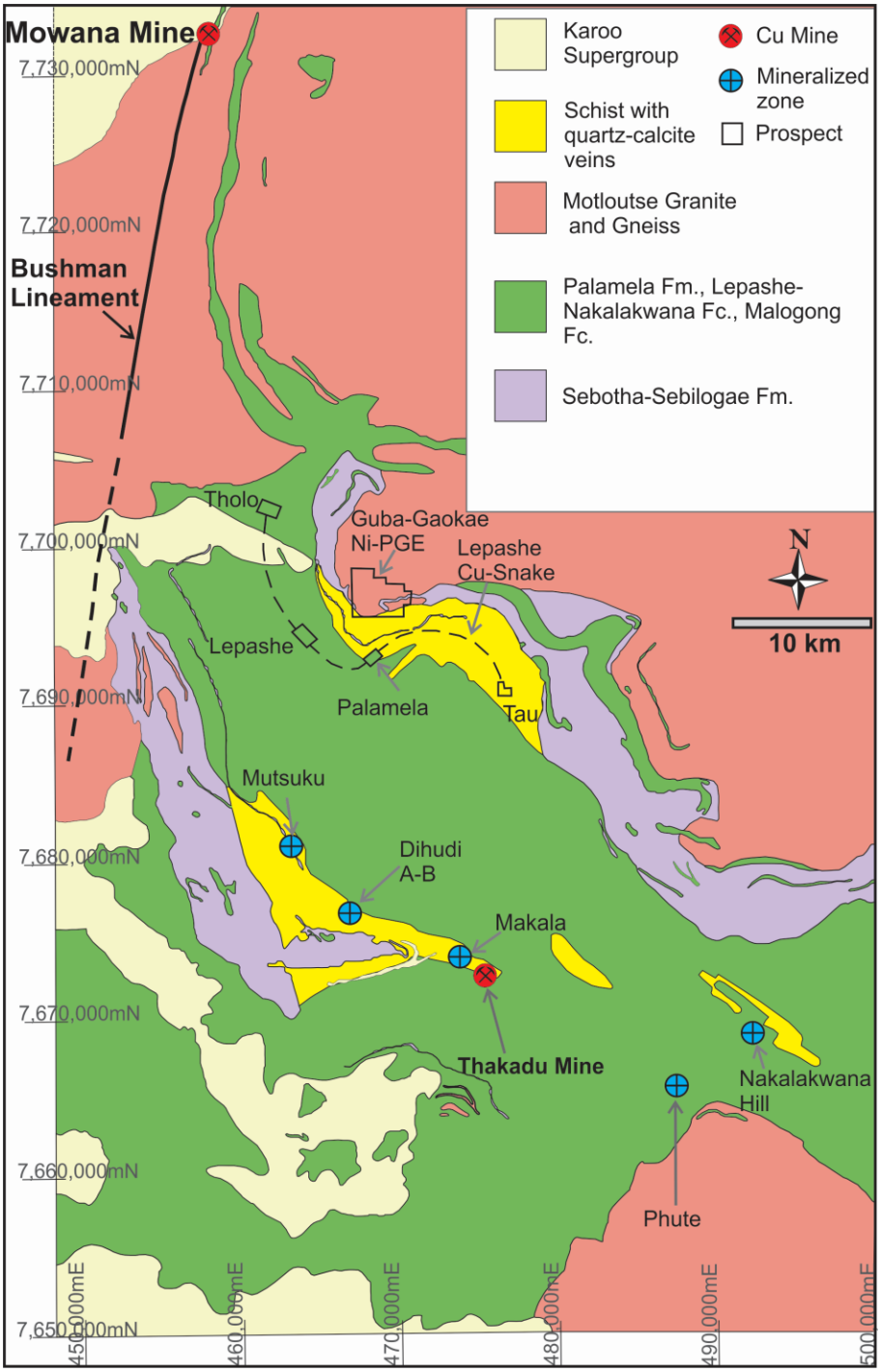

Figure 6: Geological map of Matsitama Schist Belt and surrounding granite-gneiss terranes (modified after Davis, 2009). Abbreviations; Fm., Formation; Fc., Facies.

3.2 Deformation and structures

The structural geology of NE Botswana is dominated by the Limpopo Mobile Belt. The formation of the Limpopo Mobile Belt had a major influence on the deformation of the adjacent cratonic areas (Davis, 2009). The Matsitama Schist Belt has a complex geometry defined by the WNW-to NW striking structural grain that is folded around NE striking folds and is related to the accretion of the Matsitama-Motloutse Complex to the Francistown Arc Complex (Carney et al., 1994; Davis 2009). Deformation of the Precambrian rocks commenced with NE-SW to N-S shortening associate with the accretion of the Matsitama-Motloutse Complex to the Francistown Arc Complex, which represents the SW margin of the proto-Zimbabwe Craton and the evolution of the Limpopo belt (Carney et al., 1994; Davis 2009). This initial deformation was followed by a major NW-SE shortening that a large scale was non-coaxial and resulted in clockwise rotation of the Matsitama Schist Belt (Carney et al., 1994). It also formed NE-SW striking folds with vertical axial planes and cleavage (Carney et al., 1994). Copper mineralization post-dated the formation of these folds (Davis, 2009).

Previous researchers recognised two stages of deformation that formed the WNW structures and folding of these structures by NW-SE shortening to produce folds with NE-striking axes (Key et al. 1976; Coomer et al. 1977; Botrill, 1998; McCourt et al. 2004). The most recent detailed structural mapping conducted for the African Copper PLC has delineated six regional deformational events (D1-D6), four of which are considered to have played a critical role in the localization of Cu mineralization (Davis, 2009). D1 formed by SW-dipping thrusts and probably formed regional structure known as the Bushman Lineament (Davis, 2009). The Bushman Lineament is a brittle deformation structure formed by shearing strain which is consistent with the

interpretation of the regional relationships indicating that it is a thrust (Barton et al., 1994; Davis, 2009). The main D1 structures are a series of isoclinal folds (Davis, 2009). The second deformation (D2) formed upright folds with E-W striking axial planar fabric and high strain zones (Davis, 2009). This deformation is most readily recognised by its axial planar fabric as folds are rare (Davis, 2009). D3 was a return of the NE-SW shortening that formed upright folds NW striking and axial planar fabric (Davis, 2009). These fabrics are commonly host structures to prominent veins in the Mowana mining pit (Davis, 2009). D4 formed upright folds with NE striking axial planes and axial planar cleavage and high strain zones (Davis, 2009). These folds tend to NW vergent based on cleavage-bedding vergence relationships (Davis, 2009). D5 formed folds with sub-horizontal axial planes and sub-horizontal fabrics (Davis, 2009). These had a major impact on the localization of the mineralization (Davis, 2009). D6 involved the E-W shortening and the formation of a N-S subvertical cleavage (Davis, 2009). Copper mineralization in D6 was strongly influenced by existing structures as reflected by deposit geometry and structural relationships associated with alteration and copper deposits that can be observed in drill core and exposures (Davis, 2009). Summary of the deformation history is shown in Table 1.

The final post-mineralization deformation produced numerous NE-trending parallel faults that transected the mineralized breccia into three separate zones, namely from north to south: the Mapanipani North Zone, Mapanipani Zone, and Bushman Zone (Barton et al., 1994; Newall et al., 2018; Fig. 7). These faults also controlled the sedimentation of the Karoo Supergroup (Barton et al., 1994).

Table 2: Deformation history of the Matsitama Schist Belt

Event	Description
D1	NE-SW shortening. SW dipping high strain zones and fabrics on the SW margin of the Matsitama schist belt and NE dipping along the NE margin
D2	N-S shortening. E-W striking upright regional folds and axial planar cleavage and high strain zones
D3	NE-SW shortening. Rare folds and vertical cleavage.
D3	NW-SE shortening. NE-SW striking upright folds and high strain zones. Regionally partitioned with low strain zone across the middle of the belt
D4	Vertical shortening. Folds with horizontal axial planes
D5	E-W shortening. Sub vertical north-south striking cleavage. Folding of D5 axial planes. Reactivation of S2. Copper mineralization.

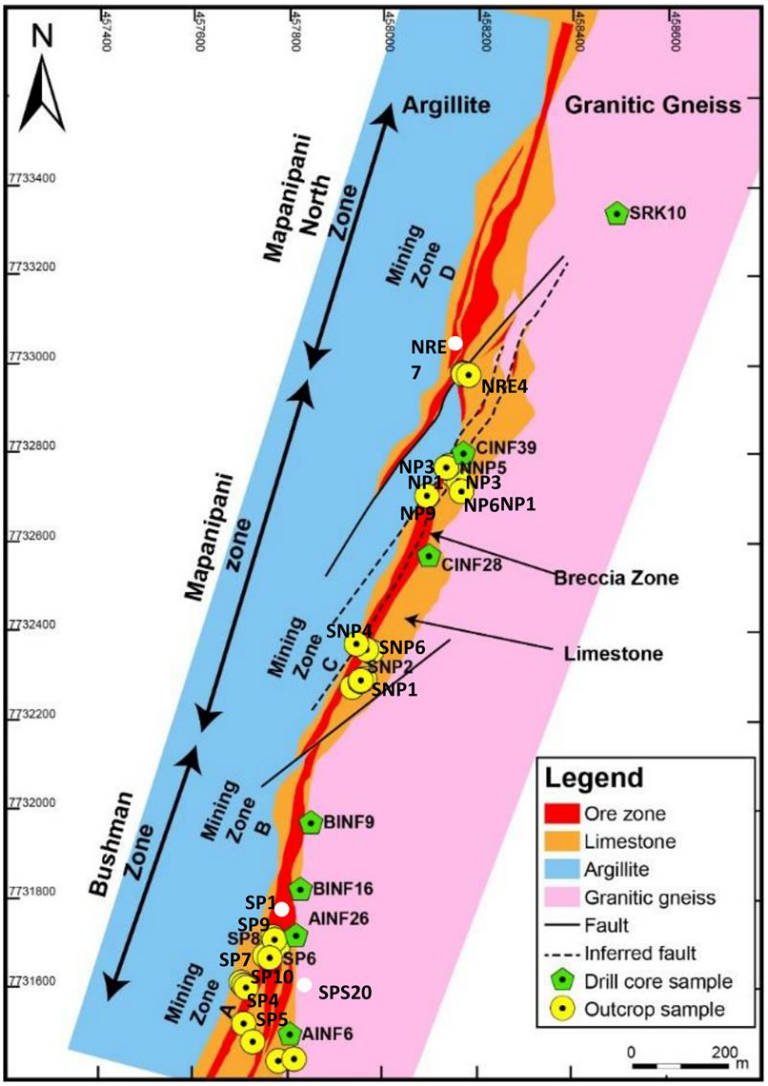

Figure 7: Geological map of Mowana deposit. Location of samples used in this study is indicated by the yellow and green symbols (modified after African Copper PLC, 2005).

CHAPTER 4: PETROGRAPHY AND MINERALIZATION

4.1 Introduction

The mineralization in Mowana deposit is hosted in a sliver of metamorphosed sedimentary rocks of the Bushman Mine group within the Matsitama Schist Belt. The mineralization is characterized by types of mineralized veins and breccias. This chapter aims to document the characteristics of the Mowana deposit. It aims to develop a paragenetic sequence of the different mineralization types and associated hydrothermal alteration through examination of the collected samples from the host rocks, quartz veins and breccias. The emphasis was also given to the ore mineral assemblages and textures.

4.2 Methodology

4.2.1 Fieldwork

Following desktop and reconnaissance study, 2 weeks fieldwork research was conducted at the Mowana deposit. The outcrop samples were collected from levels 980,960 and 940 m in an open mining pit. Observations were made and representative lithological samples were collected. The samples were collected following the strike of the orebody and mainly focused on the disseminated and massive ore and both mineralized and non-mineralised host rock samples. These include the base metal sulfides samples and the host metasedimentary rocks samples. The samples of the surrounding country rocks were also collected in order to observe any variations in the ore vicinity. The samples were mainly focused on the least altered representative units. Several photos were taken to evidence the representative field relationship of the

samples. A few drill core samples were collected from assay boreholes as an alternative for the inaccessible deeper parts of the deposit. The drill cores were logged prior to sample collection. Approximately 40 representative grab samples were collected from four mining zones of an operating open pit mine (Fig.8)

Figure 8: A photo showing a section of the mining pit. The mining follows the Bushman Lineament indicated by the black graphitic schists where the veins and breccias occur.

4.2.2 Thin and polished thin sections

30 representative thin sections were prepared from the collected samples for the petrography of both the major, minor and accessory phases and the textural relationships of the ores and rocks. Thin sections were prepared at the Department of Earth Resource Science at Akita University, following the procedure outlined below. The rock samples were first cut using a primary diamond blade floor

saw into some rock slabs (~ 2cm by 2cm). The representative rock slabs were then ground using #150, #320, #800 and #1000 mesh size powders on rotating grinders to produce a smooth surface on the sample prior to being heated overnight in an oven hotplate set at 90 degrees Celsius to remove the moisture.

Petropoxy 154 mixed at the ratio of 1:10 or E-bond was used for mounting the samples on the glass slides. Samples bonded by petropoxy 154 were left to dry overnight in a hotplate at 90 degrees Celsius. For E-bond, clips were used to hold the slides in place as well as removing some air bubbles trapped in during mounting. The mounted samples were let to dry overnight to solidify the bonding glue. The mounted samples were cut using a secondary cutter to about 1mm thick. Prepalap machine which is equivalent to #600 mesh powder was then used to grind down the thick sections to about 30 microns. #1000, #2000 and #3000 mesh powders and corresponding polish glasses were used to grind down the thick sections with a 10 minutes ultrasonic bath after the use of each mesh powder. The ultrasonic bath helps to remove the impurities and any unstable particles within the sample. The thin sections were then diamond polished using 3 μm and 1 μm for about 15 minutes each to make polished thin sections. An ultrasonic bath was used after each polishing stage. The thin sections were observed using both reflected and transmitted light with one polar and crossed polars simultaneously under a Nikon Eclipse LV100N petrographic microscope.

4.2.3 Polished sections

Rock chips of the representative sulfide samples were polished on the rotating grinders using corresponding grit powders to produce a smooth surface before being

put in cylindrical sample holders with removable caps. Vaseline gel was applied to the inner part of the holders and base caps prior to putting the sample. Low viscosity mould, 1-2 ml of Struers TM “M curing agent” for every 100 ml of low viscosity fluid was prepared. Samples were placed in the vacuum glass machine to remove the trapped air bubbles in the mould. The samples were left to dry over a period of 24 hours and subsequently hand ground using #150, #320, #800, #1000, #2000 and #3000 mesh powders with corresponding glass plates. Thereafter the edges of the samples were trimmed and smoothened using sandpaper prior to finally polishing those using 3μm and 1μm diamond polishers. An ultrasonic bath was used after every polishing stage. The polished sections were examined using reflected light on a Nikon Eclipse LV100N petrographic microscope.

4.3 Results

4.3.1 Field observations

4.3.1.1 Metasedimentary rocks

Based on drill core and outcrop examinations, the Mowana Cu deposit is hosted by four lithologic units including metamorphosed limestone, argillite, graphitic schists and surrounding granitic gneisses of the Matsitama-Motloutse Complex (Fig. 9). These units are overlain by the ca. 0.2 Ga Phanerozoic Karoo Supergroup sequence of conglomerates and siltstones (Barton et al., 1994). The Mowana orebody plunges 10°to the north (Davis, 2009) hence the base of the Karoo Supergroup also gets deeper (~100 m) to the northern extension of the deposit (Nsamba, personal communication, 2018).

At the deposit scale, the hanging wall granitic gneiss exposed at the eastern portion of the pit dips to the east. The granite gneiss exhibits a strong tectonic fabric which is folded at the footwall contact (Fig. 10a). The western margin of the granite is commonly in contact with the limestone that is located to the east of the argillitic rocks at the deposit scale. However, because of intense folding, in some instances the argillitic rocks are situated adjacent to the granite in the east. The metasedimentary rocks and the enclosing granitic gneisses have been tectonically modified such that they are flattened, elongated, and aligned parallel to the NNE-SSW steeply dipping east at approximately 70-80° Bushman Lineament.

The sampled granite gneisses close to the mineralized zone are greenish grey to pink. The granite commonly suffered from hematite alteration that is associated with Cu mineralization in the adjacent sedimentary rocks (Fig. 10e). The argillites appear green-grey to brown in colour, fine-grained, compact and often silicified. The rocks are highly fractured and/or brecciated in some parts with quartz-calcite stockworks containing pyrite and chalcopyrite disseminations often with hematite alteration (Fig. 10b). The limestone is grey, massive, fine-grained and compact. The rock type is dominantly silicified with observable quartz and calcite veinlets, cross-cutting veins are common (Fig. 10c). Near the mineralized zone, the limestone is highly fractured and jointed. Graphitic schists occur as lenses which are irregularly distributed commonly at the contact between the limestone and argillite (Fig. 11). The graphitic schists are homogeneous grey to black in colour. They typically display ductile deformation in the form of microfolds and shear fabrics. The graphitic schists are in many places cut by small quartz-calcite veinlets, which are rimmed by hematite (Fig. 10d). Pyrite mineralization in the form of stringers is observed along the foliation and the presence of native Cu in the quartz-calcite veinlets was observed in several places. The

occurrence of chloritic schist is subordinate. The chloritic schists are characteristically green, highly friable, fine-grained and associated with hematite and limonite alteration. Minor barren quartz-calcite veinlets have been observed in the chloritic schists.

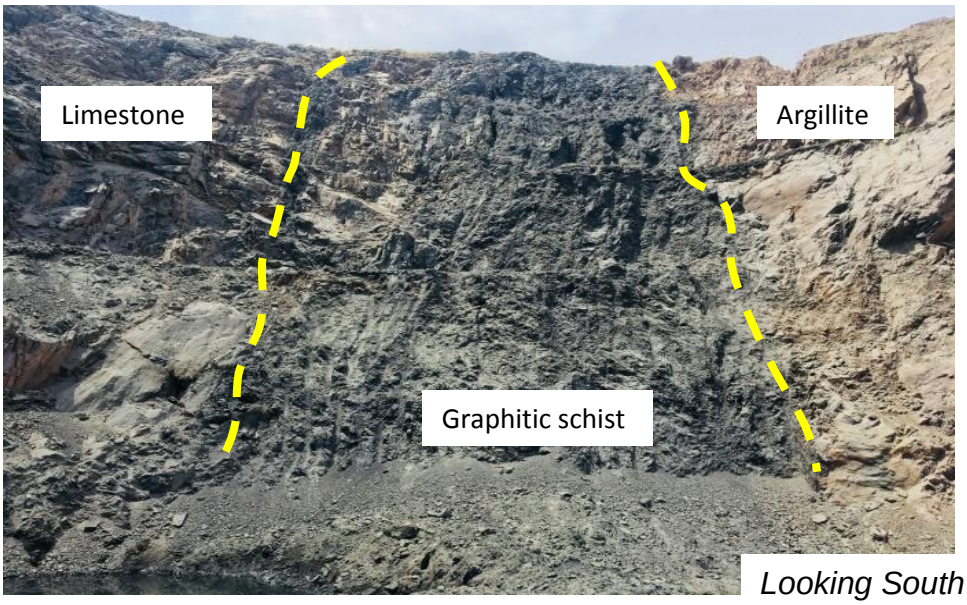

Figure 9: Working face view of the mining pit. The veins occur with the graphitic schists sandwiched between the argillite and the limestone sedimentary rocks (locality: SP1 in Fig.7). Left to right with of field of view is ~7m.

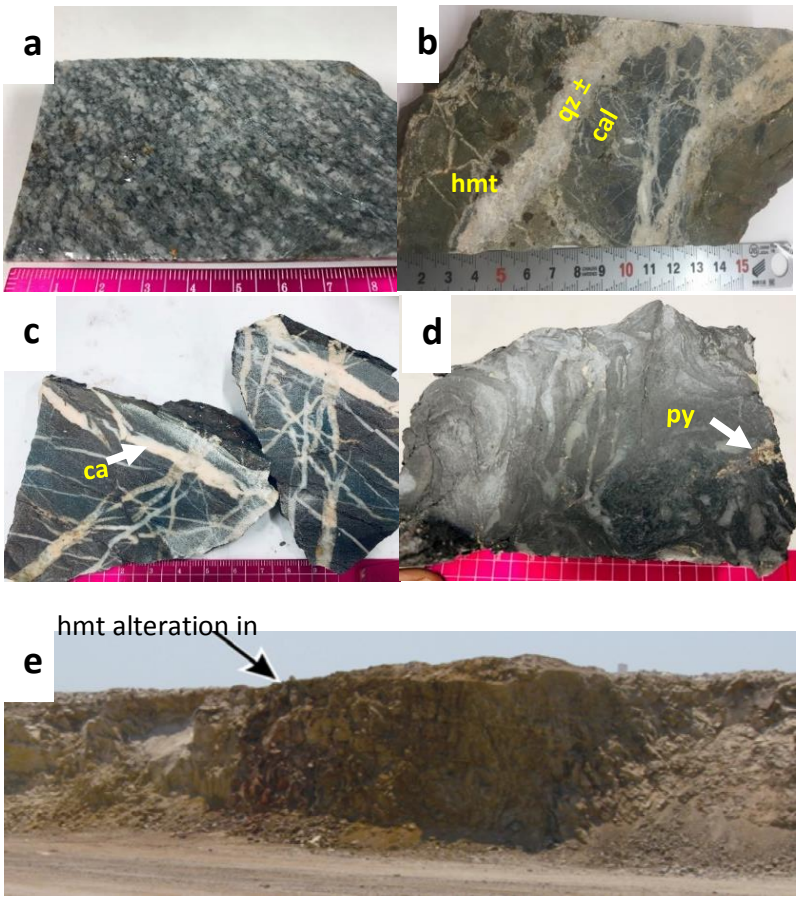

Figure 10: Representative host rock samples from the Mowana deposit. (a) Strongly foliated granitic gneiss (SRK10 152.9 m, G3) (b) Brecciated argillite crosscut by random quartz-calcite veins (BINF16 59m, F1). (c) Limestone with a stockwork of calcite veins and veinlets (sample: SP8). (d) Graphitic schist with a sheared fabric and minor quartz-calcite veinlets containing pyrite (sample: SNP2). (e) Hematite alteration in granite (sample SP20). Mineral abbreviations: cal-calcite; hmt-hematite; py-pyrite; qz- quartz.

Figure 11: Exposures of graphitic schist interlayered with the limestone and argillite rocks (locality: NRE7 in Fig. 4).

4.3.1.2 Mineralization

In the ore zone, there are two types of veins hosting the mineralization. However, time relationships between these veins has not been confirmed hence they were indicated as Type 1 and Type 2 (Fig. 12). The mineralization occurred in brittle deformation structures such as cracks. These structures post-date the main ductile (high temperature) deformation responsible for the formation of the greenstone belt.

The Type 1 veins are characterized by the quartz+calcite ± K-feldspar mineral assemblage. The Type 1 veins host dominantly the Cu mineralization. Type 1 veins occur within the graphitic schist which is commonly sandwiched between the limestone and the argillite and are only present in the Mapanipani north and Mapanipani zones of the deposit (Figure 7). The quartz-calcite ± K-feldspar veins are white to pinkish and

medium- to coarse- grained (Fig. 13a-c). The veins are mineralized with observable primary minerals including chalcopyrite and pyrite. These sulfides occur as disseminations, blebs, and semi-massive within the mineralized veins. In some places, bornite is macroscopically observed to be replacing chalcopyrite. The mineralized vein breccia commonly contains the fragments of the host rocks. Quartz textures, such as zoned and comb quartz is observable on some freshly cut quartz veins hand specimen (Fig. 13c).

The Type 2 veins are characterized by the quartz+calcite ± fluorite gangue mineral assemblage (Figure 13d-e). These veins host the galena mineralization and they only occur in the southern part of the deposit (Bushman zone, Figure 7) separate from the main chalcopyrite-bearing veins. The sulfides occur as blebs in the veins.

Supergene minerals, such as chalcocite and Cu carbonates, have also been observed. Hematite alteration is predominant as fracture infills

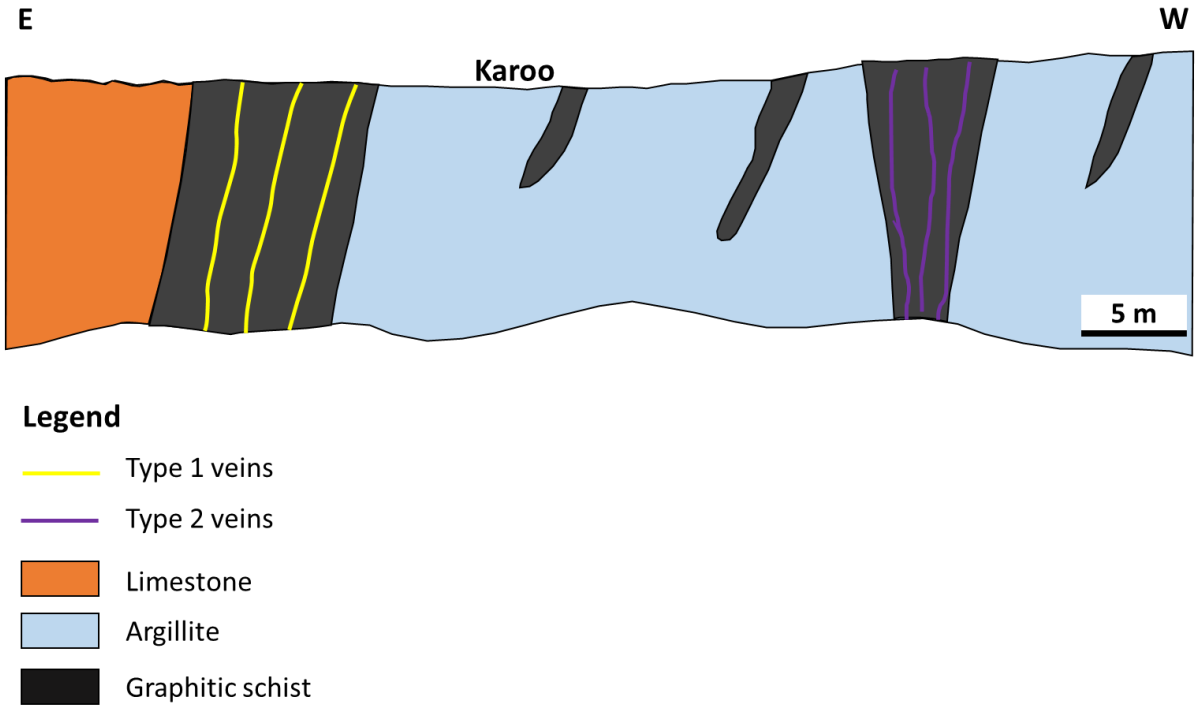

Figure 12: Schematic representation of the hydrothermal veins' occurrence at the Mowana deposit.

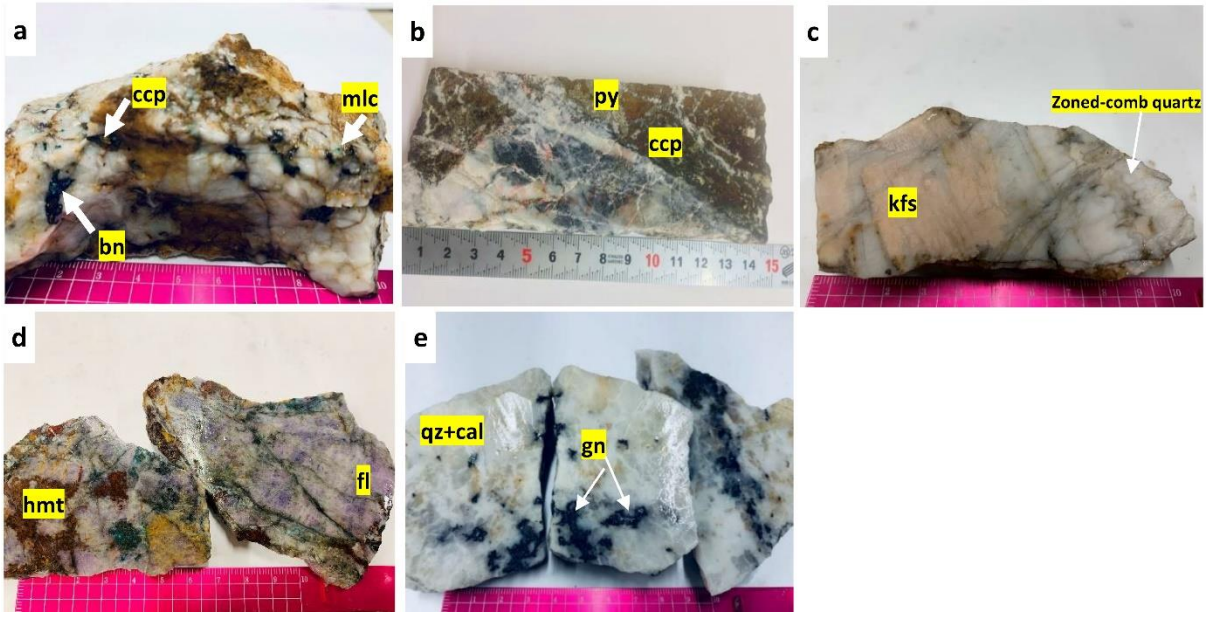

Figure 13: Representative samples (a-c) of the Type 1 vein breccias; (a) Quartz-calcite ± K-feldspar vein sample with primary chalcopyrite and supergene mineralization (sample: SNP4). (b) semi-massive chalcopyrite intergrown with pyrite (AINF6 104 m, C5). (c) Quartz+calcite±K-feldspar vein hand specimen showing the zoned-comb quartz texture. (d-e) Representative samples of the Type 2 vein breccias; (d) Quartz+calcite±fluorite veins hosting the Pb mineralization. Secondary Cu-minerals (malachite) and hematite are observed in the hand sample (Sample: Sp9). (e) Galena in the quartz+calcite±fluorite veins (sample: SP6).

Mineral abbreviations: bn-bornite; cal-calcite; ccp-chalcopyrite; fl-fluorite; gn-galena; hmt-hematite; mlc-malachite; qz-quartz.

4.3.2 Petrography

Based on microscopic observations the granite is essentially composed of quartz, K-feldspar, plagioclase, and biotite. Muscovite is present in trace amount. In the granite gneiss, the K-feldspar and plagioclase are altered to epidote and minor sericite, and biotite is altered to chlorite (Fig. 14a-c). Late non-mineralized calcite veinlets crosscut the pre-existing minerals. Argillite is characterized by strong silicification where quartz is the main cement (Fig. 14d-f). Limestone is predominantly silicified and dolomitized in some parts especially in the southern part of the deposit (Fig. 15a-c). The graphitic schist is characterized by abundant graphite and muscovite. The graphite occurs as >2mm laths largely oriented along the foliation of the schist. The schistosity is defined by the preferred orientation of muscovite. The graphitic schist (Fig. 15d-f) is in places cut by minor quartz and calcite veinlets with sulfides

mainly pyrite stringers and disseminations both in the veinlets and in the host rock. Pyrite found in the graphitic schist is enclosed by galena. In some instances, pre-existing quartz and calcite crystals are rimmed by hematite.

The granite gneiss mostly suffered from chloritization, epidotization, sericitization, and hematite alterations. The argillite and limestone predominantly suffered from pervasive silicification, carbonate alteration, and minor hematite alteration.

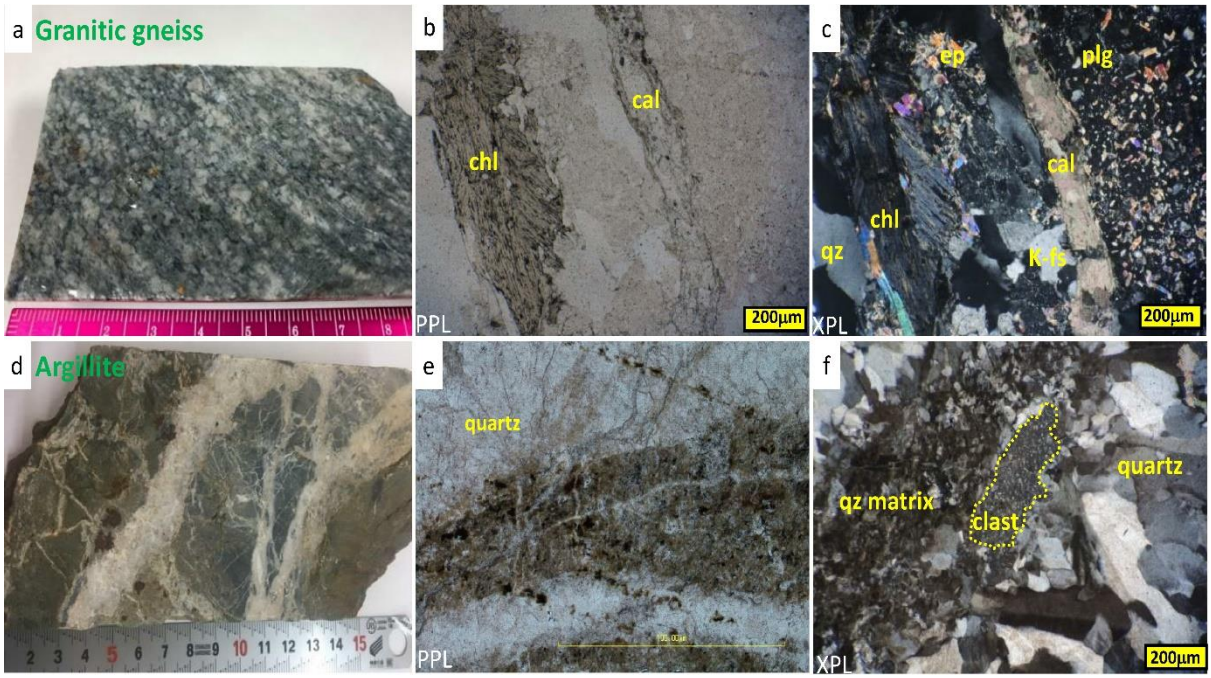

Figure 14: Representative photomicrographs of the host rock samples from the Mowana deposit. (a-c) quartz-carbonate vein associated with chloritization and epidotization of granite (SRK10 152.93 m, G3). (d-f) Intense silicification in argillite (BINF16 59 m, F1). Mineral abbreviations: cal-calcite; chl-chlorite; ep-epidote; K-fs-K-feldspar; plg-plagioclase; qz-quartz.

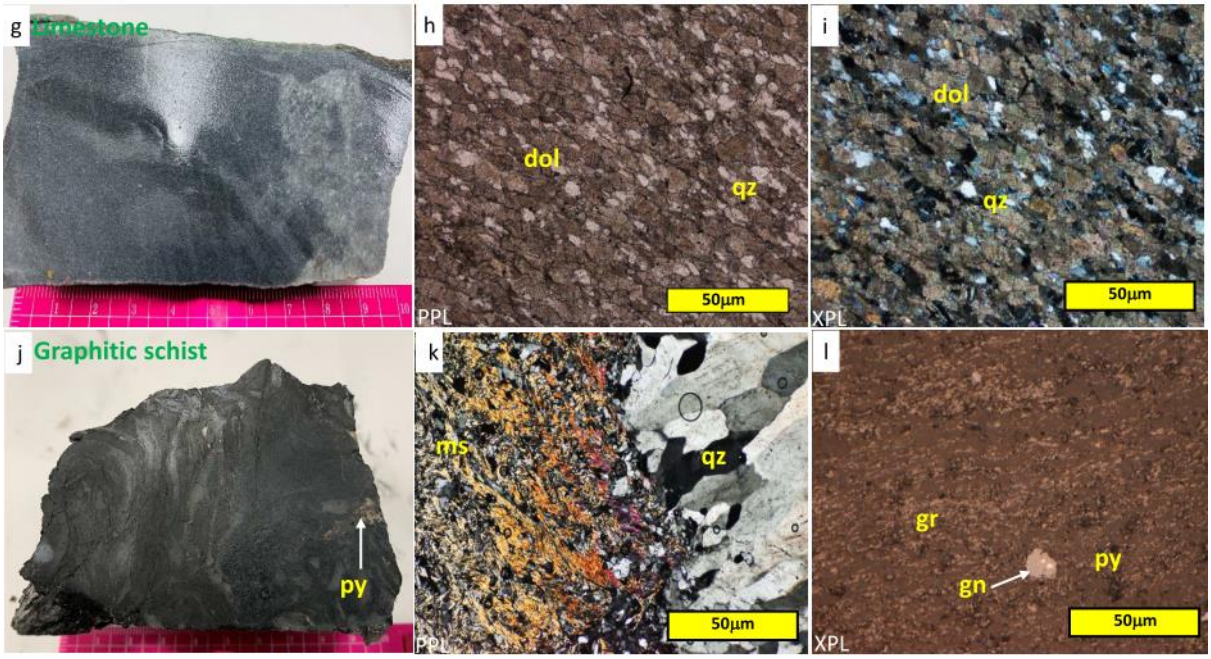

Figure 15: Representative photomicrographs of the host rock samples from the Mowana deposit. (a-c) Silicified and dolomitized limestone (sample: NP3). (d-f) hematite alteration enclosing the earlier carbonate and quartz (sample: NP5). Mineral abbreviations: cal-calcite; dol-dolomite; gn-galena; gr-graphite; hmt-hematite; py-pyrite; qz-quartz.

4.3.3 Textures of quartz and calcite veins

The Type 1 mineralized and non-mineralized vein breccias and veins consist predominantly of quartz+calcite±K-feldspar and are typically coarse-grained. The vein breccias are locally accompanied by the graphite. The quartz crystals from the Type 1 quartz veins exhibit several textures including comb, massive, mosaic, and zoned textures (Dong et al., 1995). The mosaic texture comprises aggregates of irregular and interpenetrating quartz crystals (Fig. 16d). In some instances, the quartz shows different generations wherein the comb quartz is observed around the earlier formed zoned and comb textured quartz (Fig. 16a-b). Comb quartz commonly shows zoned texture (Fig. 16a). Calcite occurs as massive and medium- to coarse-grained irregular crystals. In some instances, calcite seems to postdate the quartz as it encloses some quartz crystals and/or crosscut the earlier formed quartz (Fig. 16e-f). The K-feldspar where present, occurs as subhedral to anhedral crystals alongside the quartz and calcite (Fig. 16g-h).

The Type 2 quartz+calcite±fluorite veins are constituted of the same mineral assemblage with the addition of fluorite coexisting with quartz and calcite. Quartz in Type 2 veins also displays the mosaic, comb, massive, and zoned quartz textures. Pre-formed massive quartz is cut by the late generation of comb quartz and aggregates of anhedral quartz infills the spaces (Fig. 17a-b). Zoned and mosaic quartz was also observed (Fig. 17c-d). Feathery quartz has also been observed filling fractures in the earlier formed massive calcite (Fig. 17e-f). Fluorite exists as massive and cubic to massive crystals. Quartz and calcite crystals fill the fractures in fluorite (Fig. 17g-h) Generally, massive quartz formed earlier followed by the comb and/or

zoned comb quartz then mosaic quartz. Calcite can be observed with any of the quartz textures.

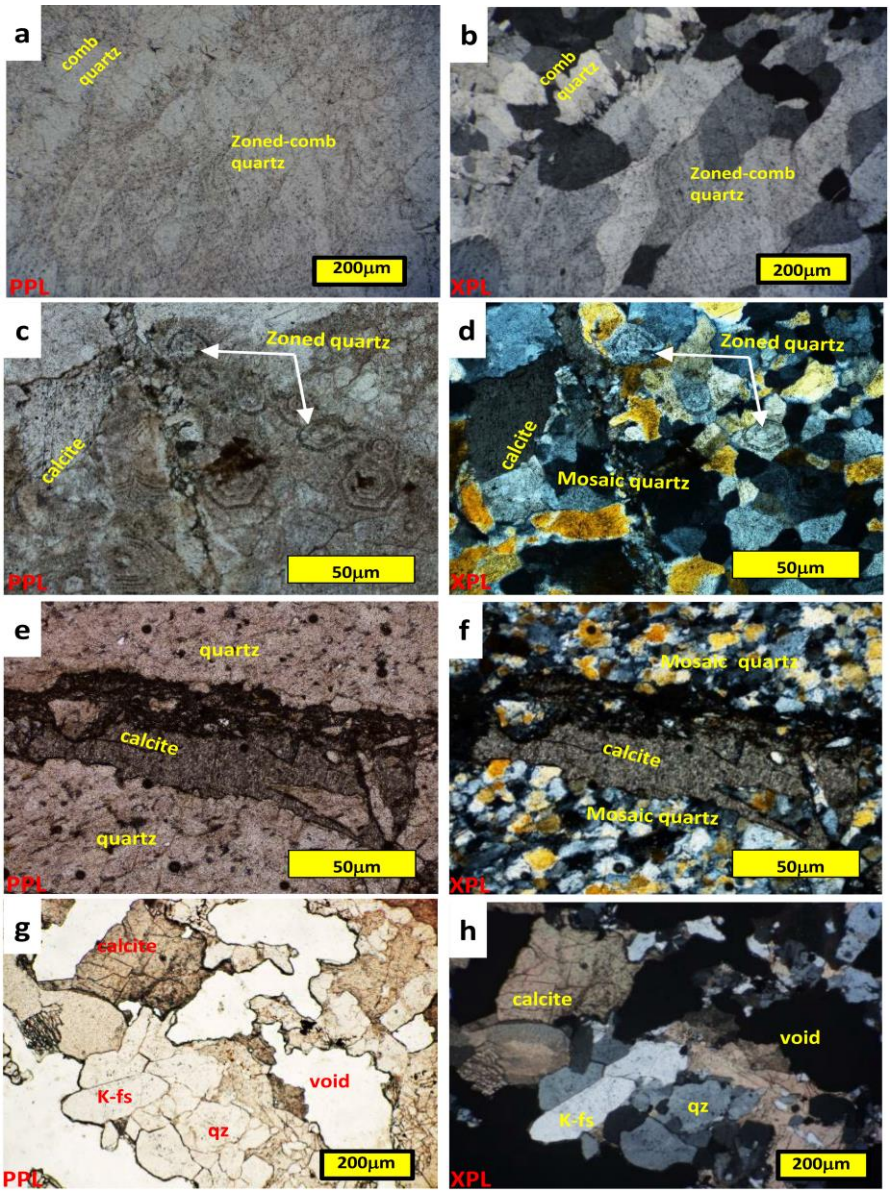

Figure 16: Representative photomicrographs of the quartz textures observed in the quartz+calcite±K-feldspar (Type 1) veins samples from the Mowana deposit. (a) Comb and zoned texture quartz (BINF9, 51.94 m, E1). (b) Mosaic and zoned texture quartz (CINF28, 81.5 m, A3). (c) Mosaic texture quartz cut by platy calcite (Sample: NP6). (d) Quartz+calcite±K-feldspar veins mineral assemblage (BINF16, 61.5 m, F2). Mineral abbreviations: cal-calcite; K-fs-K-feldspar; py-pyrite; qz-quartz.

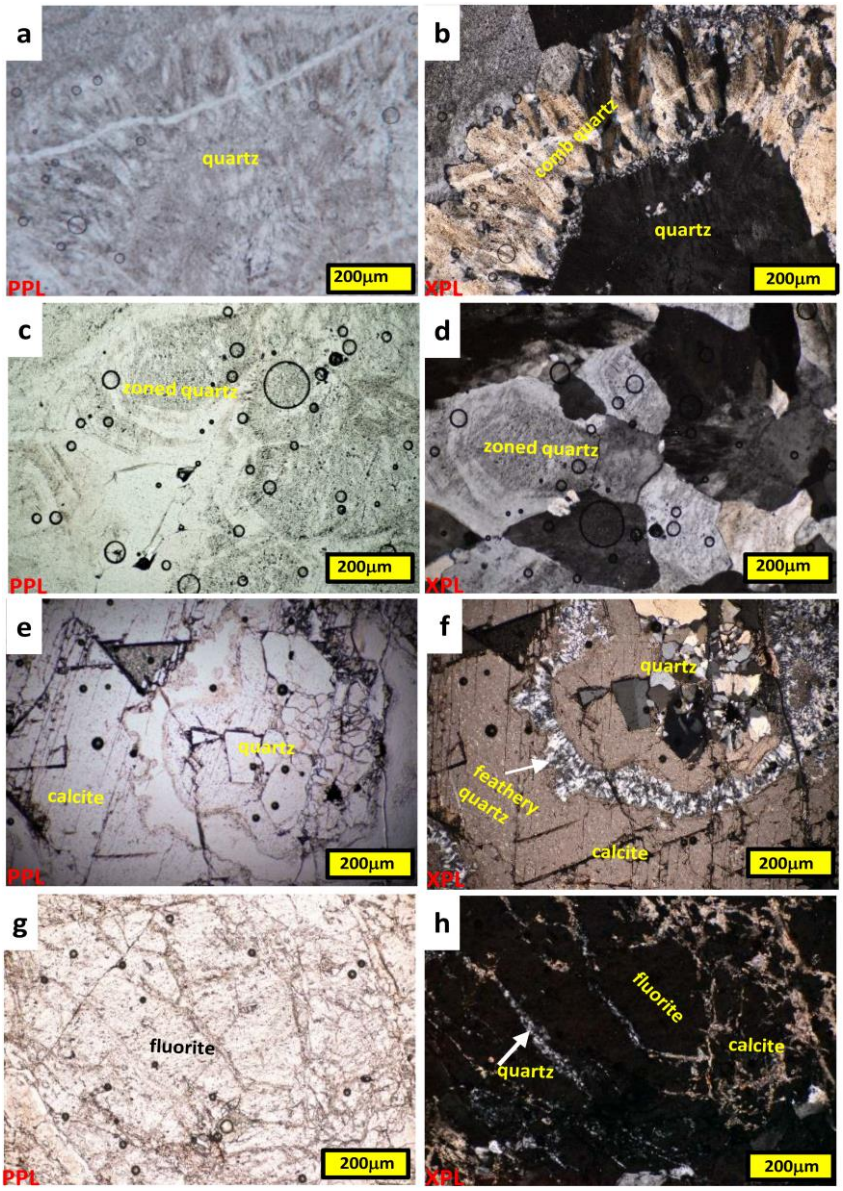

Figure 17: Representative photomicrographs of the quartz and calcite textures observed in the quartz+calcite±fluorite (Type 2) veins from the Mowana deposit. (a) Coarse grained quartz crystal overgrown by late generation comb quartz and the anhedral quartz aggregates infilling the interstitial spaces (Sample: SP7). (b) Coarse-grained quartz crystal showing zoned texture (Sample: SP10). (c-d) Quartz showing mosaic and feathery quartz along with massive calcite (Sample SP4). (e-f) Fluorite occur as coarse-grained crystals with quartz and calcite filling the interstitial spaces (SP5).

4.3.4 Ore mineralogy

Detailed macroscopic and microscopic observations revealed that the mineralization at Mowana is hosted in two types of veins. The first type is characterized by the Cu association in mining zones A, B, C, and D whereas the whereas the second type is connected to the Pb association in mining zone D (Figure 4). The superficial levels suffered from supergene enrichment and oxidation of the ore minerals.

4.3.4.1 Type 1 mineralization

The Type 1 mineralization consist of predominantly chalcopyrite, and minor galena. The ore occur along fractures or cracks, and cementing breccias as well as blebs in the mineralized veins. Quartz + calcite and minor K-feldspar are the main gangue minerals occurring together with the ore minerals. The Cu-ore occurs as blebs and/or semi-massive in the veins. Chalcopyrite occurs as coarse-grained, irregular, and porous grains in some instances rimmed by chalcocite (Fig. 18a-b) and in some parts intergrown with primary bornite (Fig.18c). Chalcopyrite is in contact with pyrite which is in some cases present as inclusions in chalcopyrite. Pyrite occurs as subhedral to anhedral aggregates, and euhedral and zoned discrete grains (Fig. 18e). Galena occurs as subhedral to anhedral isolated grains or as veinlets (Fig. 18c).

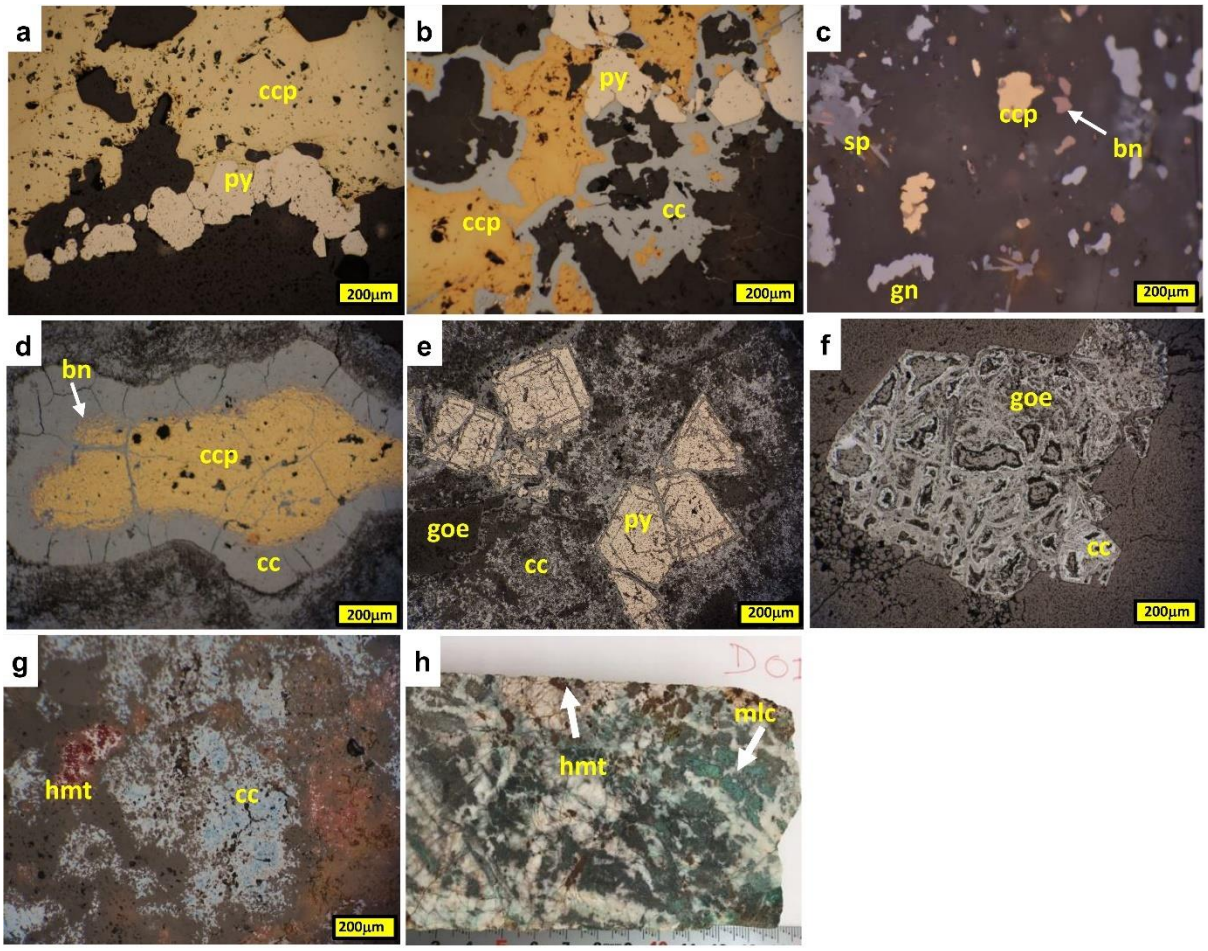

Figure 18: Representative photomicrographs and hand specimen of the characteristic hypogene and supergene stages at Mowana deposit. (a-b) Chalcopyrite (ccp) from type 1 veins, with pyrite (py) and chalcocite (cc) (AINF6 104 m, C5). (c) Chalcopyrite and bornite (bn) with minor galena (gn) (Sample: NP1). (d) Chalcocite with minor bornite both replacing chalcopyrite (BINF9 145.7 m, E5), (e) Zoned pyrite with fractures infilled by chalcocite which is in turn replaced by goethite (goe) and hematite (BINF9 133.0 m, E4). (f) Chalcocite strongly degraded and replaced by hematite (hmt) (BINF9 133.0 m, E4). (g) Macroscopic image showing malachite (mlc) and hematite from the oxidised upper part of the deposit (AINF26 24.7 m, D1). (g-h) Galena from the Type 2 veins. Covellite (cv) and anglesite (ang) replace galena (sample: SP6).

4.3.4.2 Type 2 mineralization

The second type of mineralization presented as Type 2 veins is characterized by the dominant precipitation of Pb sulfides: galena, alongside quartz, calcite, and minor fluorite. The sulfides are hosted by the quartz+calcite±fluorite veins in the southern sector of the deposit. The ore occurs as anhedral blebs in the veins and/or as veinlets (Fig. 19a). Chalcopyrite, and pyrite were observed in trace amounts in the samples representing type 2 veins.

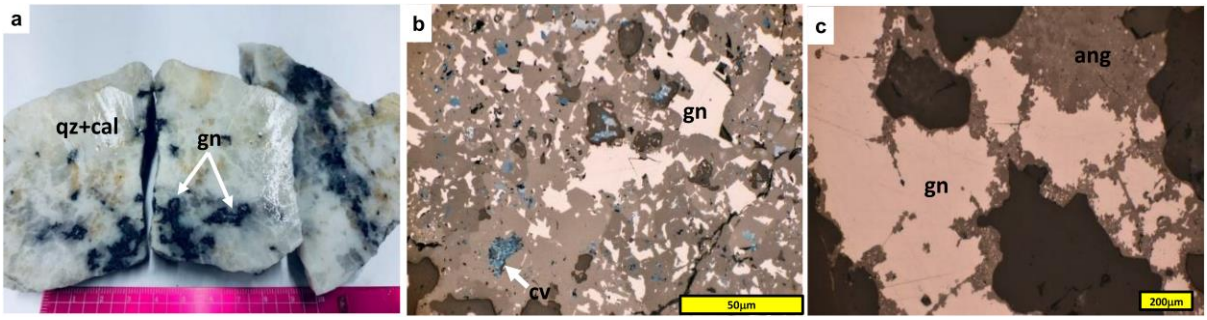

Figure 19: Representative samples from the Type 2 veins. (a) Hand specimen of the quartz+calcite vein from Type 2 veins. (b) Galena and from type 2 veins. (b-c) Covellite (cv) and anglesite (ang) replace galena (Sample: SP6).

4.3.4.3 Supergene alteration

The surface and shallower parts (up to 70 m below the surface) of the deposit experienced supergene enrichment and oxidation of the primary ore minerals. The supergene minerals occur disseminated in the supergene affected samples. In the Type 1 veins, the supergene enrichment stage is mainly manifested by massive chalcocite dominance. The chalcocite mainly occurs replacing chalcopyrite. Secondary bornite was also observed to replace some chalcopyrite crystals at the peripheries (Fig. 18d). Some earlier-formed pyrite crystals are zoned and/or fractured

with their interstices filled by chalcocite, which is in turn partially or entirely replaced by goethite and/or hematite (Fig. 18e). Complete replacement of pyrite by chalcocite and goethite consecutively leaves behind a pseudo-concentric texture in some parts (Fig. 18f). The oxide alteration is characterized by Fe-oxides and Cu-carbonates. Chalcocite is in some instances corroded and altered to hematite (Fig. 18g). The oxide mineral assemblage comprises malachite, hematite, and goethite (Fig. 12h). The paragenetic sequence showing mineral assemblages of the type 1 veins is shown in Figure 20.

Covellite and anglesite were observed as the supergene minerals replacing galena in the Type 2 veins (Fig. 19b-c). Moreover, minor chalcocite was observed replacing both galena. The paragenetic sequence showing mineral assemblages of the Type 2 is shown in Figure 21.

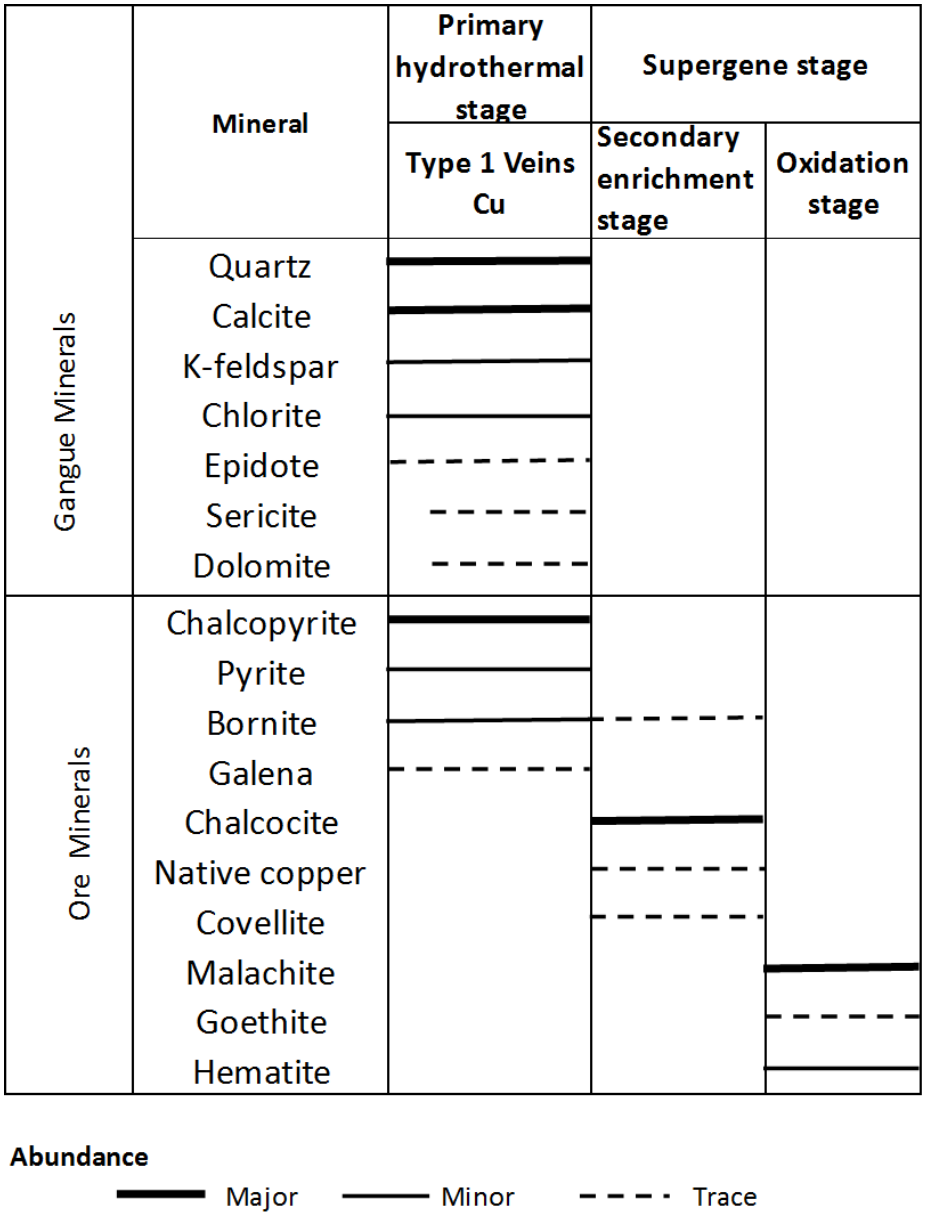

Figure 20: Paragenetic sequence of the Type 1 veins mineralization *at the* Mowana deposit showing the relative abundance of the minerals. The early mineralization stage is dominated by the precipitation of chalcopyrite and minor pyrite. The secondary enrichment stage is dominated by chalcocite and bornite while the oxidized ore mineral assemblage is predominated by malachite.

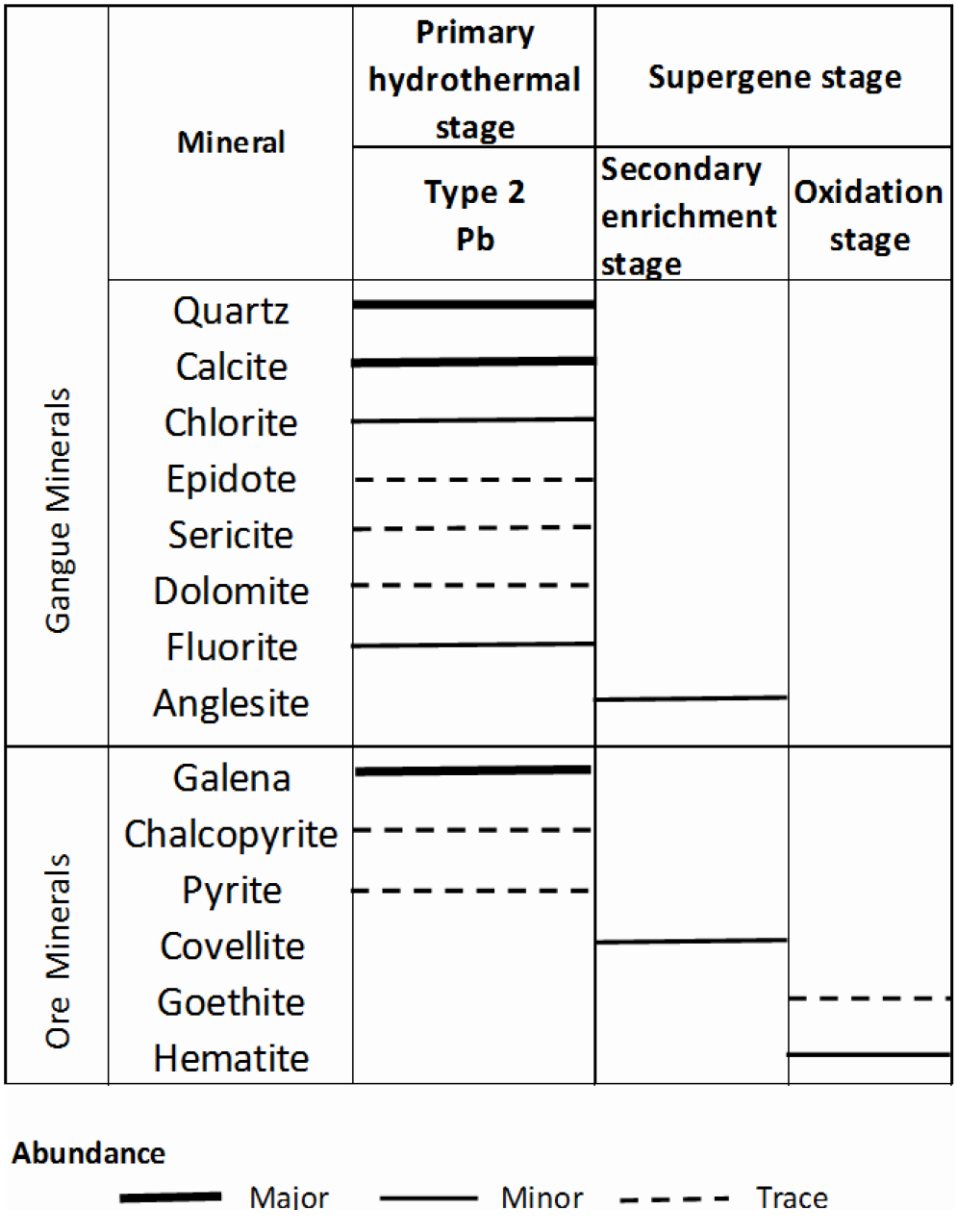

Figure 21: Paragenetic sequence of the Type 2 veins mineralization in Mowana deposit showing the relative abundance of the minerals. The early mineralization phase is characterized by galena and traces of chalcopyrite and pyrite. The supergene stage is dominated by covellite and minor hematite.

4.4 Discussion and Conclusions

The hydrothermal alteration mineral assemblages at the Mowana deposit are dominated by quartz, chlorite, epidote, sericite, hematite, and carbonate. The

hydrothermal alteration is closely associated with the mineralization since the alteration minerals occur along the veins together with the sulfides. Based on the thermal stability of the hydrothermal minerals in hydrothermal systems (Henley and Ellis, 1983; Reyes, 1990; Fig. 22), this alteration mineral assemblage is produced by near-neutral pH fluids. The temperature of alteration estimated from the alteration mineral assemblage ranges between 200 °C and >340 °C. Barton et al., 1994 estimated the mineralizing fluids temperature at 360 ± 8°C based on sulfur isotope geothermometry on three co-existing mineral pairs: (i) pyrite-sphalerite, (ii) pyrite-galena and (iii) sphalerite-galena. The temperature inferred from alteration mineral assemblage, sulfur isotope thermometry and chlorite geothermometry (next chapter) are consistent.

Quartz textures have been classified into three groups reflecting their genesis and environment of formation, namely: primary growth, recrystallization, and replacement textures adopting the classification of Dong et al. (1995). The primary growth textures are interpreted as textures formed during the initial open space-filling (Dong et al., 1995). In this study, the primary growth textures are manifested by the comb and zoned quartz. Feathery and mosaic types are described as recrystallization textures (Dong et al., 1995).

The comb texture is a primary growth texture based on geometrical selection wherein only the crystals in the direction of maximum growth are oriented perpendicular to the growth surface (Dong et al., 1995). Comb quartz is formed from slightly silica-supersaturated fluid in open space with slow cooling and uniform crystal growth (Dong et al., 1995). Zoned texture records a change of conditions during crystal growth (Fournier, 1985). Coarse-grained idiomorphic quartz crystals depict the quartz that

formed under slow cooling conditions in an open space (Moncada et al., 2012). The solubility of calcite and quartz are temperature dependant. The solubility of calcite increases with a decrease in temperature, while the solubility of quartz decreases with an increase in temperature (Seward et al., 2014). Therefore, subsequent slow fluid cooling coupled with pressure decrease resulted in calcite-undersaturated and silica super-saturated fluid conditions. Further increase in silica super-saturation resulted in the precipitation of quartz. The quartz textures may provide an aid in terms of the physical conditions associated with mineralization (Moncada et al., 2012). Although the obtained data is not enough, i.e., absence of fluid inclusion data to ascertain the possibilities of boiling or non-boiling conditions (Moncada et al., 2012), associated with the identified quartz textures, the mineralization at the Mowana deposit may have possibly formed under non-boiling conditions as evidenced by the dominant quartz textures (comb, zoned, and mosaic) observed.

Based on the observed ore mineral assemblage observed to be in equilibrium, and the temperature obtained from the chlorite geothermometry, the sulfidation state of the Mowana deposit has been estimated. The ore mineral assemblage from the Type 1 veins, lies on the boundary line of the co-existence of pyrite, bornite and chalcopyrite at a temperature range of 300-400 °C corresponding to high sulfidation state.

Moreover, the following interpretations could be made about the mineralization of the Mowana deposit;

1. The abundance of the quartz and calcite can be linked to the passage of silica saturated and calcite saturated fluids, respectively.

2. Reaction rims observable at the contact of the Type 2 veins and the host rocks or pre-formed minerals can be attributed to temperature difference.
3. The presence of pyrite with pronounce growth zones may be attributed to changes in the hydrothermal fluid composition.
4. Chalcopyrite has some inclusions of pyrite in some parts which may indicate that the chalcopyrite formed later than pyrite.
5. The pyrite crystals are fractured with interstices filled by chalcocite and goethite and/or haematite which indicates the replacement process.

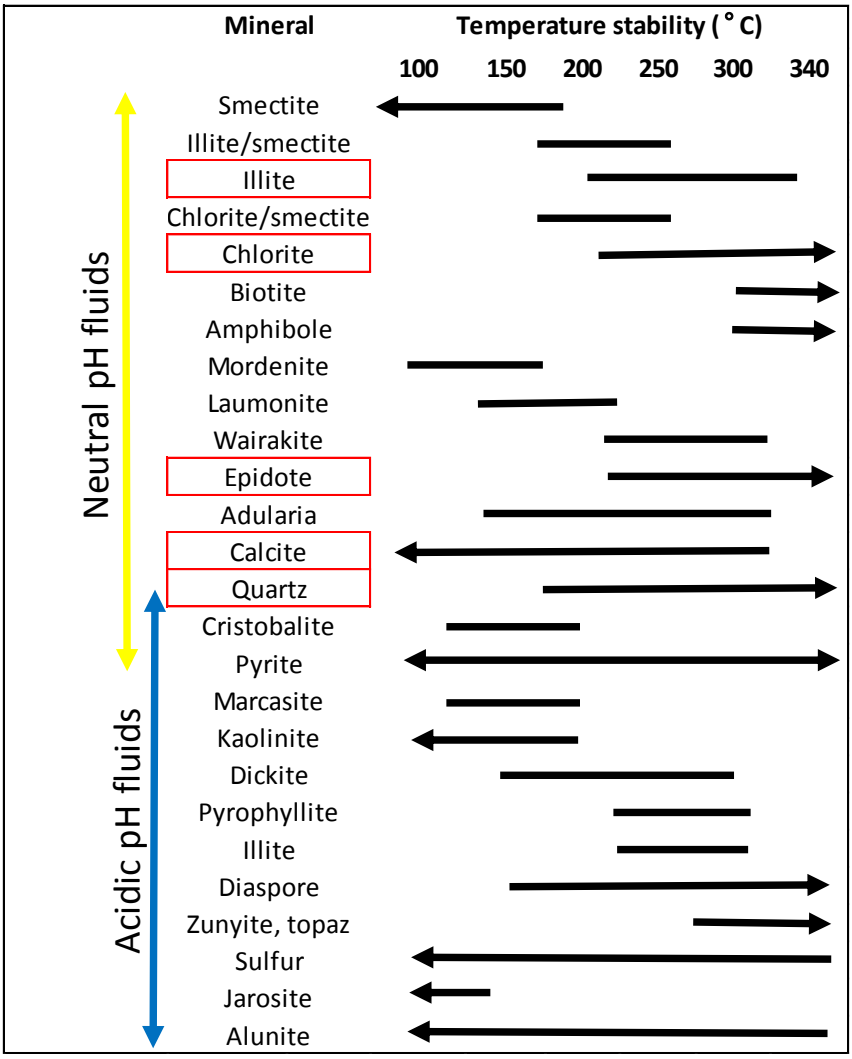

Figure 22: Temperature of stability of hydrothermal minerals. Modified after Henley and Ellis, (1983); Reyes, (1990). The red boxes indicate the alteration minerals observed in this study

CHAPTER 5: ORE MINERAL CHEMISTRY

5.1 Introduction

Trace element compositions of the chalcopyrite, galena and pyrite have been used as a tool to evaluate the co-crystallization of several base metal sulfides (Cook et al., 2016, George et al 2018). Therefore, the investigation on the representative mineralized samples was conducted through EPMA. This chapter aims to unravel the relation between the elemental composition of the minerals and the characteristics of the hydrothermal fluids responsible for the deposit formation. The ore minerals analyzed include: (a) chalcopyrite, which is the principal base metal in the deposit (Type 1), (b) pyrite (Type 1), and (c) galena which is abundant in the quartz+calcite±fluorite veins (Type 2).

5.2 Methodology

Quantitative analyses were conducted on representative ore specimens to determine the chemical composition of the sulfides, using a JOEL JXA-8230 Electron Probe Micro-analyser housed within the Department of Earth Resource Science, Akita University. Multiple points were analyzed in each target mineral in each sample.

Major and minor elements composition in galena were analyzed under the following parameters: 20 Kv, and 2.0 nA probe current. The elements Se, As, Zn, S, Fe, Cu, Pb, Au, Ag, and Sb were analysed. The standard materials used were synthesized compounds (PbS, GaAs, SnSe, ZnS, Fes2) and pure metals (Ag, Sb, Cu, and Sn).

Chalcopyrite elemental composition was analyzed at 20Kv acceleration voltage and 2.0 nA probe current. The elements analyzed were Cu, Fe, S, Ni, Co, Cr, As, Te, Pb, Zn, Au, and Ag. The standard materials used were synthesized compounds (Fes2, GaAs, PbS, ZnS) and pure metals (Cu, Fe, Ni, Co, Cr, Te, Au, Ag)

Representative samples of pyrite were analyzed for the following elements: Fe, S, Cu, As, Co, Ni, Cr, Pb, Zn, Te, Ag, Au. The following parameters were adopted for the analysis: 15 kV acceleration voltage and 20 nA probe current. The standard materials used were synthesized compounds (FeS2, GaAs, PbS, and ZnS) and pure metals (Co, Ni, Cu, Fe, Te, Ag, Au)

Chlorite chemical composition was analysed under the following parameters: 20Kv, and 20 nA probe current. The following elements analyzed were Si, Al, Cr, Fe, Mn, Mg, Zn, Ca, Na and K. Acquisition time for each element was 3 seconds with the background counted for 6 seconds. The standard materials used included SiO_2, TiO_2, MnO, Al_2O_3, MgO, FeO, Na_2O, $KAlSi_3O_8$, Cr_2O_3.

5.3 Results

5.3.1 Pyrite

The Fe and S contents of pyrite from the quartz+carbonate veins range from 45.26 wt.% to 46.5 wt.% with an average of 46 wt.% and from 53 wt.% to 53.9 wt.% with an average of 53.4 wt.%. The average contents of Co and Ni range from 143 ppm to 33.6 ppm respectively. Pyrite contains up to 200 ppm Au. The average contents of As and Ag are 107 ppm and 1.7 ppm respectively. The ratios of S/Fe, Co/Ni, Au/Ag and Fe/(S+Au) are: 1.15 to 1.18, 1.00 to 46.50, 1.00 to 8.00 and 0.85 to 0.87 respectively

with corresponding average values of 1.16, 1.42, 0.17 and 0.86 respectively. The maximum contents of Cu, Pb and Zn in pyrite are 0.1 wt.%, 3.8 wt.% and 0.1 wt. %. The results of the EPMA analysis of pyrite are shown in Appendix III.

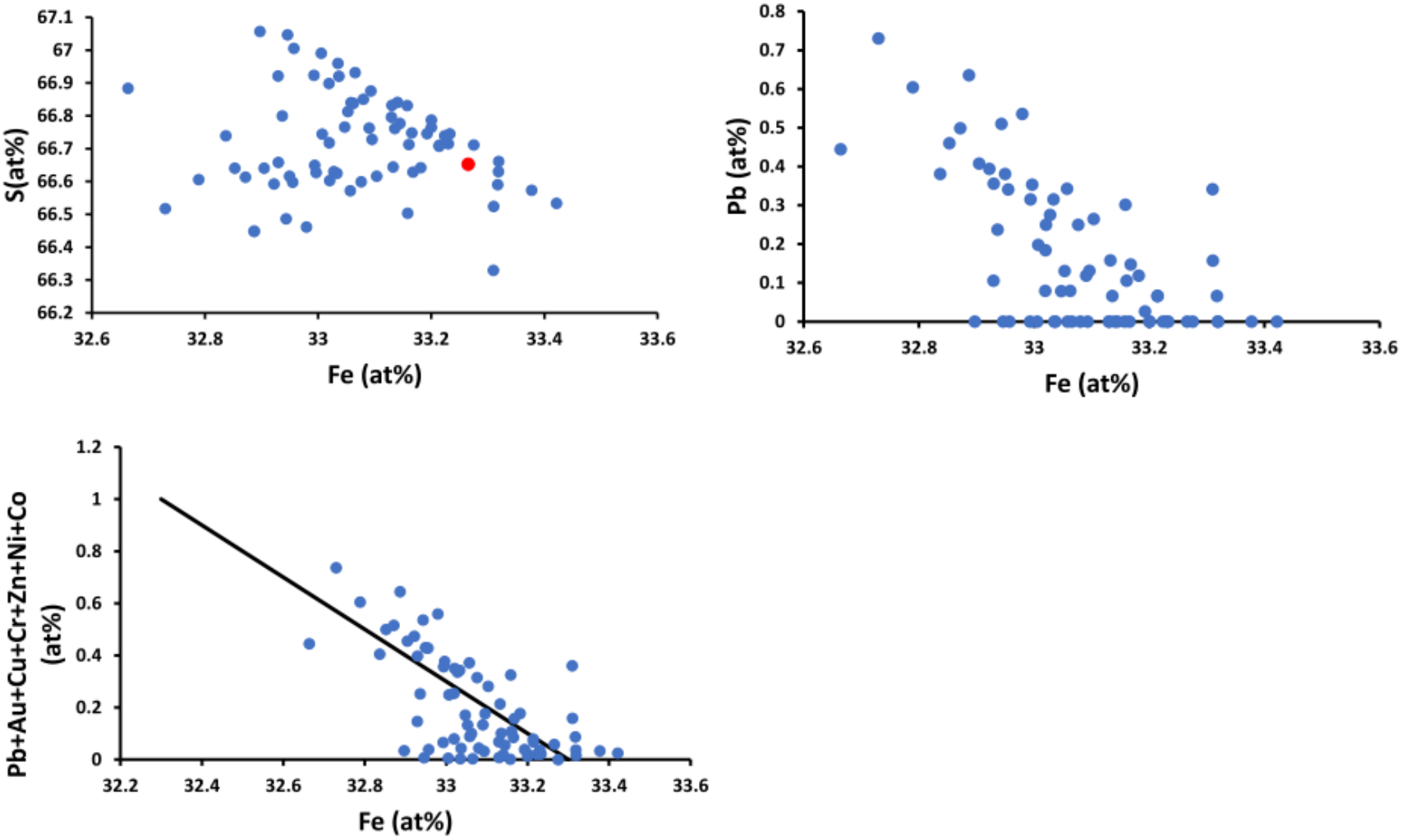

Figure 23: Scatter diagrams for the trace element composition of Type 1 vein pyrite. The red spot indicates the ideal composition for pyrite.

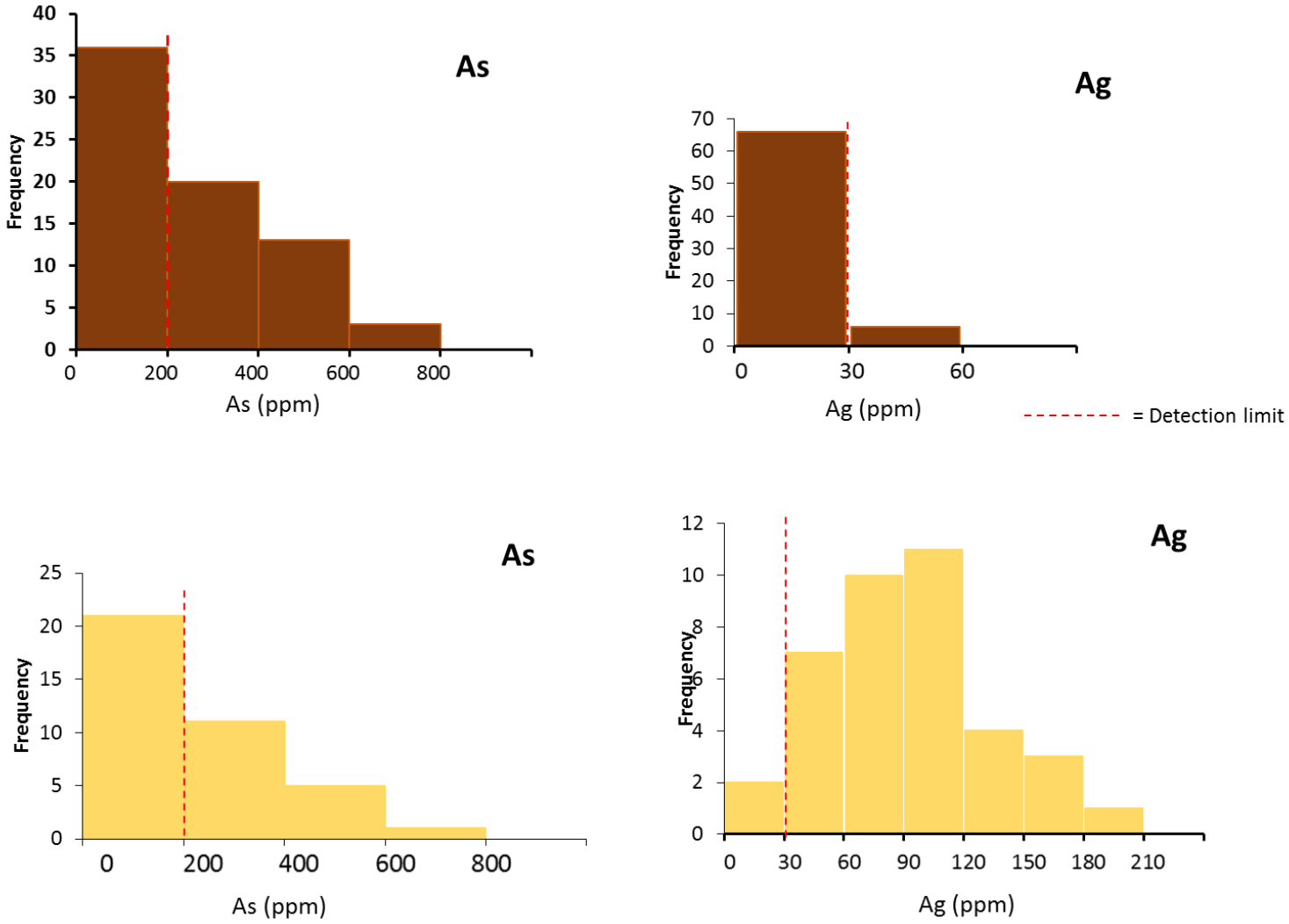

Figure 24: Histograms representing elemental contents of the pyrite (brown) and chalcopyrite (yellow).

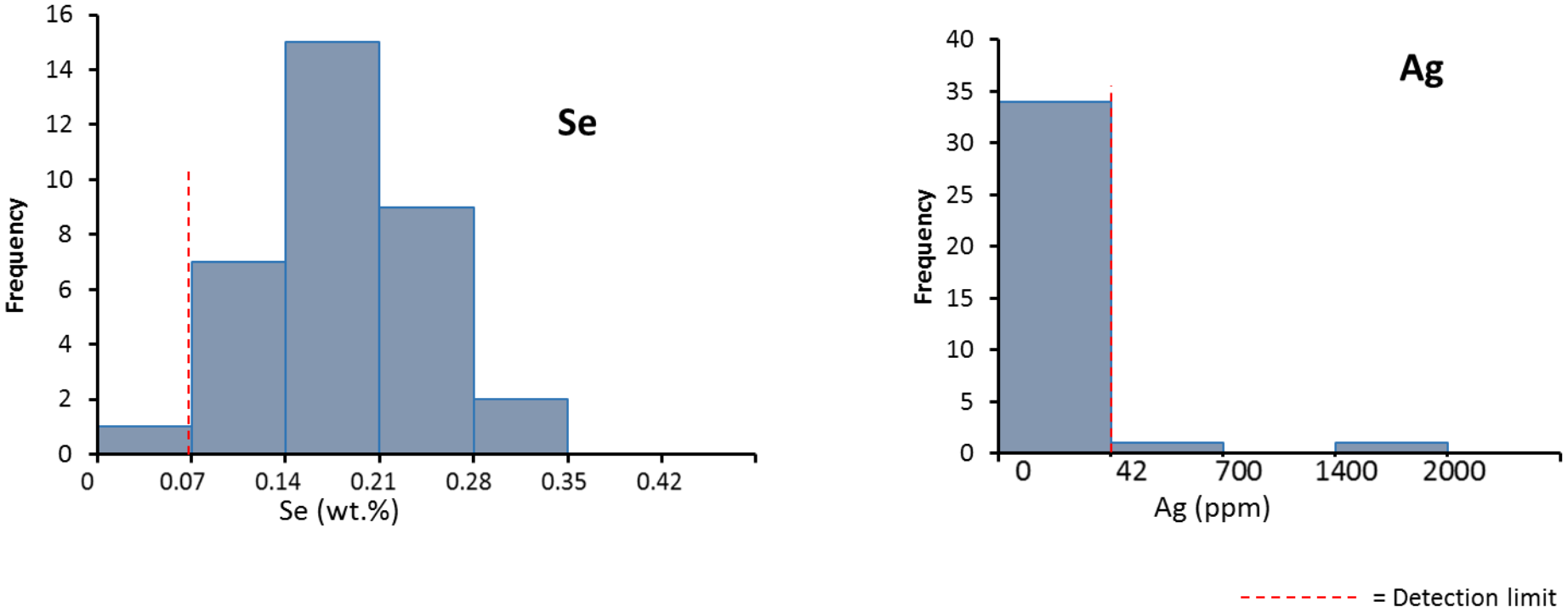

Figure 25: Histograms representing elemental contents of the galena from Type 2 veins.

5.3.2 Galena

The Pb and S contents of galena range from 84.1 wt.% to 87.0 wt.% and 12.7 wt.% to 13.5 wt.% with corresponding average values of 85.7 wt.% and 13.2 wt.% respectively. Galena contains elevated amounts of Se with an average of 1231 ppm. In general, galena shows low contents of Ag, although one sample recorded a peak of 1770 ppm Ag. The Au content in galena is below the detection limit (57 ppm). The highest value recorded for Zn is 180 ppm. The maximum Fe and Cu contents in galena are 0.04 wt.% and 0.64 wt.% respectively. Sb content is below the detection limit (53 ppm). The histograms representing some of the trace element compositions in pyrite are shown in Figure 25. The results for the microprobe analysis of galena are shown in Appendix II.

5.3.3 Chalcopyrite

Electron probing of chalcopyrite indicated that chalcopyrite contains Cu, Fe and S ranging from 33.3 wt.% to 34.2 wt.%, 30.4 wt.% to 31.5 wt.% and 32.3 wt.% to 33.9 wt.% with corresponding average values of 33.8 wt.%, 32.5 wt.% and 35.3 wt.% respectively. The Ag contents in chalcopyrite mostly range between 30 ppm and 180 ppm. The maximum Au content is 120 ppm. Cr content in chalcopyrite is 29 ppm on average. Other trace elements analysed including Co, Zn and Pb are below the detection limit. The trace elements that show significant concentrations are shown in Figure 24. Appendix I, provides the complete results for the microprobe analysis of Chalcopyrite.

5.3.4 Chlorite

Chemical compositions of the chlorite associated with the mineralization in the hydrothermal veins were analysed through electron micro-probe analysis. Chlorite mainly occurs as large irregular crystals enveloping the ore minerals (Fig. 25d). It also occurs as vein infills contemporaneous with the ore minerals (Fig. 25a-b). In some parts chlorite occurs as aggregates associated with haematite (Fig. 25c). The chemical composition of chlorites from samples of the Mowana mine is shown in Table 1. Four samples (SRK10, NRE4, SNP1, and SP11) representing the Type 1 veins were analyzed. The Fe/(Fe+Mg) and Si contents of the chlorite are in the range 0.57-0.62 and 2.6-3.0 a.p.f.u., respectively. These concentrations correspond to the ripidolite chlorite type composition which belongs to the chamosite-chlinochlore series. (Fig. 27; Heys, 1954).

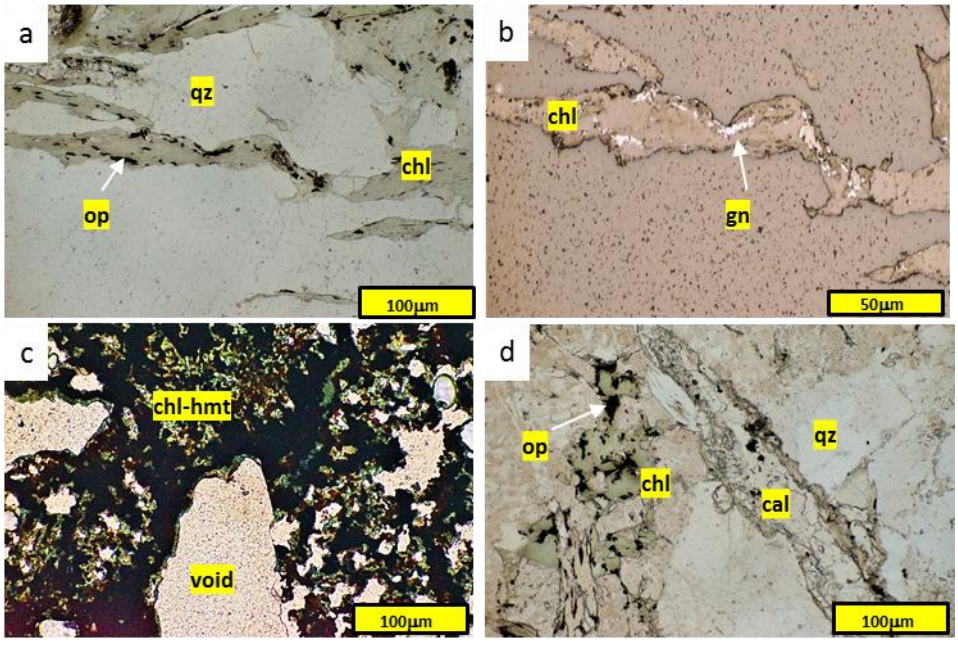

Figure 26: Representative photomicrographs showing the occurrence of chlorite contemporaneous with the hydrothermal alteration in the Type 1 veins of the Mowana deposit. (a-b) Chlorite occuring as vein infills alongside the ore minerals (SRK 10 153.0 m, G3). (c) chlorite-hematite occurring as aggregates (SP11). (d) Chlorite as irregular crystal enveloping the ore minerals(opaque). Abbreviations: cal, calcite; chl, chlorite; gn, galena; op (opaque), qz; quartz.

Table 3: The average chemical compositions of chlorite from the mineralized samples of the Mowana deposit.

Sample ID	**SRK10**		**NRE4**		**SNP1**		**SP11**	
Number of analysis	n=17		n=10		n=11		n=15	
	Ave.	(±σ)	Ave.	(±σ)	Ave.	(±σ)	Ave.	(±σ)
SiO_2(wt.%)	24.92	1.13	24.06	0.09	24.41	0.17	24.96	0.99
TiO_2	0.30	0.77	0.04	0.02	0.07	0.03	0.08	0.04
Al_2O_3	19.44	0.55	19.71	0.22	18.98	0.16	19.47	0.48
FeO	30.95	1.41	32.06	0.49	32.07	0.45	31.11	1.33
Cr_2O_3	0.01	0.01	0.01	0.01	0.01	0.01	0.01	0.01
MnO	0.40	0.03	0.42	0.03	0.41	0.03	0.37	0.04
MgO	12.11	0.58	12.03	0.28	12.22	0.20	12.46	0.51
CaO	0.20	0.63	0.04	0.01	0.05	0.03	0.06	0.03
Na_2O	0.03	0.01	0.01	0.01	0.03	0.02	0.02	0.01
K_2O	0.25	0.41	0.04	0.01	0.07	0.04	0.21	0.38
H_2O*	11.08	0.09	10.99	0.05	10.97	0.04	11.10	0.14
Total	99.69		99.42		99.29		99.85	
cation (O = 14)								
Si	2.697	0.051	2.627	0.011	2.669	0.013	2.696	0.031
Al^{IV}	1.303	0.051	1.373	0.011	1.331	0.013	1.304	0.031
Al^{VI}	1.176	0.075	1.162	0.015	1.115	0.013	1.174	0.048
Ti	0.024	0.064	0.003	0.002	0.006	0.003	0.007	0.003
Fe	0.001	0.123	2.929	0.053	2.935	0.041	2.813	0.109
Cr	2.803	0.001	0.001	0.000	0.001	0.001	0.001	0.001
Mn	0.037	0.003	0.038	0.003	0.038	0.003	0.001	0.003
Mg	1.955	0.083	1.959	0.041	1.992	0.032	2.006	0.069
Ca	0.023	0.075	0.004	0.001	0.005	0.003	0.007	0.004
Na	0.005	0.006	0.003	0.004	0.006	0.007	0.003	0.006
K	0.035	0.047	0.006	0.004	0.010	0.012	0.029	0.036
Total	10.059	0.578	10.106	0.145	10.109	0.140	10.040	0.341
Fe/(Fe+Mg)	0.411		0.401		0.404		0.416	
T (° C)	358	17	380	3	367	4	358	10

Abbreviations: FeO represents the total Fe. **T (°C) is calculated from the equation by Cathelineau (1988).

H2O* is calculated water content.

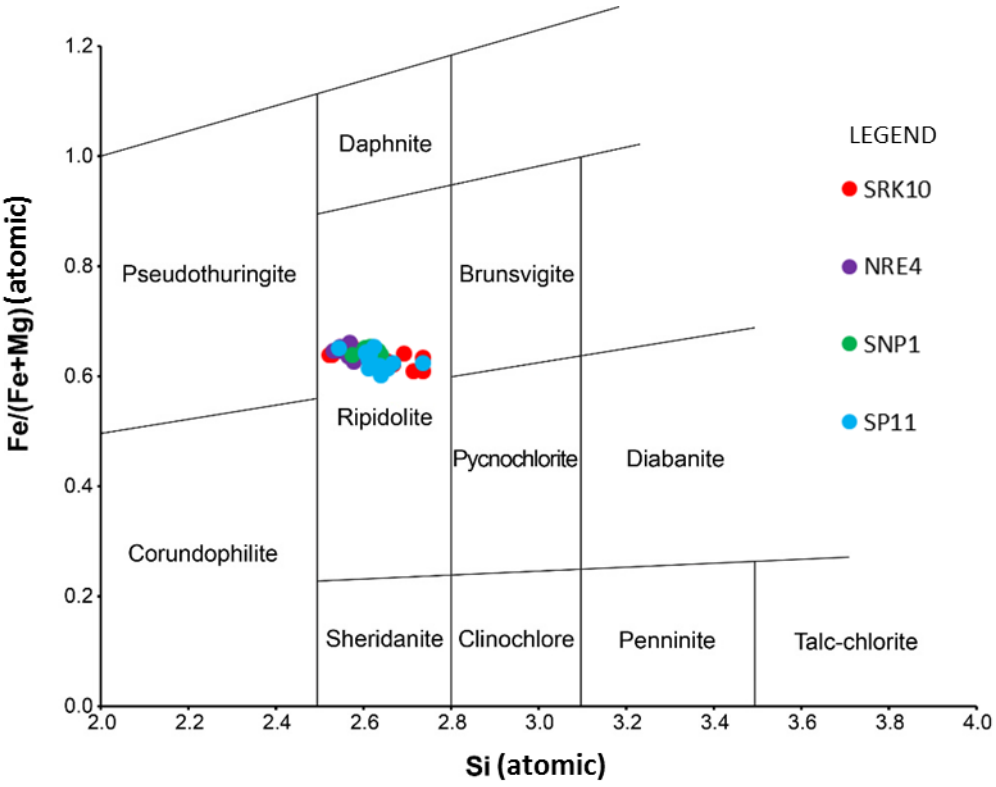

Figure 27: Chemical composition of chlorite associated with the hydrothermal veins at the Mowana deposit. Classification diagram after Heys, (1954).

5.4 Chlorite geothermometry

Temperature, pH and fO_2 of the hydrothermal fluid are the controlling factors of the chlorite composition (De Caritat et al., 1993). According to previous researches, Al^{IV} content in chlorite can be used to estimate the temperature of crystallization in various geological environments including hydrothermal systems since it is less affected by compositional variations of the host rock ((Cathelineau and Nieva, 1985; De Caritat et al., 1993). Therefore, a relationship between the tetrahedral Al^{iv} concentration in chlorite and formation temperature has been formulated by Cathelineau (1988) as follows;

$$T(°C) = 321.98Al^{IV} - 61.92$$

The chemical composition of chlorite was calculated based on 14 oxygens. The formation temperatures calculated for the Type 1 veins gave a temperature range of 340 to 400 °C, and a temperature mode of 370 to 380 °C (Fig. 28). The chlorite from the samples in or proximal to the veins gave higher temperatures compared to the ones away from the veins. The temperature obtained was used to estimate the sulfidation state of the Type 1 veins (Fig. 29). Appendix IV presents the complete EPMA analysis results for chlorite.

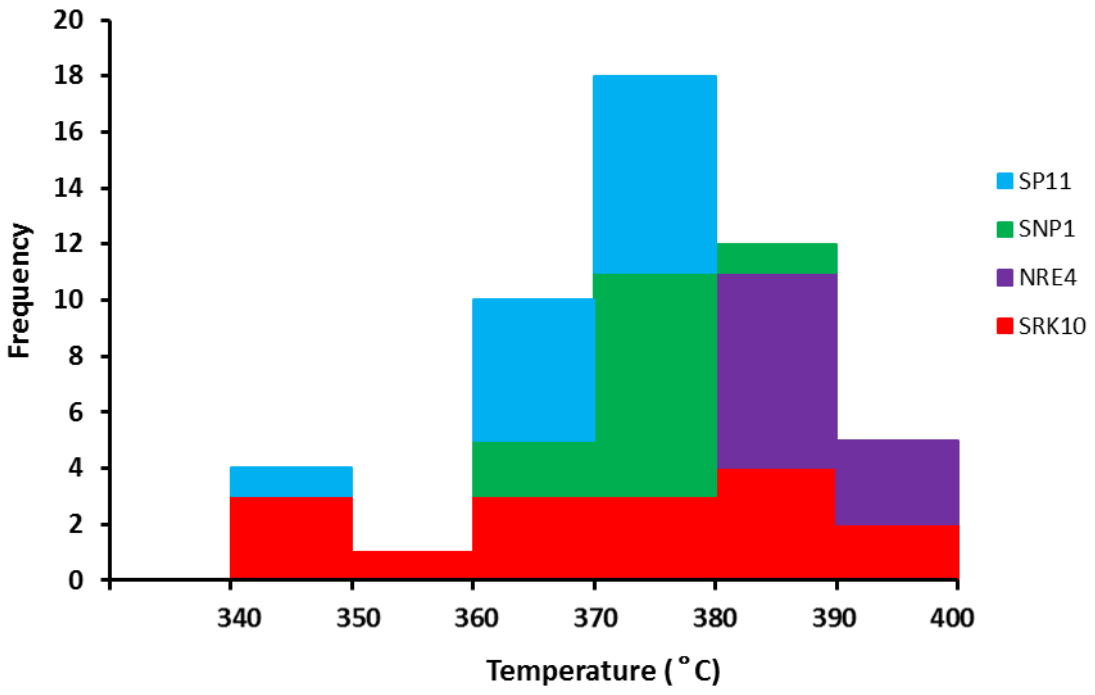

Figure 28: Histogram of the temperature estimated from the chlorite associated with the mineralized veins.

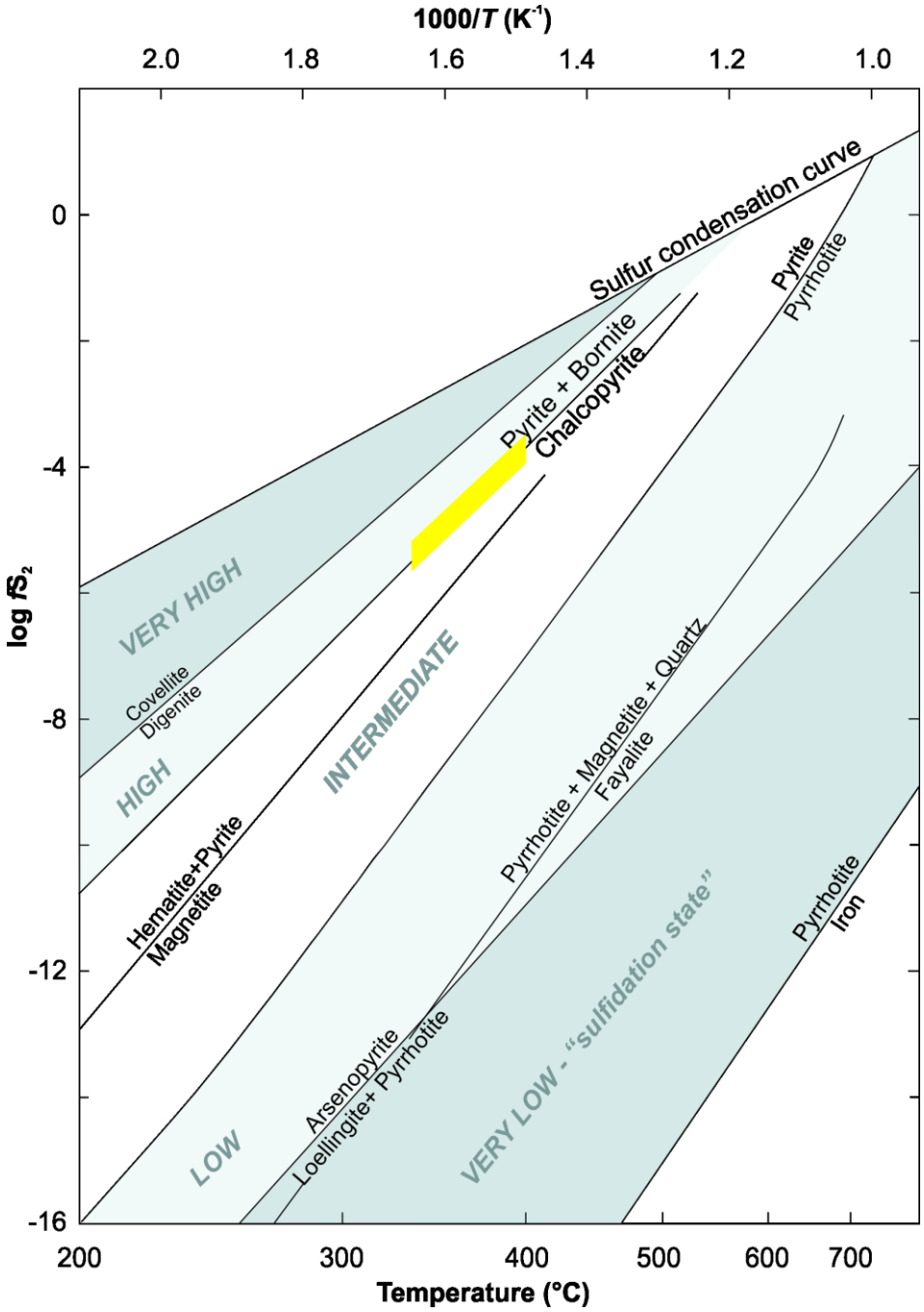

Figure 29: Log fS_2-1000/T diagram (after Einaudi et al., 2003) showing the sulfidation state for the Type 1 veins of the Mowana deposit. The sulfidation state of the Type 1 veins is plotted using the ore mineral assemblage and chlorite geothermometry data.

5.5 Discussion and Conclusions

Chalcopyrite coexisting with other sulfides such as galena is often the least preferred host for trace elements which results in low concentration of Co, Se, Ag and Bi (George et al., 2016). However, the chalcopyrite in this study shows elevated contents of Ag. This may be because silver is refractory and may have partitioned into the chalcopyrite. The Ag may have been incorporated into the Cu site of the chalcopyrite structure in Type 1 of mineralization at Mowana deposit. This might also suggest that there was a significant Ag content within the primary mineralizing fluids during chalcopyrite crystallization of Type 1 veins.

In general, the Co contents in pyrite are correlative with the temperature level, whereby high-temperature pyrite, medium-temperature pyrite, and low-temperature pyrite have Co concentrations as: >1000 ppm, 100-1000 ppm and <100 ppm, respectively (Mei, 2000). The Co contents of pyrite of Type 1 are in the range 20 ppm to 960 ppm. The Pyrite from Type 1 veins of the Mowana deposit recorded Co/Ni in the range 1.0 wt.% to 46.5 wt.%. S may be isomorphically replaced by As in pyrite, and As tends to be enriched in low temperature systems (Liu et al., 2018). The stage 1 pyrite has As contents up to 720 ppm. Zhou et al. 2005, suggested that the Fe/(S+As) ratio values of pyrite positively correlate their formation depth, the ratios of deep formation environments, medium-depth environments and shallow environments are: 0.846, 0.863 and 0.926, respectively. Most of the values from the pyrites of Mowana deposit are in the range 0.849 and 0.873 indicating the medium to shallow formation environment. The Co and Ni contents in pyrite can reflect the origin of pyrite (Bralia et

al., 1979). The Co/Ni ratios detected in the Type 1 pyrite widely vary between 1 and 4.25 which is coherent with the characteristics of a magmatic-hydrothermal pyrite.

Pb contents are relatively elevated which can be ascribed to small-scale inclusions of galena in pyrite (Houston et al. 1995).

Keith et al., 2016, indicated that Te content in pyrite links to depth with the concentration of Te high in pyrite formed at deeper levels in comparison to pyrite formed at shallow levels. On the contrary, Keith et al., 2018 indicated that the concentration of Te in pyrite is not dependent on temperature. Te content in pyrite from this study is 12.2 ppm on average.

Although its speculative in this study to account for the elevated Ag contents (1770 ppm) in galena because the Bi contents were not analyzed, and the Sb concentrations are below the detection limit, previous researches have linked the elevated Ag contents in galena to the incorporation of Ag in the crystal structure of galena with the help of Bi^{3+} and/or Sb^{3+} via coupled substitution;

$Ag^{+} + (Bi, Sb)^{3+} \longleftrightarrow 2Pb^{2+}$ (e. g. George et al., 2015, Chutas et al., 2008). However, this might not be the case at the Mowana deposit since the Bi contents of Ag were not determined and the Sb concentrations in Ag were very low.

The elevated Cu concentrations in galena indicate that the Cu is incorporated in the galena structure by solid solution (George et al., 2015). The concentration of selenium is likely incorporated into the galena through the involvement of solid solution with clausthalite (PbSe) through the substitution $Se^{2-} \longleftrightarrow S^{2-}$ at temperatures above 300°C (Liu and Chang, 1994). Grant et al., 2018 previously indicated selenium as a temperature mineral wherein the concentration of Se in pyrite increased with increase

in temperature. Galena from Cu rich ores of the VHMS deposit has shown high selenium concentrations compared to the Cu-poor ores (Carvalho et al., 2018). This has been linked to proximity to the mineralizing fluid source (Carvalho et al., 2018).

CHAPTER 6: FLUID INCLUSION ANALYSIS

6.1 Introduction

This chapter presents the fluid inclusion study conducted on the Mowana deposit. The analysis was conducted on the mineralized quartz veins. The intention of this analysis was to determine the formation temperature of the deposit. To further determine the salinity of the hydrothermal fluids derived from freezing and ice melting temperatures and finally to determine the mechanisms of ore deposition.

6.2 Methodology

Doubly polished thin sections of 16 quartz samples with about 200-400 μm thickness were prepared from the mineralized quartz veins for fluid inclusion analysis. Fluid inclusion assemblages were determined using the Nikon ECLIPSE LV100NPOL polarising microscope. Microthermometric analyses were carried out using the Linkam THMS600 stage for both heating and freezing in conjunction with the Nikon ECLIPSE LV100NPOL. This analysis was conducted at Akita University.

6.3 Results

Fluid inclusion petrography was conducted on the mineralized quartz veins. Both primary and pseudo secondary fluid inclusions were documented. The primary inclusions are the ones that occur along the growth zones of the crystals (Roedder, 1979). The primary fluid inclusions were trapped during the initial crystal growth

(Roedder, 1979). Pseudo-secondary fluid inclusions occur along fractures and cracks that formed and healed during crystal growth.

Fluid inclusions found in the quartz are dominantly liquid-rich liquid vapor fluid inclusions. Mono-phase gas inclusions were also observed. However, the fluid inclusions were quite small to conduct microthermometry (Fig. 29).

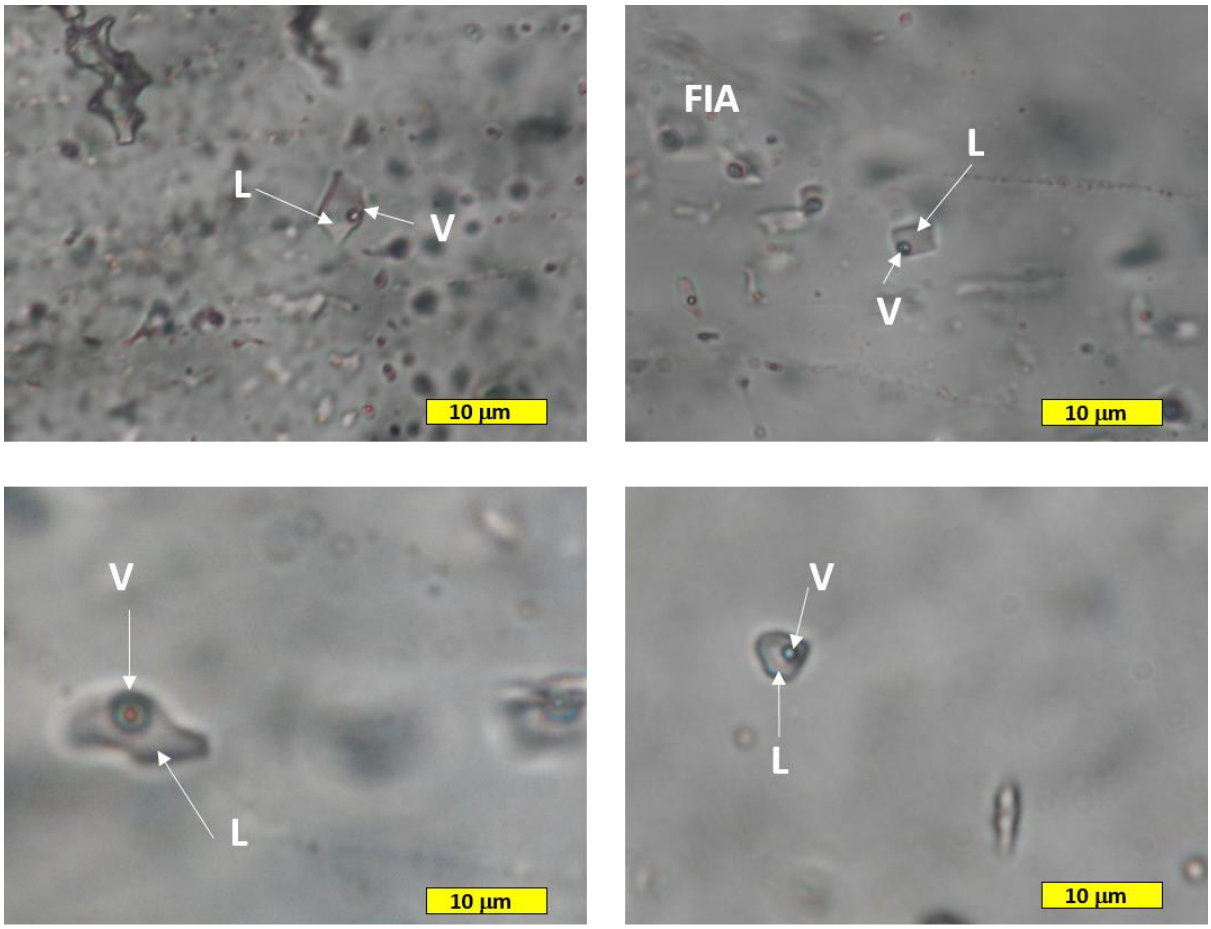

Figure 30: Representative photomicrographs of fluid inclusions in the mineralized quartz veins.

CHAPTER 7: STABLE ISOTOPES ANALYSES

7.1 Introduction

This chapter presents the stable isotopes (C, O, S) analyses on quartz and calcite from the mineralized veins, host rocks, and the sulfides collected from both the hypogene and supergene stages of the type 1 and type 2 veins mineralization at Mowana deposit. These analyses aimed to determine the source of the ore-forming fluids for the deposit and the origin of carbon for the carbonates.

7.2 Methodology

Stable isotope measurements (^{18}O, ^{13}C) of quartz and calcite minerals were outsourced to GNS Science in New Zealand. For the measurement of O-18 in quartz samples, oxygen was extracted using a CO_2-laser and BrF_5 (Sharp, 1990). Oxygen isotope values are reported in the $\delta^{18}O$ notation relative to the Vienna Standard Mean Ocean Water (VSMOW). The samples were normalized to the international quartz standard NBS-28 with value of +9.6 per mil (‰) or UWG-2 Garnet with value of +5.8 per mil (‰). The samples and standards were first heated overnight to 150°C before loading into the vacuum extraction line. These were then evacuated for approximately 6 hours. Blank BrF_5 runs were conducted until yield was less than 0.2 µmoles oxygen. Oxygen yields were then recorded, as CO_2 gas was analysed on a Geo20-20 mass spectrometer. The carbonates on the other hand were analyzed using the GVI IsoPrime Carbonate Preparation System with a reaction temperature of 25°C for 24 hours and run through a dual inlet on the IsoPrime mass spectrometer. The results

are reported relative to the Vienna Pee Dee Belemnite (VPDB) and normalized to the GNS internal standards GNS Marble with reported values of 2.04 ‰ for $\delta^{13}C$ and -6.40 ‰ for $\delta^{18}O$. The external precision of the measurements are better than 0.1‰ for $\delta^{13}C$ and 0.2 ‰ for $\delta^{18}O$.

For sulfur isotopes, the ore samples were crushed and sulfide minerals (chalcopyrite, pyrite, galena and chalcocite) were handpicked using a pair of pincers under the Nikon SMZ 1500 binocular microscope. The optimum weight of about 20 to 50 mg of pure sulfides placed in a beaker was then mixed with 20 ml 16 M nitric acid (HNO_3) and about 2 ml bromine (Br_2) under ventilation system. Watch glass was used to close the beaker to avoid the evaporation of the mixed acid solution. The mixture was then heated to digest the sulfides at 90 degrees Celsius on a hot plate. After digesting all the sulfides, the mixture was let to evaporate for a day. The resulting mixture was diluted with 10 ml 6 M HCl and 90 ml distilled water to make a 100 ml solution. The solutions with precipitate were filtrated. The solution was subjected to cation exchange by passing the solution through the resin columns. 10 ml of 10% $BaCl_2$ was added to the collected sample solution to total solution about 300 ml and heat overnight to precipitate $BaSO_4$. About 40 to 50 ml of the resulting mixture of water and $BaSO_4$ was filtered and the $BaSO_4$ leftover was dried overnight. Approximately 0.4-0.5 mg $BaSO_4$ recovered powders, mixed with 5 to 7 times V_2O_5, were loaded into tin capsules. The tin capsules containing the samples folded into cubes were analyzed using a Flash 2000 continuous flow-elemental analyzer on a Thermo Fisher Science Delta-V Advantage isotope ratio mass spectrometry at the Department of Earth Resource Science, Akita University. Analytical precision was ±0.2‰. The sulfur isotope compositions are reported in standard δ notation relative to the sulfur isotopic

ratio of Canyon Diablo meteorite troilite (CDT). The NSB-127, SO5, and SO6 house standards were used for analytical correction.

7.3 Results

7.3.1 Carbon isotopes

Table 2 shows the results for the carbon and oxygen isotopic compositions of the carbonates, graphitic schist, as well as the calcite, and quartz from the hydrothermal veins. The measured carbon ($\delta^{13}C$) isotopic compositions of the bulk rock carbonates (limestone/dolomite) have a narrow range between 6.05 and 6.89 ‰. The graphitic schist has the average $\delta^{13}C$ value of -26 ‰ with values ranging between -29.8 and -21.0 ‰. Oxygen and carbon isotopic compositions for co-existing quartz and calcite in the mineralized Type 1 veins were analyzed. The measured carbon isotope ($\delta^{13}C$) values of calcite range from -11.96 to 0.53 to ‰. The oxygen isotope values ($\delta^{18}O$) of quartz range from -9.25 to 10.29 ‰. The $\delta^{18}O$ of the calcite relative to PDB range from -22.34 to -12.42 ‰. The recalculated $\delta^{18}O$ values of the calcite relative to SMOW range between 7.88 to 18.11 ‰. The recalculations were done using the equation,

$$\delta^{18}O_{VSMOW} = 1.03091 * \delta^{18}O_{VPDB} + 30.91 ‰$$

The histogram representing the distributions of the isotopic compositions is shown in figure 31 below.

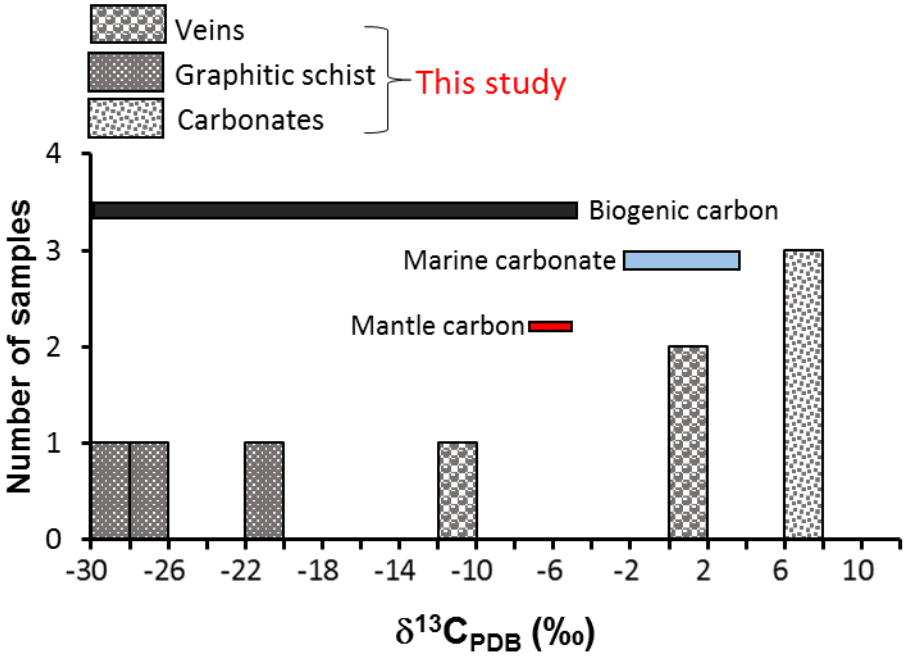

Figure 31:Distributions of $\delta^{13}C$ obtained for the carbonates and graphitic schist of the Mowana deposit. Biogenic carbon, marine carbon and mantle carbon isotopic compositions are from Criss (1995).

Table 4: Carbon and oxygen isotopic compositions of the limestone, graphitic schist, vein calcite and quartz from the Type 1 veins of the Mowana deposit.

Sample ID	$\delta^{13}C_{PDB}$ (‰)	$\delta^{18}O_{VPDB}$ (‰)	$\delta^{18}O_{SMOW}$	Rock/Mineral name
L2	6.65	-12.81	17.70	Limestone
L3	6.89	-10.2	20.39	Limestone
L18	6.05	-8.14	22.52	Limestone
G2	-29.8			Graphitic schist
G3	-21.0			Graphitic schist
G4	-27.2			Graphitic schist
NP89b	0.53	-20.92	9.34	Calcite-Type 1 vein
MP1b	0.46	-22.34	7.88	Calcite-Type 1 vein
NP2b	-11.96	-12.42	18.11	Calcite-Type 1 vein
NP89a			10.29	Quartz-Type 1 vein
MP1a			9.25	Quartz-Type 1 vein
NP2a			10.1	Quartz-Type 1 vein

7.3.2 Sulfur isotopes

Sulfur isotopic ratios were determined on the sulfides (chalcopyrite, pyrite, galena, and chalcocite) separated from the Type 1 and Type 2 veins. A single sample of disseminated pyrite in silicified limestone, interpreted as diagenetic was also analyzed. The $\delta^{34}S$ of five chalcopyrite samples from the quartz+calcite±K-feldspar veins range from -0.8 ‰ to +3.3 ‰. The $\delta^{34}S$ of two pyrite samples from the silicified limestone and Type 1 vein are higher, +15.4 ‰ and +18.0 ‰ respectively. The diagenetic pyrite occurs parallel to the lamination of the host rock and appears slightly modified (Figure 31). The pyrite from the Type 1 mineralized vein occurs as cement to the clast of the breccia (Figure 31). The $\delta^{34}S$ of a single galena sample from the galena-bearing quartz+calcite±fluorite veins is -4.2 ‰. Three chalcocite samples from the supergene stage of the quartz+calcite±K-feldspar veins yielded a narrow $\delta^{34}S$ range between 4.3 ‰ and +0.9 ‰. A list of values obtained from the analyzed sulfides is presented in Table 4 and a histogram presenting the sulfur isotopic compositions of the sulfides is shown in Figure 30.

Table 5: Sulfur isotopic compositions and the corresponding vein types of the Mowana deposit

Locality	Sample name	Mineral	$\delta^{34}S$ (‰)	Stage	Mode of occurrence (description)
SRK10	G4	py	+15.4	Diagenetic	Disseminated in silicified limestone
BINF9	E4	py	+18.0	Type 1	Q+C±K-vein
CINF28	A3	ccp	-0.8	Type 1	Q+C±K-vein
SRK10	G12	ccp	+2.6	Type 1	Q+C±K-vein
AINF6	C5	ccp	+1.6	Type 1	Q+C±K-vein
SRK10	G10	ccp	+3.3	Type 1	Q+C±K-vein
SRK10	G6	ccp	+2.8	Type 1	Q+C±K-vein
MZC	SNP4	ccp	+2.6	Type 1	Q+C±K-vein
MZC	NNP9	ccp	+3.0	Type 1	Q+C±K-vein
MZC	SNP6	ccp	+3.4	Type 1	Q+C±K-vein
MZA	SP6	gn	-4.2	Type 2	Q+C±F-vein
AINF26	D4	cc	+0.8	Supergene	Replacing ccp in Q+C±K-vein
MZC	NNP1	cc	+0.9	Supergene	Q+C±K-vein
AINF6	D3	cc	-4.3	Supergene	Q+C±K-vein

Abbreviations: ccp-chalcopyrite; cc-chalcocite; gn-galena; py-pyrite; Q+C±K- quartz+calcite±K-feldspar veins; Q+C±F-quartz+calcite±fluorite veins. Locality names MZA (Mining zone A) and MZC (Mining zone C) represents the different mining zones as shown in Figure 4.

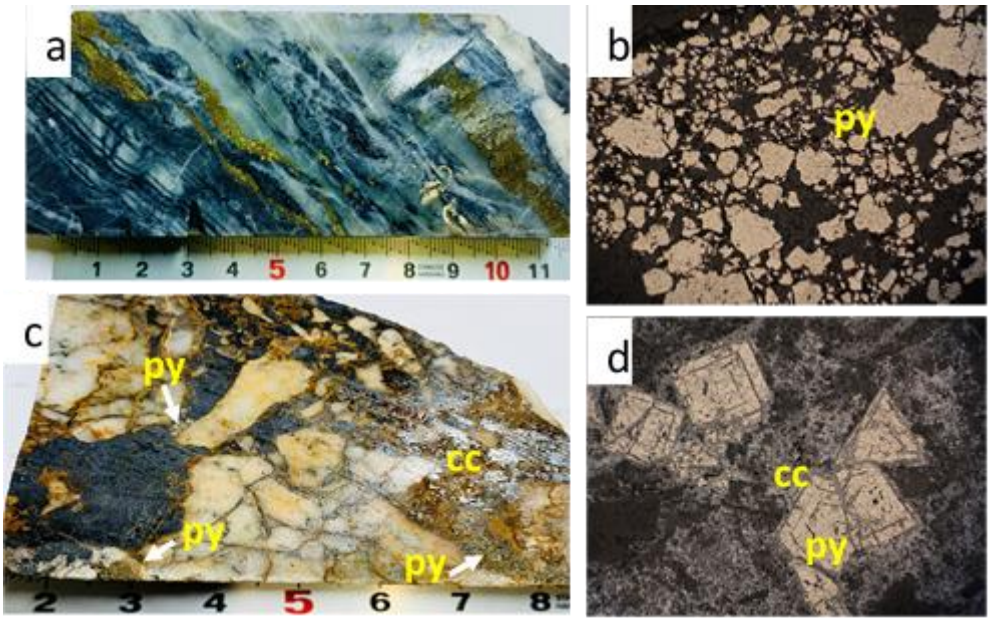

Figure 32: Representative hand specimens, and the photomicrographs showing the occurrence and morphology of the pyrite from Mowana deposit. (a-b) Pyrite deposited along the lamination of the silicified limestone (host rock). (c-d) Pyrite occurs as cement to the quartz-calcite clasts in the vein breccia from type 1 veins. Mineral abbreviations: cc-chalcocite, py-pyrite

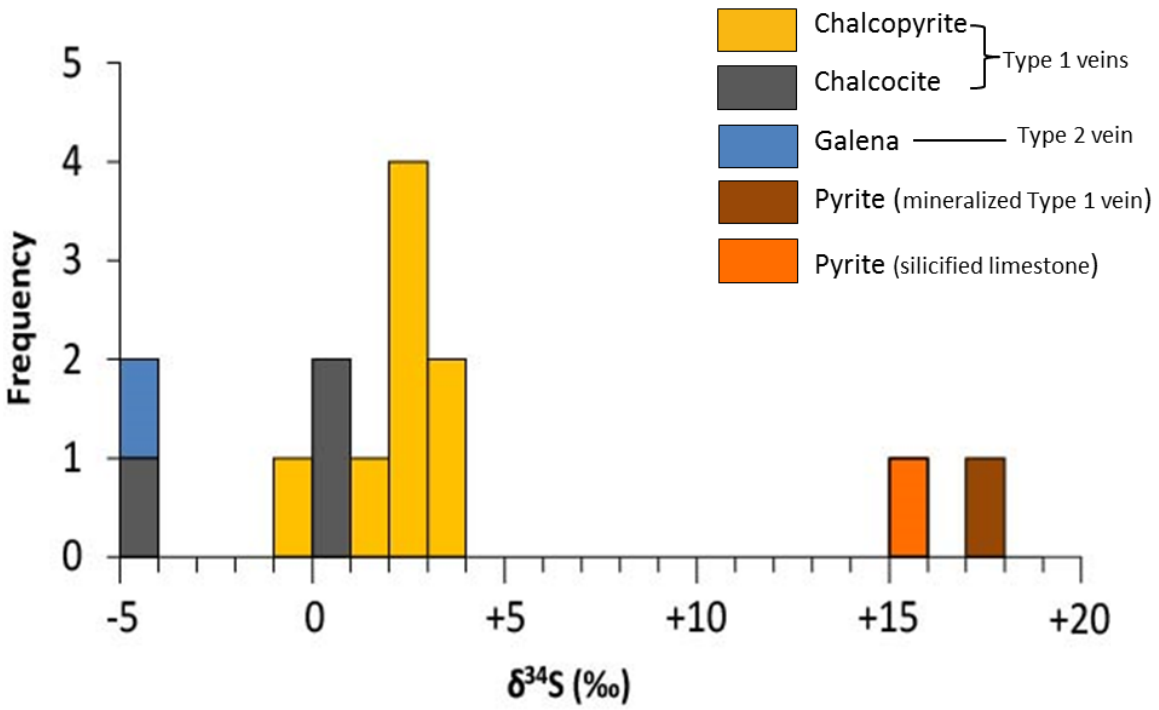

Figure 33: Histogram showing sulfur isotopic compositions (as $\delta^{34}S_{CDT}$ per mil) of sulfides in the Mowana deposit.

7.4 Formation temperature based on oxygen isotopes geothermometer

The calcite and quartz from the mineralized type 1 veins co-exist in the samples and show equilibrium textures. Therefore, the $\delta^{18}O$ values of the calcite-quartz pairs were used to calculate the crystallization temperature. The temperature was calculated based on the following equation: $1000\ln\alpha_{qz\text{-}cal} = 0.38\ (10^6/T^2)$ Clayton et al. (1989).

Table 6: Formation temperature for the Type 1 veins

Quartz $^{18}O_{SMOW}$	Calcite $^{18}O_{SMOW}$	$\Delta^{18}O_{Quartz\text{-}Calcite}$	Temp(K)	Temp °C
10.29	9.34	0.95	632	359
9.25	7.88	1.37	527	254
10.1	18.11	-8.01		

The calculated temperature ranges between 250 and 360 °C. This temperature overlaps with the temperatures estimated from both the hydrothermal alteration

mineral assemblage (250 to <340 °C) and chlorite geothermometry (340 to 400 °C). Barton et al. (1994) attributed the quartz oxygen isotopic compositions around 10 ‰ (9.25 to 10.30 ‰ in this study) to possibly indicate crystallization from reasonably high temperatures.

7.5 Origin of Carbon

The carbon isotopic composition $\delta^{13}C$ (average -26 ‰) of reduced carbon in the graphite are similar to the ones reported by the previous researcher and the average corresponds to the global average of -25 ‰ (Schidlowski, 2001). The values correspond to being derived from biogenic activity. The stratigraphy of the Matsitama schist belt to which the deposit belongs is dominated by shallow water clastic metasediments (Majaule et al., 1997). Therefore, it is likely that oxygenic photosynthesis was established at that time and the cyanobacteria were fully active (Grassineau et al., 2006).

The $\delta^{13}C$, ~+6 ‰ of the metacarbonates are unusual compared to the global trend and rarely observed in Archean carbonates (Fig. 34). The sedimentary marine carbonates are characterized by a narrow range of values around 0 ±3 ‰ (Kahur et al., 2020) indicating marine source for the carbonate rocks. These heavy values can be explained by diagenetic carbonate precipitation during which dissolved inorganic C is enriched in ^{13}C by methanogenic processes (Hayes et al., 2006), or alternatively by burial of reduced carbon in an isolated basin at that time, with the residual dissolved carbon being enriched in ^{13}C. Therefore, the resultant heavy isotopic signatures will reflect on the later precipitating carbonates. The heavy carbon isotopic compositions of the vein calcite which range from 0.46 ‰ to 0.53 ‰ in this study, could indicate crystallization from fluids dominated by either meteoric or marine water (Barton et al.

1990). A mixed source of C could also be attributed for the vein calcite since the vein calcite presented $\delta^{13}C$ values (-11.96 to 0.53 ‰) intermediate between those $\delta^{13}C$ values from the limestone (~+6 ‰) and graphitic schist (~+26 ‰ average). Moreover, a single value recorded for the $\delta^{13}C$ of calcite could possibly suggest remobilization of C from the graphite since the value is relatively too low (-11.96 ‰).

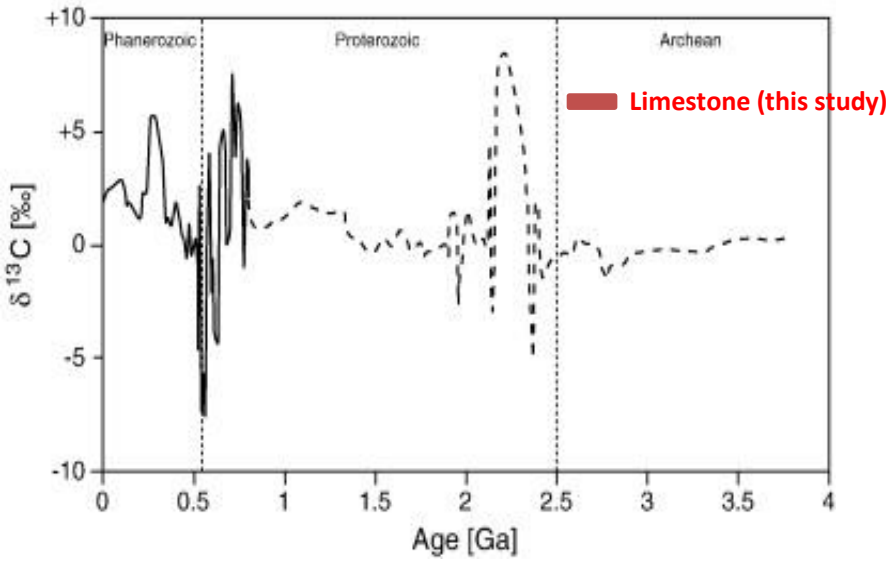

Figure 34: Record of $\delta^{13}C$ values throughout the Earth history (Och and Shields-Zhou, 2012)

7.6 Origin of Sulfur

The S isotopic compositions of the analyzed samples pose a range of possibilities for the source of S at the Mowana deposit. A relatively large population of the $\delta^{34}S$ of the analyzed samples falls in the range between -5 ‰ and +4 ‰. The calculated $\delta^{34}S$ of aqueous H_2S in the fluid for chalcopyrite ranges from -0.7 ‰ to +3.5 ‰, while that of chalcocite falls in the range from -2.4 ‰ to +2.7 ‰. The $\delta^{34}S$ of aqueous H_2S in the fluid for galena is +2.6 ‰. These values indicate that these minerals formed from the same mineralizing fluid with a slight fluctuation in the S-isotopic value. Similar $\delta^{34}S$ values (in the range +2.5‰ to +5.3‰) of the three co-existing sulfides (pyrite, galena and sphalerite) were also reported by Barton et al.

(1994). The narrow range near 0 ‰ is typical of a magmatic source (Ohmoto and Rye, 1979), but may also have derived from leaching of rocks having similar S isotope compositions (Canfield, 2005). The S isotope composition of Archean sedimentary and diagenetic pyrite has narrow $\delta^{34}S$, mostly between -5 ‰ and +5 ‰ (Canfield, 2005). Given the absence of a possible magmatic source coeval with the mineralization, the metasedimentary rocks associated with the Mowana mineralization are tentatively proposed as a possible source of S with $\delta^{34}S$ values around 0 ‰.

In contrast, the higher $\delta^{34}S$ values of the pyrite ranging between +15.4 ‰ and +18.0 ‰ indicate isotopic disequilibrium with other sulfides, despite the spatial association and require a separate source of S. The calculated $\delta^{34}S$ values of the aqueous H_2S in the fluid in equilibrium with the pyrite range between +14.4 ‰ and +17.0 ‰.

The $\delta^{34}S$ of pyrite (+15.4 ‰) from the silicified limestone can be attributed to closed system sulfate reduction wherein the residual sulfate will be progressively enriched in ^{34}S hence producing heavier sulfur isotopic signature in the resulting pyrite (Grassineau et al., 2001, 2006). The $\delta^{34}S$ value of +18.0 ‰ measured in pyrite of a Type 1 vein may be explained in two scenarios. The first scenario concerns the remobilization of the $\delta^{34}S$ rich diagenetic pyrite during brecciation. The second scenario pertains to the closed system thermochemical reduction of seawater sulfate from Proterozoic (~2 Ga) seawater. The timing of the mineralization at Mowana is estimated at ~2.0 Ga (Barton et al., 1994) at which the $\delta^{34}S$ of the seawater was at around +20 ‰ (Farquhar et al., 2011). Thermochemical sulfate reduction results in equilibrium S isotopic fractionation ($\delta^{34}S$ sulfate - $\delta^{34}S$ sulfide = ca. +17 ‰ at temperatures of 300–350 °C; Ohmoto 1986). If we consider isotopic equilibrium

between sulfide and sulfate in the assumed ore-forming temperature of 300-350 °C, the sulfide should have $\delta^{34}S$ value around +3 ‰. However, near-quantitative reduction of sulfate in a closed system will result in sulfide with S-isotope values approaching the initial $\delta^{34}S$ of sulfate.

Although inconclusive, Barton et al. 1990, analyzed the Pb isotopic compositions of galena, pyrite, and chalcopyrite from the then bushman deposit to infer the source of metals. The galena and the chalcopyrite and pyrite indicated they were precipitated from fluids of different Pb isotopic compositions. In comparison with the data by Coomer et al., 1977, from the other deposits in the Matsitama schist belt the origin of Pb in these areas proved different.

CHAPTER 8: CONCLUSIONS

Sulfide mineralization at the Mowana deposit is hosted in a sliver of strongly deformed (sheared) and hydrothermally altered metasedimentary rocks of the Matsitama Schist Belt tectonically interlayered with the granite-gneiss of the Motloutse-Mosetse Complex. Mowana deposit possess specific characteristics different from other Archean greenstone belt- hosted deposits. These include inferred long-time gap between rock formation and mineralization (the mineralization is unrelated to the greenstone formation, and rather related to intracratonic deformation at ~2 Ga). The mineralization is shear zone related and dominated by Cu, Pb and Zn as opposed to Au which is common in other Archean greenstone belt- hosted deposits.

The hydrothermal alteration of the host rocks is characterized by silicification, chloritization, epidotization, sericitization, hematite, and carbonate alterations. The alteration assemblage in the main mineralization stage (Type 1 veins) is coherent with formation from near-neutral pH mineralizing fluids at temperatures in the range 200 °C to ~>340 °C. This temperature coincides with the temperature of 340-400 °C obtained from the chlorite geothermometry.

The mineralization evolved in at least two mineralization vein types. The Type 1 is characterized by the precipitation of chalcopyrite, pyrite and primary bornite, with minor galena within the quartz+calcite±K-feldspar veins. Type 2 is manifested by galena hosted in quartz+calcite±fluorite veins.

This study has established that the Type 1 veins at the Mowana deposit formed under intermediate to high sulfidation state based on the mineral assemblage and temperature obtained from chlorite geothermometry. The superficial levels of the

deposit are characterized by supergene enrichment minerals resulting from the oxidation and weathering of the ore minerals. Chalcocite, bornite, covellite, and anglesite occur as supergene minerals. Oxidation mineral assemblage includes hematite, goethite, and malachite.

The mineralized quartz+carbonate veins of the Mowana deposit display primary growth textures, including zoned, and comb textures. Recrystallization textures are present as mosaic and feathery quartz.

Based on mineral chemistry, elevated Ag concentrations in Type 1 veins chalcopyrite could be linked to the incorporation of Ag in the Cu site of the chalcopyrite. High selenium concentration in galena is attributed to the incorporation of Se into galena through the involvement of solid solution with PbSe via substitution at temperatures beyond 300°C. Quartz from the mineralized samples host two-phase liquid rich and vapour inclusions.

The main mineralization in the hydrothermal veins (Type 1 veins) occurred at temperatures ranging between 300 to 400 °C as evidenced by chlorite geothermometry on chlorites associated with the mineralization. This temperature is supported by the temperature from carbon and oxygen isotope compositions (250 to 360 °C).

The carbon isotopic composition $\delta^{13}C$ values of graphite from graphitic schist (average -26 ‰) corresponds to a biogenic origin, possibly from cyanobacteria living in shallow sea. The heavy $\delta^{13}C$ values of the metacarbonates could be obtained either during diagenetic precipitation of the carbonates through methanogenic processes or burial of reduced carbon in an isolated basin. The C isotope composition of vein

carbonate suggest a mixture of the carbon source from the limestone and the graphitic schist.

The sulfur isotopic compositions can possibly be grouped into two potential sources of sulfur at Mowana deposit. The $\delta^{34}S$ values relatively close to 0 ‰ (-5 ‰ to +4 ‰) are indicative of either magmatic source or leaching of the host metasedimentary rocks. Moreover, the higher $\delta^{34}S$ values (+15.4 ‰ and +18.0 ‰) are linked to closed system sulfate reduction and the remobilization of the $\delta^{34}S$ rich diagenetic pyrite during brecciation.

REFERENCES

African Copper PLC (2005) Annual Report, Unpublished report, 22p.

African Copper PLC (2008) Annual Report, Unpublished Report, 52p.

Aldiss, D.T. (1991) The Motloutse Complex and the Zimbabwe Craton/Limpopo belt transition in Botswana. Precambrian Research, 50, 89-109.

Bagai, Z., Armstrong, R. A. and Kampunzu, A. B. (2002) U-Pb single zircon geochronology of granitoids in the Vumba granite-greenstone terrane (NE Botswana) Implications for the Archean Zimbabwe craton. Precambrian Research,118, 149-168.

Barton, J. M., Blaine, J. L., Doig, R. and Byron, C. L. (1994) The geological setting and style of copper mineralization at the Bushman group of deposits, northeastern Botswana. Journal of African Earth Sciences, 18, 87-97.

Berger, B. R., (1982) The geological attributes of Au-Ag-base metal epithermal deposits. In Erickson, R. L., (compiler) Characteristics of mineral deposits occurrences. U.S. Geological Survey, Open File Rep. 82-795, p. 119-126.

Blekinsop, T. G., Martin, A., Jelsma, H.A. and Vinyu, M.L. (1997) The Zimbabwe Craton. In: de Wit, M. J. and Ashwal, L. D. (eds). Greenstone Belts. New York, Claredon Press, 567-580.

Bolhar, R., Hofmann A., Kemp, A. I. S., Whitehouse, M. J., Wind, S. and Kamber, B. S. (2017) Juvenile crust formation in the Zimbabwe Craton deduced from the

O-Hf isotopic record of 3.8 - 3.1 Ga detrital zircons. Geochimica et Cosmochimica Acta, 215, 432-446.

Bottrill, T. J. (1998) Progress Report on the Matsitama Project, Botswana: A Report for Mortbury, Unpublished Report, 175p.

Bralia, A., Sabatini, G., Troja, F.A. (1979) A revaluation of Co/Ni ratio in pyrite as a geochemical tool in ore genesis problems. Mineral deposita, 14, 353-374.

Canfield, D. E. (2005) The early history of atmospheric oxygen: Homage to Robert M. Garrels. Annual Review of Earth and Planetary Sciences, 33, 1-36.

Carney, J. N., Aldiss, D. T. and Lock, N. P. (1994) The geology of Botswana. Geological Survey of Botswana, 37, 17-30.

Carvalho, J. R. S., Relvas, J., Pinto, A. M. M., Frenzel, M., Krause, J., Gutzmer, J., Pacheco, N., Fonseca, R., Santos, S. and Caetano, P. (2018) Indium and selenium distribution in the Neves-Corvo deposit, Iberian Pyrite Belt. Portugal Mineralogy Magazine, 82, S5-S41.

Cathelineau, M. (1988) Cation site occupancy in chlorites and illites as a function of temperature. Clay minerals, 23, 471-485.

Cathelineau, M. and Nieva, D. (1985) A chlorite solid solution geothermometer. The Los Azufres (Mexico) geothermal system. Contributions to Mineralogy and Petrology, 91, 235-244.

Coomer, P. G., Coward, M. P. and Lintern, B. C. (1977) Stratigraphy, structure, and geochronology of ore leads in the Matsitama Schist Belt of northern Botswana. Precambrian Research, 5, 23-41.

Chisenga, C., Jianguo, Y.P., Fadel, I., Meijde, M. and Atekwana, E.A. (2020) Updated tectonic terrane boundaries of Botswana determined from gravity and aeromagnetic data. Episodes, 43, 919–933.

Chutas, N. I., Kress, V. C., Ghiorso, M. S. and Sack, R. O. (2008) A solution model for high-temperature PbS-AgSbS2-AgBiS2 galena. American mineralogist, 93, 1630-1640.

Clayton, R. N, Goldsmith, J. R. and Mayeda, T. K. (1989) Oxygen isotope fractionation in quartz, albite, anorthite and calcite. Geochimica et Cosmochimica Acta, 53, 725-733.

Criss, R. E. (1995) Stable isotope distribution: Variations from temperature, organic, and water rock interactions. In Thomas, A. J. (ed.) Global Earth Physics-A handbook of physical constraints. AGU Reference Shelf 1, pp.292-307. American Gophysical Union, Washington DC.

Davis, T. (2009) Review of the Structural Geology of the Mowana Copper Deposit, NE Botswana: A Report for African Copper PLC, Unpublished Report, 62p.

Dodson, M. H., Compston, W., Williams, I. S. and Wilson, J. F. (1988) A search for ancient detrital zircons in Zimbabwean sediments. Journal of the Geological Society (London), 145, 977-983.

Dong, G., Morrison, G. and Jareith, S. (1995) Quartz textures in epithermal veins, Queensland-Classification, origin, and implication. Economic geology, 90, 1841-1856.

Einaudi, M.T., Hedenquist, J.W. and Inan, E.E. (2003) Sulfidation state of hydrothermal fluids: The porphyry-epithermal transition beyond. In Simmons, S.F and Graham, I. (Eds.) Volcanic, geothermal, and ore-forming fluids: rulers and witnesses of processes within the earth. Special Publication, 10, Society of Economic Geologists Inc., Littleton, 285-313

Farquhar, J., Wu, N., Canfield. D.E. and Oduro H. (2010) Connections between sulfur cycle evolution, sulfur isotopes, sediments, and base metal sulfide deposits. Economic Geology, 105, 509-533.

Fripp, R. E. P., Lilly, P. A. and Barton, J. M. (1979) The structure and origin of the Singelele Gneiss, Limpopo Mobile Belt, South Africa. Transvaal Geological Society, South Africa, 161-167.

George, L., Cook, N. J., Ciobanu, C. L. and Wade, B. P. (2015) Trace and minor elements in galena: A reconnaissance LA-ICP-MS study. American Mineralogist, 100, 548-569.

Grant, H. L. J., Hannington, M.D., Petersen, S., Frische, M. and Fuchs, S. H. M. and (2018) Contranits on the behavior of trace elements in the actively forming TAG deposit, Mid-Atlantic Ridge, based on LA-ICPMS analyses of pyrite. Chemical Geology, 498,45-71.

Grassineau, N. V., Abell, P., Appel, P. W. U., Lowry, D.and Nisbet, E. G. (2006) Early life signatures in sulfur and carbon isotopes from Isua, Barberton, Wabigoon (Steep Rock), and Belingwe Greenstone belts (3.8 to 2.7 Ga). In Kesler, S. E. and Ohmoto, H. (eds.). Evolution of Early Earth's Atmosphere, Hydrosphere,

and Biosphere-Constraints from Ore deposits. Geological Society of America Memoir, 198, 33-52.

Hayes, J. M. and Waldbuer, J. R. (2006) The carbon cycle and associated redox processes through time;Philosophical Transactions. The Royal Society, 361, 931-950.

Haynes, S. J. (1993) Veintype ore deposits: Introduction. Ore Geology Reviews, 8, 205-211.

Henley, R. W. and Ellis, A. J. (1983) Geothermal systems ancient and modern; A geochemical review. Earth-Science Reviews, 19, 1-50.

Heys, M. H. (1954) A new review of the chlorites. Mineralogical Magazine,30, 277-292.

Hofmann, A. and Chagondah G. (2019) The Paleoarchean Record of the Zimbabwe Craton. In Van Kranendonk, M. J., Bennett, V. C. and Hoffmann J. E. (eds). Earth's Oldest Rocks. Elsevier, 855-863.

Hofmann, A., Dirks, P. G. H. M., Jelsma, H. A. and Matura, N. (2003) A tectonic origin for ironstone horizons in the Zimbabwe craton and their significance for greenstone geology. Journal of the Geological Society (London), 160, 83-97.

Huston, D. L., Sie, S. H., Suter, G. F., Cooke, D. R. and Both, R. A. (1995) Trace elements in sulfide minerals from eastern Australia volcanic-hosted massive sulfide deposits: Part 1, Proton microprobe analyses of pyrite, chalcopyrite, and sphalerite, and Part II. Selenium levels in pyrite; comparison with δ34S values and implications for the source of sulfur in volcanogenic hydrothermal systems. Economic Geology, 90, 1167-1196.

Jelsma, H.A. and Dirks, P. H. G. M. (2000) Tectonic evolution of a greenstone sequence in northern Zimbabwe: sequential early stacking and pluton diapirism. Tectonics, 19, 135-152.

Kamber, B. S., Kramers, J. D. and Rollinson, H. R. (1993) The Triangle Shear Zone, a Proterozoic kill-joy in the tectonic model for the Archean Limpopo Mobile Belt. Terra Abstracts, 5, 316-317.

Karhu, J. A. and Bekker A. (2020) Carbon isotopes in the solar system. In Gargaud M. et al.(eds). Encyclopedia of Astrobiology. Springer.

Kampunzu, A. B., Tomable, A. R., Zhai, M., Bagai, Z., Majaule, T. M., and Modisi, M. (2003) Major and trace element geochemistry of plutonic rocks from Francistown, NE Botswana: Evidence for Neoarchean continental active margin in the Zimbabwe Craton. *Lithos 71*, 431-460.

Keith, M. Haase, K. M., Klemd, R., Krumm, S. and Strauss, H. (2016) Systematic variations of trace element and sulfur isotope compositions in pyrite with stratigraphic depth in the Skouriotissa volcanic-hosted massive sulfide deposit, Troodos ophiolite, Cyprus. Chemical Geology, 423, 7-18.

Keith, M. Smith, D. J., Jenkin, G. R.T., Holwell, D. A. and Dye, M. D. (2018) A review of Te and Se systematic in hydrothermal pyrite from precious metal deposits: insights into ore-forming processes. Ore Geology Reviews, 96, 269-282.

Kusky, T. M. (1998) Tectonic setting and terrane accretion of the Archean craton. Geology, 26, 163-166.

Liu, H. and Chang, L. L. Y. (1994) Phase relations in the system PbS-PbSe-PbTe. Mineralogy Magazine, 58, 567-578.

Liu, Z., Shao, Y., Zhou H., Liu, N., Huang, K., Liu, Q., Zhang, J. and Wang C. stratiform and lamellar orebodies: Implications for the ore genesis of the Dongguashan Copper (Gold) deposit, Eastern China. Minerals, 8, 380.

Majaule, T. and Davis, D. W. (1998) U-Pb zircon dating and geochemistry of the granitoids in the Mosetse area, NE Botswana, and tectonic implications. 50th Anniversary International Conference, Abstract Volume. Geological Survey of Botswana, 46-48.

Majaule, T., Hall, R. P. and Hughes, D. J. (1997) Geochemistry of mafic and ultramafic igneous rocks of the Matsitama supracrustal belt, northeastern Botswana-provenance implications. South African Journal of Geology, 100, 169-179.

Master, S. (1994) Geodynamic evolution and correlation of the Magondi Belt, Zimbabwe, implications for the Paleoproterozoic history of Botswana. Botswana Journal of Earth Science, 2, 25-32.

McCourt, S., and Armstrong, R. A. (1998) SRIMP U-Pb zircon geochronology of granites from the Central Zone, Limpopo Belt, southern Africa: Implications for the age of the Limpopo Orogeny. *South African Journal of Geology, 101*, 329-338.

McCourt, S., Kampunzu, A. B., Bagai, Z. and Armstrong, R. A. (2004) The crustal architecture of Archean terranes in Northeastern Botswana. Geological Society of South Africa, 107, 147-158.

Mei, J. M. (2000) Chemical typomorphic characteristics of pyrite from Zhilingtou gold deposit, Suichang, Zhejiang. Geoscience, 14, 51-55.

Newall, P., Szebor, N., Mounde, M., King, P., Allen A., Kenwright, M. and Luneva, V. (2018) Competent Person's Report on the Mineral Assets held by Cradle Arc in Africa. London: Wadell Armstrong International, Unpublished Report, 204p.

Och, L. M. and Shields-Zhou, G. A. (2012) The Neoproterozoic oxyenegation event: environmental pertubations and biochemical cycling. Earth-Science Reviews, 110, 26-57.

Oberthur, T., Davis, D. W., Blenkinsop, T. G. and Hohndorf, A. (2002) Precise U–Pb mineral ages, Rb–Sr and Sm–Nd systematics for the Great Dyke, Zimbabwe—constraints on late Archean events in the Zimbabwe craton and Limpopo belt. Precambrian Research, 113, 293–305.

Ohmoto, H. (1986) Stable isotope geochemistry of ore deposits. In Valley, J. W., Taylor Jr., H. P., O'Neil, J. R. (eds). Stable Isotopes in High-Temperature Geological Processes. Reviews in Mineralogy, 16, 491-559.

Ohmoto, H. and Rye, R. O. (1979) Isotopes of Sulfur and Carbon. In Barnes, H. L. (ed). Geochemistry of Hydrothermal Deposits. 2nd edition. New York: John Wiley & Sons, Inc., 509-567.

Prendergast, M. D. (2004) The Bulawayan Supergroup: A late Archean passive margin related large igneous province in the Zimbabwe craton. Journal of the Geological Society (London), 161, 431-445.

Ranganai, R. T., Kampunzu, A. B., Atekwana, E. A., Paya, B. K., King, J. G., Koosimile, D. I. and Stettler E. H. (2002) Gravity evidence for a larger Limpopo Belt in Southern Africa and geodynamic implications. Geophysics Journal International 149, F9-F14.

Reed, M. H. and Palandri, J. (2006) Sulfide mineral precipitation from hydrothermal fluids. Reviews in Mineralogy and Gochemistry, 61, 609-631.

Reyes, A. G. (1990) Petrology of the Philippine geothermal systems and the application of alteration mineralogy to their assessment. Journal of Volcanology and Geothermal Research, 43, 279-309.

Roedder, E. (1979) Fluid inclusions as samples of ore fluids. In Barnes, H. L. (ed) Geochemistry of Hydrothermal Ore deposits. 2nd edition. John Wiley & Sons, Inc. New York, 684-737

Schidlowski, M. (2001) Carbon isotopes as biogeochemical recorders of life over 3.8 Ga of Earth history: evolution of a concept. Precambrian Research, 106, 117-134.

Selly, D., Scott, R., Emsbo, P., Koziy, L., Hitzman, M. W., Bull, S. W., Duffett, M., Sebagenzi, S., Halpin, J. and Broughton, D. W.M. (2018) Structural configurations of the Central African Copperbelt: Roles of evaporites in structural evolution, basin hydrology and ore location. Society of Economic Geologists Inc. SEG Special Publications, 21, 115-156.

Seward, T. M., William-Jones, A. E. and Migdisov, A. A. (2014) The chemistry of metal transport and deposition by ore-forming hydrothermal fluids. In Scott, S. (ed.). Treatise on Geochemistry, 13, Amsterdam, Elsevier, 29-57.

Sharp, Z. D. (1990) Laser based microanalytical method for the in situ determination of oxygen isotope ratios of silicates and oxides. Geochimica et Cosmochimica Acta, 54, 1352-1357.

Simmons, S. F., White, N. C. and John, D. A. (2005) Geological Characteristics of epithermal precious and base metal deposits. In Hedenquist, J. W., Thompson, J. F. H., Goldfarb, R. J. and Richards, J. P. One Hundredth Annivesary Volume. Society of Economic Geologists Inc., Littleton, 485-522.

Van Reenen, D. D., Smit, C. A., Perchuk, A. L., Huizenga, J.M., Safonov, O. G. and Gerya, T. V. (2019) The Neoarchean Limpopo Orogeny: Exhumation and regional-scale gravitational crustal overturn driven by a granulite diapir. In Kroner, A. and Hoffman, A. (eds.). The Archean Geology of the Kaapvaal Craton, Southern Africa. Springer International Publishing, 185-224.

Watkeys, M. K., Light, M. P. R. and Broederick, R. J. (1983) A retrospective view of the central zone of the Limpopo Belt, Zimbabwe. Geological Society of South Africa, Special Publication, 8, 65-80.

Wilson, J. F., Nesbitt, R. W. and Fanning, C. M. (1995) Zircon geochronology of Archaean felsic sequences in the Zimbabwe craton: A revision of greenstone stratigraphy and a model for crustal growth. In Coward, M. P. and Ries, A. C (eds.). Early Precambrian Processes. Geological Society (London), Special Publications,109-126.

Wormald, R. J. and Downey, W.S. (1999) The high heat production Gaborone Granite Complex in southeast Botswana and its economic significance. Botswana Journal of Earth Sciences, 4, 39-45.

Yanagisawa, F. and Sakai, H. (1983) Thermal decomposition of barium sulfate-vanadium pentaoxide-silica glass mixtures for preparation of sulfur dioxide in sulfur isotope ratio measurements. Analytical Chemistry, 55, 985-987.

Zhou, X. W., Li, S. R., Lu, L., Li, J. J. and Wang, J. Z (2005) Study of pyrite typomorphic characteristics of Wulong quartz-vein-type deposit in Dandong, Liaoning Province, China. Geoscience, 19, 231-238

Zhu, Y. and Tan, F. J. (2011) Geochemistry of hydrothermal gold deposits: A review. Geoscience Frontiers, 2, 367-374.

ACKNOWLEDGEMENTS

First and foremost, I would like to express my sincere gratitude to the Japanese Government (MEXT: Monbukagusho) scholarship and Akita University for the opportunity and financial support for this research.

I sincerely acknowledge my supervisors, Professor Akira Imai at Kyushu University, Professor Andrea Agangi, and Associate Professor Ryohei Takahashi at Akita University for their enthusiasm, unending guidance, and support throughout my research.

I would like to extend my sincere gratitude to the Leboam Holdings Limited for giving permission for this work within their mining lease area and for providing logistical support during field work despite the hardships the company faced.

I would like to express many thanks to Dr Manalo for having supported me through all the trail of this research work. She always had her office open for me with numerous questions and for motivation when I am down.

Dr Hinako Sato cannot in anyhow be left out as she was very helpful in providing guidance on the analytical measurements carried out in this research. Last but no means least I would like to thank my Economic Geology laboratory members and friends for all their immense help and support they offered me always.

I am greatly thankful to the friends in my life for their support and company when the going really got tough. They always gave me a push to keep moving.

APPENDIX I

CHALCOPYRITE MAJOR AND MINOR ELEMENT COMPOSITION

No.	As	S	Te	Pb	Fe	Cu	Zn	Ni	Cr	Co	Au	Ag	Total
3	0.000	33.484	0.000	0.000	31.010	33.831	0.000	0.000	0.000	0.000	0.004	0.009	98.34
4	0.000	33.282	0.010	0.000	30.974	33.586	0.000	0.000	0.000	0.000	0.009	0.008	97.87
5	0.005	33.221	0.002	0.000	30.956	34.026	0.000	0.000	0.012	0.000	0.006	0.007	98.24
8	0.000	33.244	0.000	0.000	30.966	33.864	0.000	0.000	0.000	0.000	0.002	0.006	98.08
9	0.000	33.557	0.007	0.000	31.086	33.827	0.000	0.000	0.000	0.000	0.000	0.005	98.48
10	0.037	32.957	0.000	0.000	31.115	33.729	0.000	0.000	0.000	0.000	0.009	0.005	97.85
11	0.039	33.071	0.000	0.000	31.512	33.791	0.000	0.000	0.000	0.000	0.000	0.001	98.41
15	0.014	33.508	0.000	0.000	31.076	34.094	0.000	0.000	0.000	0.000	0.006	0.009	98.71
16	0.000	32.222	0.000	0.000	31.240	33.589	0.000	0.000	0.002	0.000	0.003	0.018	97.07
17	0.028	33.595	0.000	0.000	31.164	33.256	0.000	0.000	0.000	0.000	0.006	0.011	98.06
18	0.000	33.892	0.007	0.000	30.831	33.995	0.000	0.000	0.006	0.000	0.000	0.005	98.74
19	0.018	33.544	0.002	0.000	30.984	34.158	0.000	0.000	0.000	0.000	0.000	0.011	98.72
20	0.000	33.714	0.000	0.000	31.032	34.110	0.000	0.000	0.000	0.000	0.000	0.008	98.86
21	0.000	33.428	0.014	0.000	30.623	33.522	0.000	0.000	0.001	0.000	0.003	0.014	97.61
22	0.000	33.365	0.003	0.000	30.719	33.411	0.000	0.000	0.014	0.000	0.006	0.008	97.53
23	0.006	33.895	0.000	0.000	30.519	33.378	0.000	0.000	0.000	0.000	0.004	0.011	97.81
42	0.000	33.208	0.017	0.000	30.447	33.813	0.000	0.000	0.000	0.000	0.000	0.000	97.49
43	0.000	33.370	0.000	0.000	30.666	33.765	0.000	0.000	0.002	0.000	0.003	0.006	97.81
44	0.001	33.072	0.006	0.000	30.596	33.750	0.000	0.000	0.015	0.000	0.004	0.002	97.45
45	0.008	33.575	0.022	0.000	30.480	33.735	0.000	0.000	0.000	0.000	0.004	0.003	97.83
47	0.012	33.416	0.014	0.000	30.548	33.589	0.000	0.000	0.001	0.000	0.008	0.005	97.59
48	0.000	33.553	0.000	0.000	30.653	33.776	0.000	0.000	0.009	0.000	0.005	0.000	98.00
50	0.000	33.623	0.000	0.000	30.441	33.783	0.000	0.000	0.000	0.000	0.000	0.009	97.86
51	0.000	33.510	0.017	0.000	30.688	33.902	0.000	0.000	0.000	0.000	0.005	0.007	98.13
52	0.006	33.823	0.000	0.000	30.646	33.782	0.000	0.000	0.000	0.000	0.004	0.004	98.27
53	0.001	33.574	0.000	0.000	30.538	33.789	0.000	0.000	0.001	0.000	0.009	0.007	97.92
54	0.000	33.576	0.000	0.000	30.694	33.747	0.000	0.000	0.011	0.000	0.003	0.008	98.04
55	0.009	33.484	0.004	0.000	30.500	33.695	0.000	0.000	0.013	0.000	0.001	0.002	97.71

56	0.000	33.491	0.000	0.000	30.447	33.856	0.000	0.000	0.000	0.000	0.000	0.010	97.80
57	0.027	33.764	0.000	0.000	30.676	33.693	0.000	0.000	0.000	0.000	0.008	0.001	98.17
58	0.006	33.265	0.021	0.000	30.628	33.671	0.000	0.000	0.005	0.000	0.004	0.013	97.61
59	0.000	33.673	0.000	0.000	30.555	33.852	0.000	0.000	0.000	0.000	0.000	0.005	98.09
60	0.000	33.342	0.000	0.000	30.790	33.664	0.000	0.000	0.000	0.000	0.000	0.007	97.80
61	0.024	33.816	0.000	0.000	30.499	33.959	0.000	0.000	0.000	0.000	0.004	0.006	98.31
64	0.000	33.668	0.000	0.000	30.650	33.533	0.000	0.000	0.003	0.000	0.000	0.015	97.87
65	0.000	33.720	0.000	0.000	30.625	33.890	0.000	0.000	0.011	0.000	0.001	0.003	98.25
66	0.057	33.458	0.000	0.000	30.595	33.732	0.010	0.000	0.001	0.000	0.004	0.002	97.86
67	0.000	33.795	0.000	0.000	30.446	33.788	0.000	0.000	0.004	0.000	0.012	0.005	98.05

APPENDIX II

PYRITE MAJOR AND MINOR ELEMENT COMPOSITION

No.	As	Pb	S	Te	Ag	Au	Cu	Cr	Zn	Fe	Ni	Co	Total
5	0.01	0.34	53.32	0.00	0.00	0.01	0.03	0.00	0.00	46.37	0.00	0.00	100.078
6	0.00	1.63	53.31	0.00	0.00	0.01	0.04	0.00	0.00	45.95	0.00	0.00	100.936
7	0.03	1.83	53.09	0.00	0.00	0.00	0.06	0.00	0.00	45.59	0.00	0.00	100.614
8	0.00	1.02	53.32	0.00	0.00	0.00	0.01	0.00	0.06	45.84	0.01	0.00	100.267
10	0.02	0.00	53.44	0.00	0.00	0.00	0.00	0.00	0.04	46.19	0.00	0.00	99.689
11	0.00	2.10	53.19	0.00	0.00	0.01	0.03	0.00	0.05	45.66	0.00	0.00	101.03
12	0.00	0.00	53.53	0.00	0.00	0.00	0.04	0.00	0.00	46.33	0.00	0.00	99.902
13	0.02	0.00	53.46	0.00	0.00	0.00	0.00	0.01	0.00	46.47	0.00	0.05	100.005
14	0.00	0.00	53.94	0.01	0.00	0.02	0.00	0.00	0.00	46.26	0.00	0.00	100.217
15	0.00	0.82	53.41	0.00	0.00	0.00	0.00	0.01	0.00	46.49	0.00	0.00	100.73
16	0.01	0.00	53.54	0.00	0.00	0.00	0.02	0.00	0.00	46.52	0.00	0.00	100.09
17	0.00	0.00	53.59	0.00	0.00	0.01	0.00	0.00	0.00	46.03	0.00	0.00	99.63
18	0.00	0.00	53.75	0.00	0.00	0.01	0.00	0.00	0.00	46.03	0.00	0.00	99.79
19	0.01	1.22	53.42	0.00	0.00	0.01	0.00	0.01	0.02	45.78	0.00	0.00	100.48
20	0.00	0.61	53.23	0.00	0.00	0.01	0.04	0.00	0.05	46.07	0.00	0.00	100.01
21	0.00	1.97	53.30	0.00	0.00	0.00	0.00	0.01	0.00	45.83	0.00	0.07	101.17
22	0.00	0.00	53.90	0.00	0.00	0.01	0.05	0.01	0.00	45.96	0.00	0.00	99.94
23	0.04	0.00	53.69	0.00	0.00	0.00	0.00	0.00	0.00	46.01	0.00	0.10	99.83
24	0.01	0.00	53.73	0.00	0.00	0.01	0.03	0.00	0.06	46.32	0.00	0.02	100.17
25	0.00	0.41	53.63	0.00	0.00	0.00	0.00	0.00	0.00	46.12	0.01	0.01	100.19
26	0.00	1.63	53.47	0.00	0.00	0.00	0.04	0.00	0.00	46.01	0.00	0.03	101.18
27	0.03	0.00	53.59	0.00	0.00	0.00	0.00	0.01	0.00	46.09	0.00	0.07	99.79
29	0.00	1.77	53.07	0.00	0.00	0.00	0.00	0.00	0.03	46.33	0.00	0.00	101.19
30	0.00	0.41	53.47	0.00	0.00	0.00	0.00	0.00	0.00	45.88	0.00	0.00	99.76

No	As	Pb	S	Te	Ag	Au	Cu	Cr	Zn	Fe	Ni	Co	Total
31	0.00	0.00	53.69	0.00	0.00	0.00	0.00	0.00	0.03	46.28	0.00	0.00	100.00
32	0.05	2.64	53.34	0.00	0.00	0.01	0.04	0.01	0.00	45.94	0.00	0.00	102.04
33	0.03	0.00	53.29	0.01	0.00	0.01	0.00	0.00	0.03	46.12	0.00	0.00	99.48
34	0.00	0.00	53.46	0.00	0.00	0.00	0.07	0.00	0.00	45.88	0.00	0.00	99.40
37	0.07	0.75	52.42	0.00	0.00	0.01	0.00	0.01	0.00	45.36	0.01	0.01	98.63
38	0.01	1.56	53.31	0.00	0.00	0.00	0.00	0.01	0.00	46.21	0.03	0.00	101.14
39	0.00	2.77	53.24	0.00	0.00	0.00	0.04	0.00	0.00	45.92	0.00	0.00	101.97
40	0.00	0.00	53.48	0.00	0.00	0.02	0.03	0.00	0.02	46.00	0.00	0.00	99.54
41	0.04	1.97	53.33	0.00	0.00	0.01	0.00	0.00	0.04	45.61	0.00	0.00	100.98
42	0.04	0.14	53.32	0.00	0.00	0.00	0.00	0.00	0.00	46.10	0.00	0.02	99.62
43	0.00	2.57	53.17	0.00	0.00	0.01	0.02	0.00	0.00	45.61	0.00	0.00	101.38
45	0.00	0.00	53.56	0.00	0.00	0.01	0.03	0.00	0.03	45.80	0.00	0.00	99.42
46	0.01	0.00	53.31	0.01	0.00	0.00	0.00	0.02	0.00	46.00	0.00	0.08	99.42
47	0.02	0.00	53.22	0.00	0.00	0.00	0.04	0.01	0.00	46.48	0.00	0.00	99.77
48	0.00	1.43	53.36	0.00	0.00	0.01	0.00	0.01	0.02	45.97	0.00	0.07	100.86
49	0.01	0.00	53.44	0.00	0.00	0.00	0.03	0.01	0.07	45.95	0.01	0.03	99.55
50	0.00	1.29	53.24	0.00	0.00	0.00	0.08	0.01	0.00	45.96	0.02	0.00	100.61
51	0.01	1.29	53.36	0.00	0.00	0.00	0.06	0.03	0.00	45.98	0.00	0.09	100.82
52	0.00	0.00	53.46	0.00	0.00	0.01	0.02	0.00	0.02	46.18	0.00	0.08	99.78
53	0.04	0.55	53.38	0.00	0.00	0.01	0.00	0.00	0.00	46.12	0.00	0.00	100.09
54	0.02	0.95	53.52	0.00	0.00	0.01	0.06	0.00	0.01	46.04	0.00	0.03	100.64
57	0.02	0.41	53.52	0.02	0.00	0.01	0.00	0.00	0.09	46.05	0.00	0.05	100.16
58	0.02	3.77	53.24	0.00	0.00	0.00	0.00	0.01	0.00	45.54	0.01	0.00	102.59
59	0.04	1.76	53.30	0.00	0.00	0.02	0.05	0.00	0.00	45.85	0.00	0.07	101.09
61	0.02	0.00	53.39	0.00	0.00	0.01	0.09	0.02	0.00	46.32	0.00	0.00	99.86
62	0.02	0.82	53.25	0.00	0.00	0.00	0.00	0.00	0.02	46.02	0.00	0.07	100.20
63	0.00	0.68	53.49	0.00	0.00	0.00	0.03	0.00	0.05	46.11	0.00	0.00	100.35
64	0.02	0.00	53.43	0.00	0.00	0.00	0.00	0.00	0.00	46.08	0.00	0.00	99.54
65	0.00	1.83	53.50	0.00	0.00	0.00	0.03	0.00	0.00	46.06	0.01	0.00	101.42

66	0.00	0.00	53.16	0.01	0.00	0.01	0.00	0.02	0.00	46.03	0.05	0.00	99.28
68	0.00	0.00	52.37	0.00	0.00	0.00	0.01	0.00	0.00	45.26	0.01	0.00	97.65
69	0.03	0.00	53.03	0.00	0.00	0.00	0.00	0.02	0.00	45.70	0.01	0.00	98.79
70	0.00	1.36	53.01	0.00	0.00	0.00	0.02	0.00	0.01	45.79	0.00	0.00	100.19
71	0.00	3.11	53.07	0.00	0.00	0.00	0.00	0.00	0.00	45.41	0.00	0.00	101.59
72	0.00	0.00	53.10	0.01	0.00	0.00	0.03	0.02	0.02	46.27	0.00	0.00	99.45
73	0.02	0.00	53.25	0.00	0.00	0.00	0.00	0.00	0.00	46.17	0.00	0.00	99.45
74	0.03	3.31	53.59	0.00	0.00	0.01	0.00	0.01	0.00	46.11	0.00	0.01	103.06
75	0.00	2.03	53.26	0.00	0.00	0.00	0.06	0.02	0.00	45.77	0.00	0.06	101.20
76	0.00	1.76	53.11	0.00	0.00	0.00	0.02	0.00	0.00	45.84	0.02	0.00	100.75
77	0.00	2.37	53.20	0.00	0.00	0.02	0.00	0.01	0.03	45.59	0.03	0.00	101.24
78	0.00	0.34	53.13	0.00	0.00	0.01	0.02	0.00	0.00	45.99	0.00	0.00	99.48
79	0.00	0.61	53.42	0.00	0.00	0.00	0.02	0.02	0.00	46.02	0.00	0.00	100.10
80	0.00	0.55	53.45	0.01	0.00	0.01	0.00	0.00	0.07	45.72	0.00	0.00	99.80
84	0.02	0.34	53.36	0.00	0.00	0.01	0.00	0.00	0.00	46.18	0.00	0.00	99.91
85	0.00	0.34	53.25	0.01	0.00	0.00	0.05	0.00	0.00	45.94	0.00	0.00	99.60
86	0.00	0.68	53.78	0.01	0.00	0.00	0.00	0.00	0.00	46.25	0.00	0.00	100.73
87	0.00	0.00	53.65	0.00	0.00	0.00	0.01	0.00	0.00	45.82	0.00	0.00	99.48
88	0.01	2.30	53.60	0.00	0.00	0.00	0.00	0.00	0.00	45.50	0.00	0.00	101.41

APPENDIX III

GALENA MAJOR AND MINOR ELEMENT COMPOSITION

	No.	Se	As	Zn	S	Fe	Cu	Pb	Au	Ag	Sb	Total
sample 1	1	0.066	0.000	0.000	13.325	0.000	0.004	85.207	0.000	0.000	0.000	98.60
sample1	2	0.000	0.000	0.002	12.711	0.025	0.012	84.288	0.000	0.000	0.000	97.04
sample 1	3	0.103	0.000	0.000	13.398	0.007	0.000	86.089	0.000	0.000	0.000	99.60
sample 1	4	0.008	0.000	0.000	13.407	0.001	0.000	85.977	0.000	0.000	0.000	99.39
sample 1	5	0.044	0.000	0.000	13.418	0.019	0.003	87.010	0.000	0.000	0.000	100.49
sample 1	6	0.117	0.000	0.000	13.192	0.000	0.000	85.585	0.000	0.000	0.000	98.89
sample 1	7	0.137	0.000	0.002	13.253	0.013	0.000	85.572	0.000	0.000	0.000	98.98
sample 1	8	0.104	0.000	0.000	13.083	0.013	0.114	84.890	0.000	0.035	0.000	98.24
sample 2	9	0.107	0.000	0.000	13.275	0.000	0.012	85.824	0.000	0.000	0.000	99.22
sample2	10	0.007	0.000	0.000	13.160	0.018	0.000	85.715	0.000	0.000	0.000	98.90
sample 2	11	0.103	0.000	0.000	13.481	0.032	0.000	85.544	0.000	0.000	0.000	99.16
sample 2	12	0.150	0.000	0.000	13.439	0.031	0.031	86.498	0.000	0.000	0.000	100.15
sample 2	13	0.168	0.000	0.000	13.339	0.022	0.002	85.919	0.000	0.000	0.000	99.45
sample 2	16	0.284	0.000	0.017	13.069	0.020	0.635	84.082	0.000	0.177	0.000	98.28
sample 2	17	0.037	0.000	0.000	12.998	0.001	0.000	85.122	0.000	0.000	0.000	98.16
sample 2	18	0.128	0.000	0.015	13.425	0.016	0.000	86.359	0.000	0.000	0.000	99.94
sample 2	19	0.214	0.000	0.015	13.466	0.034	0.051	85.593	0.000	0.000	0.000	99.37
sample 2	20	0.148	0.000	0.000	13.156	0.035	0.000	85.477	0.000	0.000	0.000	98.82
sample 3	21	0.197	0.000	0.000	13.237	0.020	0.000	85.436	0.000	0.000	0.000	98.89
sample 3	22	0.135	0.000	0.006	13.058	0.019	0.000	86.452	0.000	0.000	0.000	99.67
sample 3	23	0.079	0.000	0.000	13.285	0.018	0.000	85.670	0.000	0.000	0.000	99.05
sample 3	24	0.191	0.000	0.000	13.173	0.000	0.000	85.789	0.000	0.000	0.000	99.15
sample 3	25	0.148	0.000	0.000	13.306	0.006	0.000	86.176	0.000	0.000	0.000	99.64
sample 3	26	0.117	0.000	0.000	13.225	0.000	0.000	85.454	0.000	0.000	0.000	98.80
sample 3	27	0.083	0.000	0.000	13.178	0.024	0.000	86.189	0.000	0.000	0.000	99.47
sample 3	28	0.144	0.000	0.000	13.242	0.008	0.000	85.850	0.000	0.000	0.000	99.24
sample 3	29	0.072	0.000	0.000	13.262	0.011	0.000	85.430	0.000	0.000	0.000	98.78
sample 3	30	0.044	0.000	0.000	13.209	0.000	0.000	85.086	0.000	0.000	0.000	98.34

	No.	Se	As	Zn	S	Fe	Cu	Pb	Au	Ag	Sb	Total
Sample 4	31	0.078	0.000	0.000	13.119	0.012	0.000	85.584	0.000	0.000	0.000	98.79
sample 4	32	0.122	0.000	0.018	13.449	0.021	0.181	86.050	0.000	0.000	0.000	99.84
Sample 4	33	0.271	0.000	0.000	13.254	0.014	0.001	86.237	0.000	0.000	0.000	99.78
Sample 4	34	0.293	0.000	0.000	13.393	0.000	0.000	86.000	0.000	0.000	0.000	99.69
Sample 4	35	0.197	0.000	0.000	13.132	0.028	0.000	86.127	0.000	0.000	0.000	99.48
Sample 4	36	0.070	0.000	0.000	13.170	0.009	0.000	85.397	0.000	0.000	0.000	98.65
Sample 4	37	0.118	0.000	0.000	13.379	0.028	0.015	85.523	0.000	0.000	0.000	99.06
Sample 4	39	0.146	0.000	0.005	12.722	0.031	0.005	85.131	0.000	0.000	0.000	98.04

APPENDIX IV

CHEMICAL COMPOSITION OF CHLORITE

	Amo_141	Amo_142	Amo_143	Amo_144	Amo_145	Amo_147	Amo_148	Amo_149	Amo_150	Amo_151	Amo_152	Amo_153
SiO2 (wt.%)	24.72	24.12	25.08	25.59	24.10	25.00	24.41	24.21	25.34	23.81	25.15	24.87
TiO2	3.36	0.11	0.15	0.15	0.13	0.14	0.11	0.07	0.06	0.07	0.15	0.09
Al2O3	17.88	19.50	19.58	19.90	19.48	19.88	19.79	19.68	18.12	19.92	19.69	19.46
Cr2O3	0.00	0.01	0.02	0.04	0.01	0.00	0.01	0.00	0.03	0.01	0.02	0.00
Fe2O3	0.69	0.00	0.00	0.00	0.00	0.00	0.00	0.00	0.00	0.00	0.00	0.00
FeO	28.37	32.41	31.13	30.45	32.53	30.86	31.61	31.82	31.31	31.65	31.04	31.22
MnO	0.40	0.47	0.38	0.40	0.45	0.39	0.42	0.39	0.37	0.41	0.38	0.41
MgO	10.99	11.87	11.65	11.60	11.71	12.33	12.34	12.24	13.40	12.29	12.51	12.41
ZnO	0.02	0.03	0.00	0.00	0.04	0.04	0.03	0.00	0.02	0.05	0.03	0.05
CaO	2.73	0.03	0.05	0.04	0.03	0.03	0.04	0.05	0.03	0.06	0.08	0.03
Na2O	0.03	0.04	0.01	0.00	0.02	0.00	0.02	0.03	0.01	0.04	0.04	0.03
K2O	0.11	0.03	0.42	0.64	0.10	0.29	0.10	0.05	0.03	0.05	0.08	0.04
H2O*	11.15	10.98	11.06	11.15	10.97	11.15	11.08	11.02	11.08	10.99	11.18	11.08
Total	100.45	99.59	99.52	99.96	99.55	100.10	99.94	99.57	99.80	99.33	100.33	99.69
Total cation (O=14)												
Si	2.653	2.613	2.706	2.740	2.614	2.675	2.624	2.614	2.722	2.576	2.686	2.677
Al iv	1.347	1.387	1.294	1.260	1.386	1.325	1.376	1.386	1.278	1.424	1.314	1.323
Al vi	0.920	1.123	1.210	1.263	1.125	1.196	1.149	1.139	1.033	1.139	1.177	1.159
Ti	0.271	0.009	0.012	0.012	0.010	0.011	0.009	0.006	0.005	0.005	0.012	0.007
Cr	0.000	0.001	0.001	0.003	0.001	0.000	0.001	0.000	0.002	0.000	0.001	0.000
Fe3+	0.056	0.000	0.000	0.000	0.000	0.000	0.000	0.000	0.000	0.000	0.000	0.000
Fe2+	2.546	3.043	2.854	2.743	3.056	2.819	2.934	2.976	2.912	2.983	2.826	2.877
Mn	0.036	0.043	0.035	0.036	0.041	0.036	0.038	0.036	0.034	0.037	0.034	0.037
Mg	1.758	1.917	1.873	1.852	1.892	1.966	1.977	1.971	2.146	1.982	1.992	1.992
Zn	0.001	0.003	0.000	0.000	0.003	0.003	0.002	0.000	0.002	0.004	0.002	0.004
Ca	0.314	0.003	0.006	0.004	0.003	0.003	0.005	0.005	0.003	0.007	0.009	0.004
Na	0.011	0.016	0.004	0.000	0.007	0.000	0.008	0.012	0.004	0.016	0.015	0.014
K	0.030	0.009	0.114	0.174	0.027	0.079	0.026	0.014	0.007	0.012	0.023	0.012
OH*	8.000	8.000	8.000	8.000	8.000	8.000	8.000	8.000	8.000	8.000	8.000	8.000
Fe/Fe+Mg	0.597	0.614	0.604	0.597	0.618	0.589	0.597	0.602	0.576	0.601	0.587	0.591
T (° C)	**372**	**385**	**355**	**344**	**384**	**365**	**381**	**384**	**349**	**397**	**361**	**364**

	Amo_154	Amo_155	Amo_156	Amo_157	Amo_158	Amo_159	Amo_160	Amo_161	Amo_162	Amo_163	Amo_164	Amo_165
SiO2 (wt.%)	25.42	24.39	23.83	24.67	24.15	23.97	24.05	24.23	24.04	24.00	24.01	24.18
TiO2	0.19	0.06	0.01	0.10	0.07	0.02	0.05	0.04	0.02	0.09	0.03	0.04
Al2O3	19.31	19.53	19.71	19.50	19.66	19.44	19.59	19.79	20.21	19.76	19.83	19.80
Cr2O3	0.03	0.02	0.00	0.03	0.02	0.02	0.02	0.01	0.02	0.02	0.01	0.01
Fe2O3	0.00	0.00	0.00	0.00	0.00	0.00	0.00	0.00	0.00	0.00	0.00	0.00
FeO	29.66	31.75	31.91	31.22	31.60	32.16	31.72	31.10	32.28	32.52	32.38	31.73
MnO	0.35	0.42	0.41	0.41	0.41	0.43	0.38	0.36	0.44	0.42	0.43	0.41
MgO	12.40	12.24	12.35	12.63	12.24	11.79	12.13	12.52	12.05	11.86	11.65	12.31
ZnO	0.05	0.00	0.04	0.00	0.01	0.03	0.06	0.04	0.04	0.02	0.01	0.03
CaO	0.06	0.04	0.03	0.05	0.04	0.02	0.06	0.04	0.03	0.03	0.03	0.05
Na2O	0.05	0.03	0.03	0.04	0.03	0.02	0.02	0.01	0.00	0.02	0.00	0.03
K2O	0.37	0.09	0.03	0.12	0.03	0.04	0.05	0.08	0.02	0.05	0.05	0.04
H2O*	11.07	11.02	10.97	11.09	10.99	10.90	10.96	11.02	11.07	11.00	10.96	11.03
Total	98.95	99.59	99.32	99.86	99.25	98.83	99.07	99.23	100.23	99.78	99.38	99.64
Total cation (O=14)												
Si	2.741	2.633	2.580	2.648	2.616	2.616	2.612	2.618	2.583	2.595	2.608	2.608
Al iv	1.259	1.367	1.420	1.352	1.384	1.384	1.388	1.382	1.417	1.405	1.392	1.392
Al vi	1.206	1.137	1.119	1.134	1.144	1.137	1.139	1.157	1.163	1.134	1.164	1.145
Ti	0.015	0.005	0.001	0.008	0.006	0.001	0.004	0.003	0.002	0.007	0.002	0.003
Cr	0.002	0.001	0.000	0.002	0.002	0.002	0.001	0.001	0.001	0.002	0.001	0.001
Fe3+	0.000	0.000	0.000	0.000	0.000	0.000	0.000	0.000	0.000	0.000	0.000	0.000
Fe2+	2.704	2.964	3.018	2.894	2.961	3.040	2.985	2.906	3.007	3.050	3.036	2.966
Mn	0.032	0.039	0.037	0.037	0.037	0.040	0.035	0.033	0.040	0.039	0.039	0.037
Mg	1.993	1.969	1.993	2.021	1.977	1.918	1.964	2.017	1.931	1.911	1.886	1.979
Zn	0.004	0.000	0.003	0.000	0.001	0.003	0.005	0.003	0.003	0.001	0.001	0.002
Ca	0.007	0.005	0.004	0.006	0.004	0.003	0.007	0.005	0.003	0.004	0.003	0.005
Na	0.023	0.014	0.012	0.017	0.011	0.006	0.006	0.002	0.000	0.008	0.000	0.011
K	0.100	0.024	0.009	0.032	0.009	0.011	0.013	0.021	0.007	0.012	0.013	0.012
OH*	8.000	8.000	8.000	8.000	8.000	8.000	8.000	8.000	8.000	8.000	8.000	8.000
Fe/Fe+Mg	0.576	0.601	0.602	0.589	0.600	0.613	0.603	0.590	0.609	0.615	0.617	0.600
T (° C)	**343**	**378**	**395**	**373**	**384**	**384**	**385**	**383**	**394**	**390**	**386**	**386**

	Amo_166	Amo_167	Amo_168	Amo_169	Amo_170	Amo_171	Amo_172	Amo_173	Amo_174	Amo_175	Amo_176	Amo_177
SiO2 (wt.%	23.96	24.07	24.65	24.58	24.65	24.29	24.38	24.37	24.08	24.37	24.44	24.50
TiO2	0.02	0.03	0.02	0.06	0.10	0.04	0.16	0.09	0.06	0.08	0.05	0.08
Al2O3	19.63	19.41	18.91	18.98	18.95	19.10	18.76	19.15	19.37	18.89	18.95	18.87
Cr2O3	0.01	0.00	0.01	0.02	0.02	0.01	0.01	0.00	0.04	0.01	0.01	0.01
Fe2O3	0.00	0.00	0.00	0.00	0.00	0.00	0.00	0.00	0.00	0.00	0.00	0.00
FeO	32.22	32.86	32.45	31.99	31.95	32.45	32.75	32.54	31.40	31.32	32.15	31.57
MnO	0.40	0.48	0.46	0.42	0.46	0.38	0.40	0.44	0.40	0.35	0.41	0.39
MgO	12.11	11.66	12.20	12.44	12.28	11.95	11.98	12.00	12.22	12.54	12.20	12.52
ZnO	0.04	0.04	0.07	0.05	0.08	0.08	0.03	0.04	0.04	0.04	0.03	0.04
CaO	0.04	0.03	0.03	0.03	0.04	0.03	0.12	0.03	0.05	0.04	0.06	0.04
Na2O	0.01	0.03	0.03	0.01	0.01	0.02	0.01	0.04	0.07	0.02	0.04	0.03
K2O	0.04	0.04	0.04	0.06	0.06	0.04	0.02	0.05	0.18	0.12	0.07	0.09
H2O*	10.97	10.95	11.02	11.02	11.01	10.95	10.96	10.99	10.93	10.93	10.97	10.97
Total	99.44	99.60	99.90	99.66	99.58	99.34	99.56	99.74	98.83	98.72	99.39	99.08
Total cation (O=14)												
Si	2.596	2.612	2.661	2.654	2.667	2.639	2.647	2.636	2.616	2.651	2.649	2.657
Al iv	1.404	1.388	1.339	1.346	1.333	1.361	1.353	1.364	1.384	1.349	1.351	1.343
Al vi	1.124	1.116	1.087	1.089	1.099	1.105	1.067	1.099	1.120	1.093	1.091	1.089
Ti	0.001	0.003	0.002	0.005	0.008	0.003	0.013	0.008	0.005	0.006	0.004	0.006
Cr	0.001	0.000	0.001	0.002	0.001	0.001	0.001	0.000	0.003	0.001	0.001	0.001
Fe3+	0.000	0.000	0.000	0.000	0.000	0.000	0.000	0.000	0.000	0.000	0.000	0.000
Fe2+	3.037	3.098	3.037	2.995	2.983	3.056	3.084	3.053	2.971	2.957	3.025	2.970
Mn	0.037	0.044	0.042	0.039	0.042	0.035	0.036	0.040	0.037	0.032	0.038	0.035
Mg	1.955	1.886	1.963	2.002	1.980	1.935	1.938	1.935	1.978	2.033	1.970	2.023
Zn	0.003	0.003	0.006	0.004	0.006	0.006	0.003	0.004	0.003	0.003	0.002	0.003
Ca	0.005	0.003	0.004	0.003	0.004	0.003	0.014	0.003	0.006	0.005	0.007	0.005
Na	0.006	0.012	0.012	0.006	0.003	0.009	0.003	0.017	0.029	0.010	0.016	0.011
K	0.010	0.011	0.010	0.017	0.017	0.011	0.006	0.012	0.049	0.034	0.020	0.025
OH*	8.000	8.000	8.000	8.000	8.000	8.000	8.000	8.000	8.000	8.000	8.000	8.000
Fe/Fe+Mg	0.608	0.622	0.607	0.599	0.601	0.612	0.614	0.612	0.600	0.593	0.606	0.595
T (° C)	**390**	**385**	**369**	**371**	**367**	**376**	**374**	**377**	**384**	**373**	**373**	**371**

	Amo_178	Amo_179	Amo_180	Amo_181	Amo_182	Amo_183	Amo_184	Amo_185	Amo_186	Amo_187	Amo_188	Amo_189
SiO2 (wt.%	24.22	25.18	24.47	24.78	24.48	24.28	24.79	24.78	24.51	24.39	24.44	25.18
TiO2	0.07	0.08	0.07	0.05	0.07	0.12	0.02	0.04	0.06	0.07	0.07	0.14
Al2O3	18.85	20.16	19.32	19.06	18.78	18.87	19.07	20.03	19.42	18.98	19.22	19.96
Cr2O3	0.02	0.00	0.02	0.01	0.00	0.01	0.00	0.01	0.01	0.02	0.01	0.01
Fe2O3	0.00	0.00	0.00	0.00	0.00	0.00	0.00	0.00	0.00	0.00	0.00	0.00
FeO	32.17	30.43	32.34	31.39	32.86	31.89	30.46	30.68	32.27	31.24	31.40	30.68
MnO	0.44	0.33	0.39	0.42	0.40	0.38	0.35	0.35	0.39	0.36	0.39	0.41
MgO	12.08	12.61	12.17	12.96	11.96	12.17	13.50	12.85	12.27	12.51	12.57	12.28
ZnO	0.01	0.00	0.07	0.02	0.07	0.05	0.03	0.00	0.00	0.04	0.03	0.10
CaO	0.04	0.04	0.04	0.04	0.05	0.05	0.03	0.10	0.04	0.16	0.06	0.06
Na2O	0.02	0.02	0.00	0.00	0.03	0.03	0.01	0.01	0.00	0.05	0.02	0.01
K2O	0.06	0.34	0.01	0.02	0.02	0.04	0.02	0.15	0.02	0.11	0.05	0.32
H2O*	10.90	11.21	11.04	11.08	10.97	10.91	11.08	11.17	11.06	10.95	11.00	11.18
Total	98.89	100.40	99.93	99.83	99.69	98.78	99.35	100.16	100.04	98.87	99.26	100.31
Total cation (O=14)												
Si	2.641	2.677	2.641	2.663	2.654	2.648	2.665	2.644	2.639	2.647	2.644	2.687
Al iv	1.359	1.323	1.359	1.337	1.346	1.352	1.335	1.356	1.361	1.353	1.356	1.313
Al vi	1.085	1.218	1.115	1.095	1.074	1.093	1.099	1.179	1.121	1.097	1.113	1.211
Ti	0.006	0.006	0.006	0.004	0.005	0.009	0.002	0.003	0.005	0.006	0.005	0.011
Cr	0.001	0.000	0.002	0.001	0.000	0.001	0.000	0.000	0.000	0.001	0.001	0.001
Fe3+	0.000	0.000	0.000	0.000	0.000	0.000	0.000	0.000	0.000	0.000	0.000	0.000
Fe2+	3.047	2.761	3.015	2.920	3.091	3.012	2.837	2.817	3.002	2.945	2.941	2.787
Mn	0.041	0.030	0.035	0.039	0.037	0.035	0.031	0.031	0.035	0.033	0.036	0.037
Mg	1.964	1.998	1.957	2.076	1.933	1.978	2.164	2.044	1.969	2.024	2.027	1.953
Zn	0.000	0.000	0.005	0.002	0.005	0.004	0.002	0.000	0.000	0.003	0.002	0.008
Ca	0.004	0.005	0.005	0.004	0.005	0.006	0.003	0.011	0.004	0.019	0.007	0.007
Na	0.009	0.008	0.000	0.000	0.014	0.011	0.002	0.004	0.000	0.020	0.008	0.003
K	0.018	0.091	0.002	0.006	0.007	0.011	0.006	0.041	0.006	0.029	0.014	0.087
OH*	8.000	8.000	8.000	8.000	8.000	8.000	8.000	8.000	8.000	8.000	8.000	8.000
Fe/Fe+Mg	0.608	0.580	0.606	0.584	0.615	0.604	0.567	0.579	0.604	0.593	0.592	0.588
T (° C)	**376**	**364**	**376**	**368**	**371**	**373**	**368**	**375**	**376**	**374**	**375**	**361**

	Amo_190	Amo_191	Amo_193
SiO2 (wt.%	24.05	24.99	25.80
TiO2	0.05	0.11	0.14
Al2O3	19.77	19.38	19.67
Cr2O3	0.01	0.02	0.03
Fe2O3	0.00	0.00	0.00
FeO	32.57	30.75	30.68
MnO	0.44	0.32	0.39
MgO	12.01	13.26	12.23
ZnO	0.02	0.05	0.02
CaO	0.06	0.05	0.05
Na2O	0.00	0.02	0.03
K2O	0.03	0.06	0.42
H2O*	11.03	11.16	11.24
Total	100.03	100.17	100.70
Total cation (O=14)			
Si	2.593	2.667	2.741
Al iv	1.407	1.333	1.259
Al vi	1.127	1.120	1.215
Ti	0.004	0.009	0.011
Cr	0.001	0.002	0.002
Fe3+	0.000	0.000	0.000
Fe2+	3.052	2.829	2.755
Mn	0.040	0.029	0.035
Mg	1.930	2.110	1.937
Zn	0.001	0.004	0.002
Ca	0.007	0.006	0.005
Na	0.000	0.007	0.012
K	0.009	0.016	0.113
OH*	8.000	8.000	8.000
Fe/Fe+Mg	0.613	0.573	0.587
T (° C)	**391**	**367**	**344**

APPENDIX V

STABLE ISOTOPES ANALYSES

Sample type: Limestone/dolomite

Smaple ID	Analysis Type	Delta 13C (‰)	Delta 18 O_{VPDB} (‰)	δ 18 O_{SMOW}	Other info
L2	C13, O18	6.65	-12.81	17.70	Host rock
L3	C13, O18	6.89	-10.2	20.39	Host rock
L18	C13, O18	6.05	-8.14	22.52	Host rock

Sample type: Graphitic schist

Sample ID	Analysis Type	Delta 13C (‰)	Other info
G2	C13	-29.8	Host rock
G3	C13	-21.0	Host rock
G4	C13	-27.2	Host rock

Sample type: Calcite

Smaple ID	Analysis Type	Delta 13C (‰)	Delta 18 O_{VPDB} (‰)	d18 O_{SMOW}	Other info
NP89b	C13, O18	0.53	-20.92	9.34	Type 1 vein
MP1b	C13, O18	0.46	-22.34	7.88	Type 1 vein
NP2b	C13, O18	-11.96	-12.42	18.11	Type 1 vein

Sample type: Quartz

Smaple ID	Analysis Type	Delta 18O (‰)	Other info
NP89a	O18	**10.29**	Type 1 vein
MP1a	O18	**9.25**	Type 1 vein
NP2a	O18	**10.1**	Type 1 vein

Calculations:

$$\delta 18O_{SMOW} = 1.03091 * \delta^{18}O_{VPDB} + 30.91$$

Temperature: 0.38 ($10^6/T^2$) Clayton et al., 1989

Formation temperature of the Type 1 veins

Quartz	Calcite	Quartz-Calcite	Temp(K)	Temp °C
18 O_{SMOW}	18 O_{SMOW}			
10.29	9.34	0.95	632.4555	359
9.25	7.88	1.37	526.6614	254
10.1	18.11	-8.01		